Comparison of the PDT and PACT activities of a series of water-soluble AAAB, ABAB, AABB, ABBB and BBBB Sn(IV) tetraarylporphyrins

A thesis submitted to Rhodes University in partial fulfilment of the requirements for the degree of

Master of Science (Chemistry)

By

Pertunia Rendani Macigane

ORCID ID: 0000-0002-5425-2938

RHODES UNIVERSITY
Where leaders learn

February 2025

---Dedication---

To myself, may this mile stone serve as a reminder that believeing in yourself, perseverance, determination, resilience, hard work and spirit of not giving up has made this achievement possible.

Congratulations, self! You did it.

“If you can't **fly** then **run** if you **can't run** then **walk** if you **can't walk** then **crawl,** but whatever you do, you have to keep moving forward.”

-Martin Luther King Jr.-

---Acknowledgement---

My supervisor, Professor John Mack, “Our academic Father”, your work ethic and quality of research have always motivated me to work tirelessly to my fullest potential. This work would not have been possible without your Scottish temperament (Resilience, Dark sense of humour & Determination).

Distinguished Professor T. Nyokong, I am honoured and grateful to be co-supervised by you. You have instilled in me the importance of communicating science and innovative research.

The Pearson-Young Memorial Scholarship and Rhodes University, the financial support and facility provided to complete my research work.

The INI (S22) colleagues, thank you for being part of my journey. The laboratory was a conducive environment. My sister -Kg- it has been a journey! We cried, laughed and always worked to our fullest potential. Without those venting sessions, I would be insane, singing in riddles. Thank you for always being one phone call away.

My collaborative colleagues within the Department of Chemistry, Prof. K. Lobb, Kabelo and Normsa, thank you for your assistance with Molecular docking.

To my parents, Ntanganedzeni and Mabung Macigane, your patience with my academic journey does not go unnoticed. Thank you for your unwavering, unconditional love and support.

To my siblings, Mukonazwothe and Mutshidzi Macigane, “I am their role model”, they say.`

To “Mine” Tiyani Alfred Ngwenyama, thank you for your support, words of encouragement, understanding and for being an escape from academic life.

---Abstract---

Cancer kills more people every year than tuberculosis, malaria, and AIDS combined. More than 60% of all cases are found in Africa, Latin America, and Asia. There is an ongoing need to identify and develop new treatments to diminish the mortality rate and increase life expectancy. Chemotherapy and radiotherapy can be used to treat cancer, but due to their severe side effects, photodynamic therapy (PDT) was developed as an alternative non-invasive method. To effectively and successfully treat cancer through PDT, a photosensitiser dye, a light source and singlet oxygen are required. PDT is used to treat skin, breast and prostate cancer, among others, that are readily accessible with a fibre optic. A photosensitiser dye is administered intravenously and accumulates in cancerous tumour cells. Since laser light is involved, the dye should absorb in the phototherapeutic window (620−850 nm), since haemoglobin and other pigments absorb at shorter wavelength, while water absorbs at longer wavelength. The aim of this study is to explore how readily synthesised tetraphenyl porphyrins, which absorb weakly at the higher energy edge of the phototherapeutic window, can be structurally modified to make them more suitable for biomedical photosensitiser dye applications by introducing 4-piperidinylphenyl groups introduced at the *meso*-positions. The porphyrinoids synthesised will be divided into four series: AAAB (Series 1), ABAB/AABB (Series 2), ABBB (Series 3) and BBBB (Series 4). The difference across these series relates to the number of 4-piperidinylphenyl groups introduced.

The Sn(IV) ion was inserted within the porphyrin central cavity since its *trans*-axial ligation hinders aggregation that can negatively impact the photophysical properties of the dyes. The metalation enhances the singlet oxygen quantum yield. A red shift of the lowest energy Q band of the Sn(IV) complexes of Series 1−4 to the edge of the phototherapeutic window is observed relative to the parent Sn(IV) tetraphenylporphyrin complex due to the presence of the 4-piperidinylphenyl groups. Quaterisation of the 4-piperidinylphenyl nitrogen atoms was carried

out to increase the water solubility of the porphyrin ligand and enhance its suitability for biomedical applications.

In vitro PDT and PACT activity studies have been carried out to assess the photodynamic activity of the porphyrinoids, and it can be elucidated that for the porphyrinoids to be photodynamically active, there should be a balance between their hydrophobicity and lipophilicity. All porphyrin analogues exhibited minimal dark cytotoxicity and high photodynamic (PDT) activity against MDA breast cancer cells. The IC_{50} values obtained for **3-Sn** and **3-Sn-Q** were > 1.79 and 1.09 μM, respectively, after irradiation with a 595 nm Thorlabs LED for 60 min. Series 1 (**1-Sn-Q**) and 2 (**2-Sn-Q**) exhibited exceptional antimicrobial activity against *S. aureus* bacteria with Log_{10} reduction values of 5.11 and 7.49, respectively, which demonstrates that the antimicrobial activity of the porphyrin analogues does not correlate with the number of charges on the quaternised nitrogen atoms of the 4-piperidinylphenyl groups.

Molecular docking studies were conducted to determine the probable pharmacological properties of the porphyrin analogues, and the results demonstrate that the compounds violate Lipinski's rule of five. Therefore, they cannot be used as orally active drugs but can administered as intravenous injections similar to Photofrin®. The porphyrinoids have exceptional ADMET properties and are predicted to be non-carcinogenic.

---Table of Contents---

---List of Figures---

---List of Schemes---

---List of Tables---

---List of Symbols---

f	Oscillator strength
Φ_F	Fluorescence quantum yield
Φ_Δ	Singlet oxygen quantum yield
IC_{50}	Half-maximal inhibitory concentration
λ	Wavelength
μM	Micromolar
τ_T	Triplet lifetime

---List of Abbreviations---

CFU	Colony-forming unit
DMEM	Dulbecco's modified Eagle's medium
DMSO	Dimethylsulfoxide
FDA	Food and Drug Administration
HOMO	Highest occupied molecular orbital
HSA	Human Serum Albmin
ISC	Inter-crossing System
LED	Light emitting diode
LUMO	Lowest occupied molecular orbital
MCF-7	Breast cancer cell line
MALDI-TOF-MS	Matrix-assisted laser desorption/ionisation-time of flight-mass spectrometry
PACT	Photodynamic antimicrobial therapy
PDT	Photodynamic Therapy
PS	Photosensitizers
PBS	Phosphate buffer saline
ROS	Reactive singlet species
$^1O_2$	Singlet Oxygen
TD-DFT	Time-dependent density functional theory

UV-vis	Ultraviolet-visible
ZnTPP	Zinc tetraphenylporphyrin

Chapter 1: Introduction

1.1 Problem Statement

Cancer is a deadly disease that kills people all over the world regardless of race, gender, age, country's demographics, and economic status [1-5]. In 2022, an estimated 20 million new cancer cases were reported, along with 9.74 million deaths due to cancer, and it is predicted that by the year 2045, there will be an increase to 32.6 million new cancer cases and the number of deaths due to cancer to increase to 16.9 million cases [2]. Since cancer can be viewed as an ongoing pandemic, identifying effective cancer treatments so that the mortality rate can be diminished and life expectancy can be increased is the subject of an intense global research effort.

Cancer is an umbrella term for diseases related to the uncontrollable growth of abnormal cells in the human body [2-6]. These abnormal cancer cells grow and clam on top of each other to form a mass called a tumour, which can be benign or malignant [6]. The cancerous cells within the benign tumour do not migrate to other organs, but those of malignant tumours migrate from the infected organ through the blood system to healthy organs and start to grow and accumulate to form another tumour through metastasis [6].

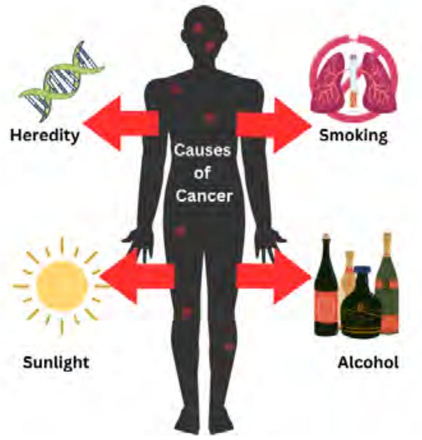

Figure 1. The potential causes of cancer.

There are over 150 types of cancer. The most common, affecting many people globally, are breast, lung, and prostate cancer [7-13]. The cause of cancer is statistically and scientifically unclear because no common cause has been identified, but factors such as (**Figure 1**) excess smoking have been discovered as the leading cause of lung cancer [7-13]. Exposure to sunlight, excessive consumption of alcohol, hereditary factors and obesity have been proven to increase the incidence of other types of cancer.

These different types of cancer can be treated through surgery, chemotherapy, and radiation therapy. Unfortunately, these traditional modes of cancer treatment cause server-side effects, tissue damage, and dysfunctionality of infected organs [7-13]. The traditional modes of cancer treatment are unselective between cancerous and normal tissue cells during their cancer treatment procedure. In breast cancer surgery, in most cases, they remove the whole breast instead of removing the infected part of the breast. Such disadvantages influenced the development of photodynamic therapy (PDT) in the past decade as an alternative substitute for cancer treatment [7-13].

1.2 Photodynamic Therapy (PDT)

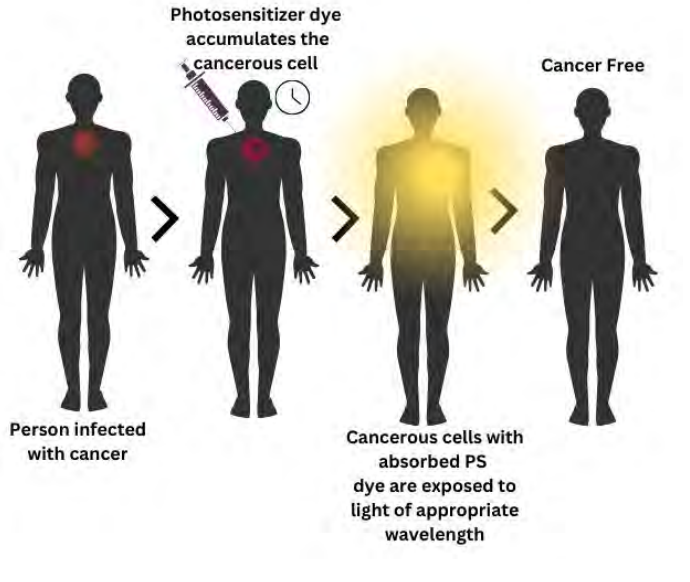

Figure 2. The treatment process applied during PDT.

Unlike traditional modes of cancer treatment, PDT is a controllable modality that can be modified to be selective between cancerous cells and normal tissue cells so that it can destroy cancerous cells without affecting the normal tissue cells (**Figure 2**). It is a target-orientated modality [14-27]. To treat cancer successfully and effectively in a non-invasive approach, PDT requires a photosensitiser (PS) dye, a light source of appropriate wavelength, and singlet oxygen ($^1O_2$). The PS and light source are two nontoxic PDT components, which, when combined, produce cytotoxic singlet oxygen and other reactive oxygen species (ROS) that destroy cancer cells through cell apoptosis [14-27].

1.3 PDT Mechanism

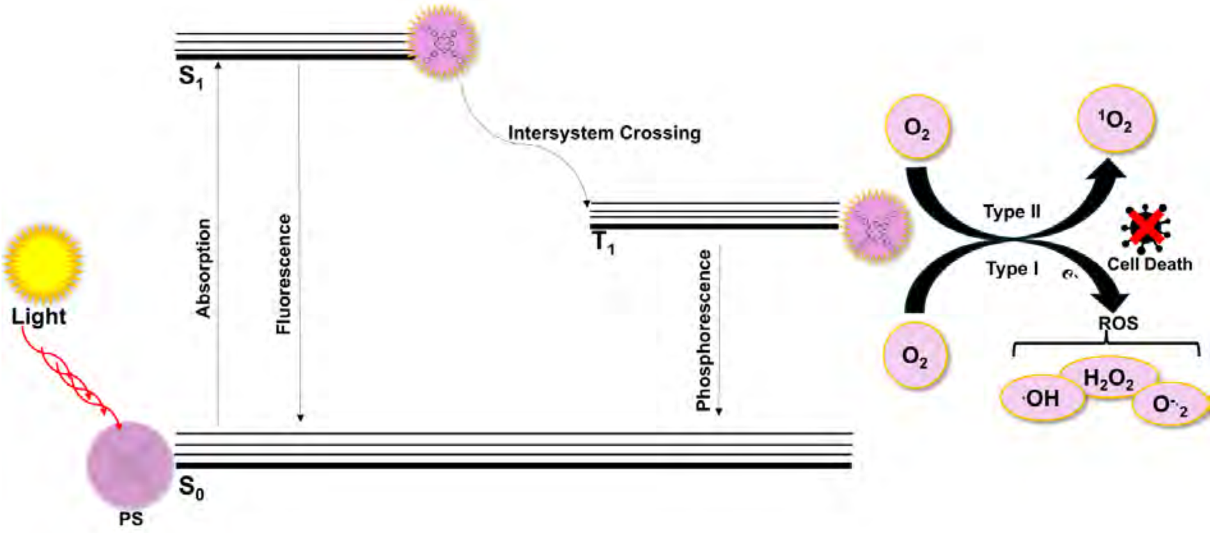

Figure 3. Jablonski diagram showing photochemical mechanism involved in PDT and PACT.

The photosensitiser dye is injected intravenously and accumulates in cancer cells. Light of appropriate wavelength is used to excite the PS dye from the ground singlet state (S_0) to the exited singlet state (S_1) [14-27]. As the singlet excited state photosensitiser undergoes relaxation, some return to the ground state through fluorescence and some (short-lived) undergo intersystem crossing (ISC) to the triplet state (T_1), where photochemical mechanisms Type I and II occur [14-27] (**Figure 3**). In the Type II reaction, the triplet excited PS interacts with molecular oxygen to produce the singlet oxygen species used in PDT and photodynamic antimicrobial chemotherapy (PACT) to cause tumour cell death and inactivate bacteria. However, in the Type I reaction, there is a direct interaction between the substrate and triplet excited PS dye, which produces radicals that transfer electrons to oxygen to produce reactive oxygen species (ROS), which are also used in both PDT and PACT to induce cell death or disrupt the cellular membrane, causing microbial cell death [14-27].

1.4 Photodynamic antimicrobial Therapy

There is a global health crisis related to antimicrobial resistance. Antimicrobial resistance occurs when diseases caused by bacteria, fungi and other pathogens are resistant to antimicrobial drugs (antibiotics), which makes it hard to cure bacterial diseases and increases the spread and death caused by the bacteria [28-38]. Photodynamic antimicrobial Therapy (PACT) is a promising method that can be used to eliminate pathogenic antimicrobial resistance caused by bacteria, such as *Staphylococcus aureus* (*S. aureus*), which causes skin and soft-tissue infections in hospitals. *S. aureus* is a spherical Gram-(+) bacteria resistant to Methicillin, the last effective antibiotic in this context. Antibiotic resistance is a global health threat because the resistant bacteria can be transmitted from one patient to another [28-38]. Photosensitiser dyes are in PACT to effectively treat antimicrobial resistance because it is difficult for bacteria to develop resistance to $^1O_2$ and the other ROS produced by the photosensitisers. The mechanism used in PDT and PACT are very similar. Hence, a photosensitiser dye can be used for both methods.

1.5 Photosensitiser Nomenclature

Photosensitisers are an essential component in PDT/PACT because, in their absence, singlet oxygen and reactive oxygen species used to cause cell death will not be produced. The FDA has approved several porphyrin PS dyes for use in PDT and PACT. They are aromatic planar macrocyclic organic compounds (natural/synthetic) that are composed of four pyrrolic rings connected by four methane bridges, which form the porphyrin core structure [39-40] (**Figure 4A**).

Porphyrins have four inner pyrrole nitrogens that form a coordination cavity at their centre. They can be substituted at twelve different positions, eight pyrrolic β-positions and four *meso*-positions, and a coordination metal ion can also be inserted in the central cavity of porphyrins (**Figure 4A**). The core structure of porphyrins consists of twenty-six π-electrons, where eighteen π-electrons are involved in the main π-conjugation system, and four other π-electrons are exposed to saturation reactions and electrophilic additions reactions, hence the formation of porphyrin analogues such as chlorins and bacteriochlorins (**Figure 4B-C**) [39-42].

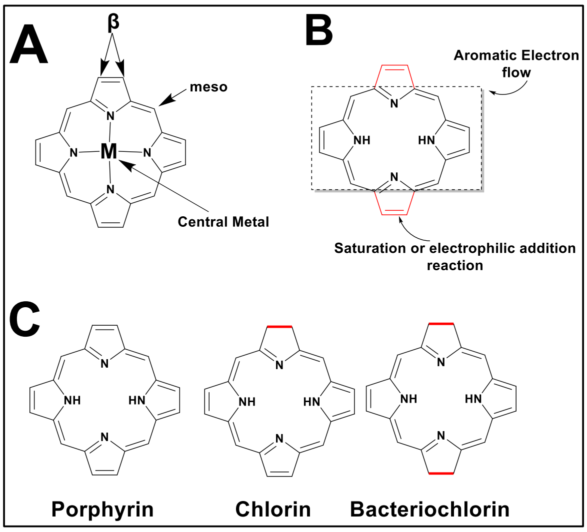

Figure 4. (A) Porphyrins *meso*, beta and central substitution. (B) Porphyrins aromatic electron flow and position at which the saturation or electrophilic addition reaction occurs. (C) Porphyrin analogues (Chlorin, Bacteriochlorin).

1.6 Porphyrin Synthesis

Several methods can be used to synthesise porphyrins. The Menotti and Rothemund [43], Adler-Longo [44] and Lindsey methods [45] are the most commonly used for *meso*-substituted porphyrins. These methods convert an aryl aldehyde (or aryl aldehydes) and pyrrole to a porphyrin through a condensation reaction, but their reaction conditions differ. The Alder-Longo method (**Figure 5**) was used for the porphyrin syntheses reported in this study. The aldehyde and pyrrole are refluxed in propionic acid at 140°C for 30 min to form the porphyrin

[44]. This method can be readily altered by reacting two aldehydes with different substituents and pyrrole to produce *meso*-substituted mono-, di-, tri- and tetra-substituted porphyrins. Despite the tedious purification process to obtain the porphyrin analogues, the other drawback with this method is that you obtain a mixture of di-substituted *cis*- and *trans*-porphyrin analogues, and it is difficult to separate the two isomers using column chromatography. Therefore, the di-substituted porphyrin product synthesised in this work is a mixture of the two isomers.

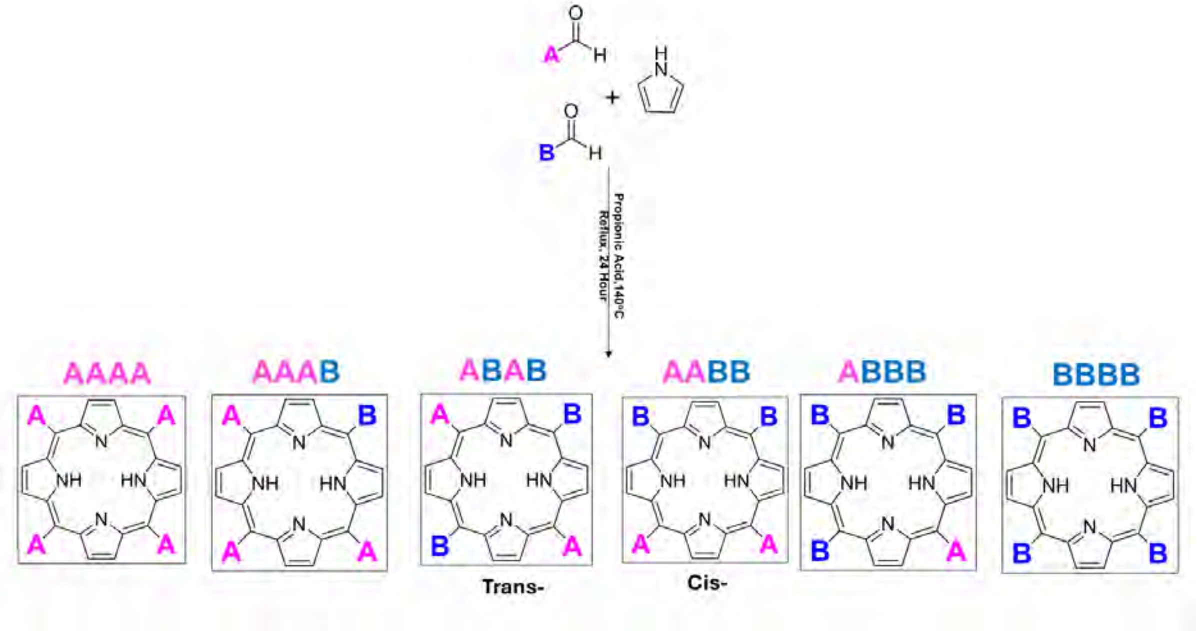

Figure 5. Adler-Longo reaction mechanism of porphyrin synthesis.

1.7 Porphyrin spectroscopy and electronic structure

The absorption spectrum of porphyrin is best understood and explained using the "four-orbital model" proposed by Martin Gouterman in the 1960s [39]. According to Martin Gouterman, the absorption spectrum of a free base porphyrin consists of an allowed B (or Soret) band in the blue/ultraviolet region (400 nm) and forbidden Q bands in the red/visible region (500−700 nm) [39], arising from the $\Delta M_L = \pm 1$ and ± 9 transitions associated with a 16 atom 18 π-electron system with an $M_L = 0, \pm 1, \pm 2, \pm 3, \pm 4, \pm 5, \pm 6, \pm 7, 8$ sequence in the MO energies in ascending energy terms (**Figure 6A**).

The band maxima of the B and Q bands can be modulated by modifying the substituents at the *meso* positions of the ligand and/or by inserting a metal ion into their central cavity. These bands in the porphyrin absorption spectrum arise from the transitions between the four frontier π-MOs. In the context of the D_{4h} symmetry of four-fold symmetric metal porphyrin complexes, the $M_L = \pm 4$ MOs associated with the HOMO of the $C_{16}H_{16}^{2-}$ parent perimeter transform as a_{1u} and a_{2u} (**Figure 6B**), while the $M_L = \pm 5$ MOs associated with LUMO transform as e_g* for symmetry reasons [46-47]. The angular nodal patterns of the degenerate e_{gx} and e_{gy} MOs are very similar and are rotated by 90° with respect to each other. In contrast, the accidentally degenerate a_{1u} and a_{2u} MOs (**Figure 6B**) lie on a different set of atoms.

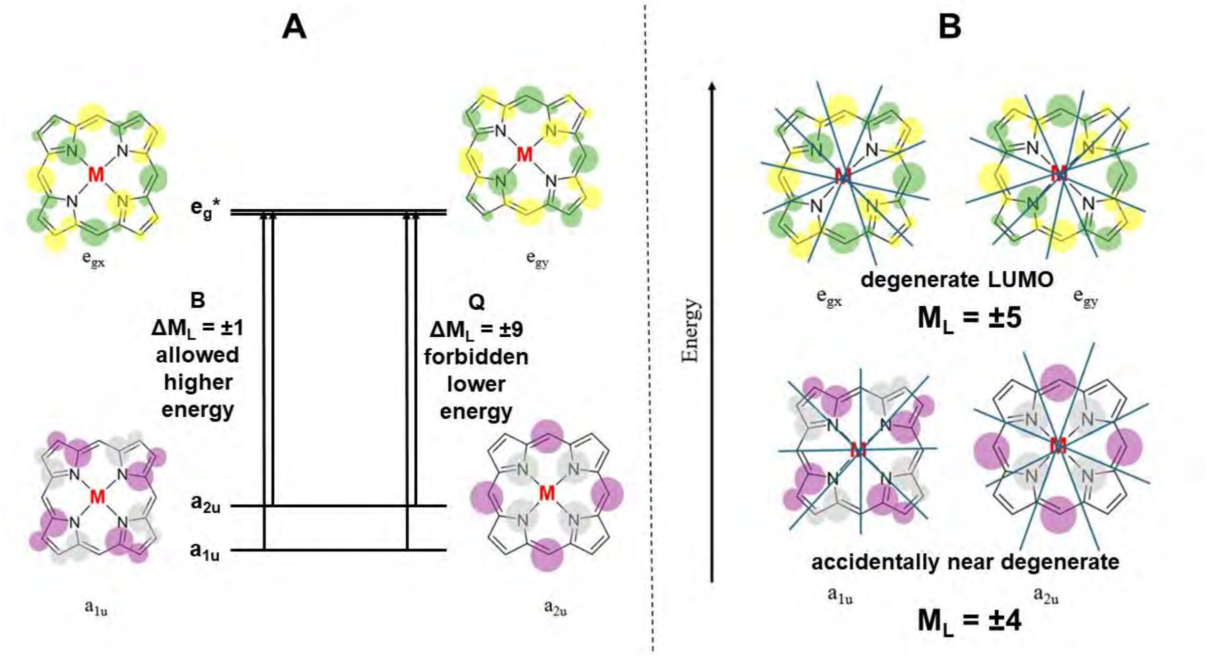

Figure 6. (a) The Gouterman HOMO and LUMO orbitals in porphyrins and the origin of the B and Q bands of porphyrins. (b) Degenerate and accidentally degenerate angular nodal patterns.

1.8 Unsaturated Porphyrin

When the pyrrolic ring structure of porphyrins is unsaturated, new porphyrin derivates are formed, such as chlorins or bacteriochlorins [48-51] (**Figure 2C**). The UV-visible spectra of chlorins and bacteriochlorins contain intense, red-shifted Q bands in the red region of the visible [48-51] (**Figure 7**). The longer the wavelength of the lower energy Q band of the PS dye, the deeper the penetration (**Figure 7**) of the laser light into tumour cells, which is an advantage in PDT/PACT [48-51]. The goal of this study is to use porphyrins to identify structural modifications that enhance the suitability of dyes for PDT and PACT, which can be applied to chlorins and bacteriochlorins in future.

1.9 Metalation of Porphyrin

When closed-shell coordination metal ions such as Mg(II) and Zn(II) are inserted into porphyrins, the four Q bands observed for the free base ligand are replaced by two spectral bands (**Figure 7**), since there is no longer a symmetry-related splitting of the main electronic band and its vibrational overtone [52-53]. If the porphyrin is substituted with a late transition metal ion, such as Co(II), Ni(II), Pd(II), and Cu(II), there is a hypso effect on the porphyrin absorption spectrum of porphyrins. The porphyrin Q and B bands are blue-shifted compared to the free base porphyrin spectrum due to mixing between the e_g* lowest unoccupied molecular orbital (LUMO) of the π-system and an e_g orbital formed by the $3d_{xz}$ and $3d_{yz}$ orbitals of the central metal ion [52-56]. In contrast, diamagnetic main group coordination metal ions, such as Sn(IV), Pb(II), As(III), Sb(III), and Bi(III), tend to have a hyper effect on the main spectral bands through a red shift of the main spectral bands [52-56] (**Figure 7**). Heavy main group ions, such as Sn(IV) and Pb(II), tend to increase the generation of singlet oxygen ($1O_2$) by boosting the kinetics of intersystem crossing (ISC) through spin-orbit coupling [52-56].

1.10 Phototherapeutic window

When the insertion of the metal ion results in a bathochromic shift of the Q band of the porphyrin photosensitiser dye deeper into the phototherapeutic window (620−850 nm) compounds, since there is increased tissue penetration because there is less absorption by endogenous chromophores and water in this spectral region (**Figure 7**). Other structural modifications of porphyrins, such as the preparation of chlorins and N-confused porphyrins [57-58], can also increase the suitability of the ligand for use in photodynamic therapy by shifting the absorption of the Q-bands into the phototherapeutic window [57-58]. This therapeutic window range is regularly used as a guideline on how best to synthesise molecules that would be PDT active.

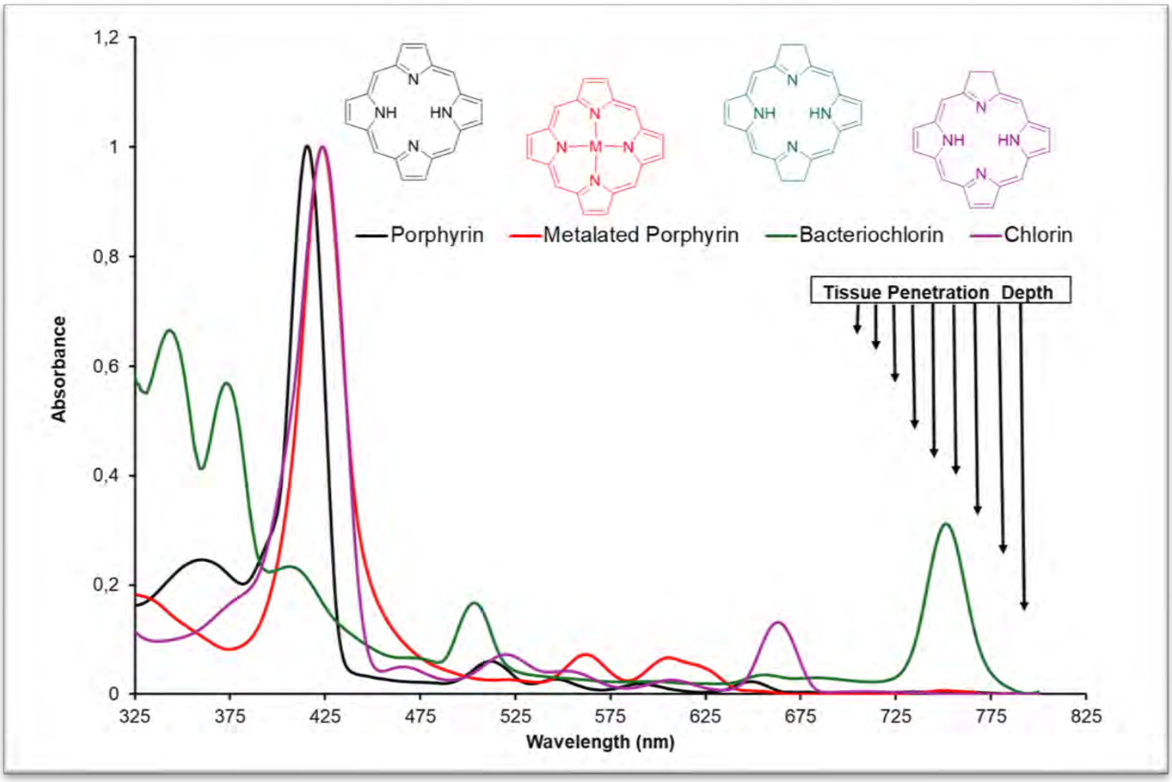

Figure 7. UV-visible absorption spectra of porphyrins, chlorins and bacteriochlorins.

1.11 Photophysical and Photochemical Parameters

The photophysiochemical properties of photosensitiser, such as the singlet oxygen quantum yield (Φ_Δ), fluorescence quantum yield (Φ_F), the triplet state lifetime (τ_T) and Stokes shift, are some of the essential parameters of the photosensitiser that are required to determine and predict the efficiency of the PS dye in biological applications, such as PDT and PACT.

1.12 Singlet Oxygen Quantum yield (Φ_Δ)

As illustrated in **Figure 3**, singlet oxygen is a cytotoxic species produced when the photosensitiser interacts with light, resulting in cell death during PDT. Therefore, singlet oxygen quantum yield can be defined as the number of molecules of singlet oxygen produced per quanta of light absorbed by the photosensitiser [59, 60]. Singlet oxygen quantum yield can be determined with a comparative method, which employs a known standard and a scavenger in DMSO. In this work, dimethyl anthracene (DMA) was used as a scavenger, and the amount of $^1O_2$ produced by the PS dye and known standard zinc tetraphenylporphyrin (ZnTPP) were compared using Equation 1.1 by plotting DMA absorbance against photoirradiation time [49]:

$$\Phi_{\Delta}=\Phi_{STD}\ (M_{sample}/M_{standard}) \qquad 1.1$$

Φ_{STD} is the singlet quantum yield of the standard (Φ_{STD}= 0.53, ZnTPP in DMSO [59, 60]), while M_{sample} and $M_{standard}$ are the slopes for the best-fit lines for the sample and standard solutions, respectively.

1.13 Triplet Lifetime

The excited photosensitiser undergoes intersystem crossing to the triplet state, producing singlet oxygen and ROS, as shown in **Figure 3** [61]. The average time the excited photosensitiser remains in the triplet state is known as the triplet lifetime, which can be determined and calculated by fitting the triplet decay curve with an exponential curve, since the τ_T value is defined as the time it takes for the triplet decay curve to reach 1/e of its initial value [61].

1.14 Fluorescence Quantum Yield

As the excited PS dye returns to the ground singlet state from the singlet excited state, the process is known as fluorescence [62]. The fluorescence quantum yield is defined as the ratio of the number of photons emitted to the number of photons absorbed. It can be determined and calculated by using a comparative method:

$$\Phi_F=\Phi_{F(STD)}\ (F.\ A_{STD}.\ n^2/\ F_{STD}.\ A.\ n^2_{STD})$$

Where $\Phi_{F(STD)}$ is the fluorescence quantum yield of the standard ($\Phi_{F(STD)}$ = 0.039 ZnTPP in DMSO) [63], F and F_{STD} are areas under the fluorescence emission curves of the sample and standard, A and A_{STD} are the absorbance values at the excitation wavelengths and n^2 and n^2_{STD} are the refractive indices of the solvents used.

1.15 Stokes shifts

The Stokes shift is the energy difference between the absorption and fluorescence band maxima associated with the $S_0 \rightarrow S_1$ and $S_1 \rightarrow S_0$ transitions, respectively. This energy gap is usually related to the stabilisation of the S_1 state as a result of internal conversion after photoexcitation and hence provides a measure of the rigidity of the structure in this context [64]. Solvent polarity can also influence the magnitude of the energy gap, since the solvation sphere will influence the internal conversion of the photoexcited molecules. The Stokes shift can be determined using Equation 1.2:

$$\Delta \bar{v} = \bar{v}_a - \bar{v}_f \qquad 1.2$$

Where $\bar{v}$ is the absorption maximum and $\bar{v}_f$ is the Fluorescence maximum.

1.16 Molecular docking

Molecular docking is the computational study of how proteins and ligands of interest (the PS dye) interact [65]. It guides and assists scientists in understanding the interaction of the PS dye when it is administered in the body. Through molecular docking, we can evaluate the pharmacokinetics of the porphyrinoids to gauge how effective they will be during *in vivo* PDT and PACT studies [66-70]. The protein of interest is human serum albumin (HSA), a predominant plasma protein that functions as a transport protein in the body. The molecular docking will evaluate the binding affinity of the PS dyes to HSA. The more negative the value for binding affinity, the higher the probability that the photosensitiser will bind to the HSA, which will increase the localisation and drug delivery of the PS dye to cancerous cells because there are HSA receptors on the surface of the cancerous and bacterial cells [66-70].

1.17 Aims and Objectives of this Thesis.

There is an ongoing need to identify and develop new treatments to diminish the mortality rate and increase life expectancy. The goal of the project is to prepare water-soluble porphyrinoids that are suitable for use as photosensitiser dyes in PDT and PACT. *In vitro* PDT and PACT activity studies will be carried out to assess the suitability of the 4-piperidinylphenyl-substituted tetraphenylporphyrin dyes **1-4** shown in **Scheme 1** for use as photosensitiser dyes in PDT and PACT. The sp^3-hybridised 4-piperidinylphenyl nitrogen atom can be readily quaternised with CH_3I to form water-soluble dyes **1-4-Q** (**Scheme 1**). An Sn(IV) ion can be inserted to form the **1-4-Sn** and water-soluble **1-4-Sn-Q** complexes (**Scheme 1**). A key advantage of inserting a Sn(IV) ion is that *trans*-axial ligation can hinder aggregation [49], which results in unfavourable photophysicochemical properties.

The annotations in Scheme 1:

1. Mono-4-piperidinylphenyl-substituted dyes and complexes **1**, **1-Q**, **1-Sn**, **1-Sn-Q** (Series 1)
2. Di-4-piperidinylphenyl-substituted dyes and complexes **2**, **2-Q**, **2-Sn**, **2-Sn-Q** (Series 2)
3. Tri-4-piperidinylphenyl-substituted dyes and complexes **3**, **3-Q**, **3-Sn**, **3-Sn-Q** (Series 3)
4. Tetra-4-piperidinylphenyl-substituted dyes and complexes **4**, **4-Q**, **4-Sn**, **4-Sn-Q** (Series 4)

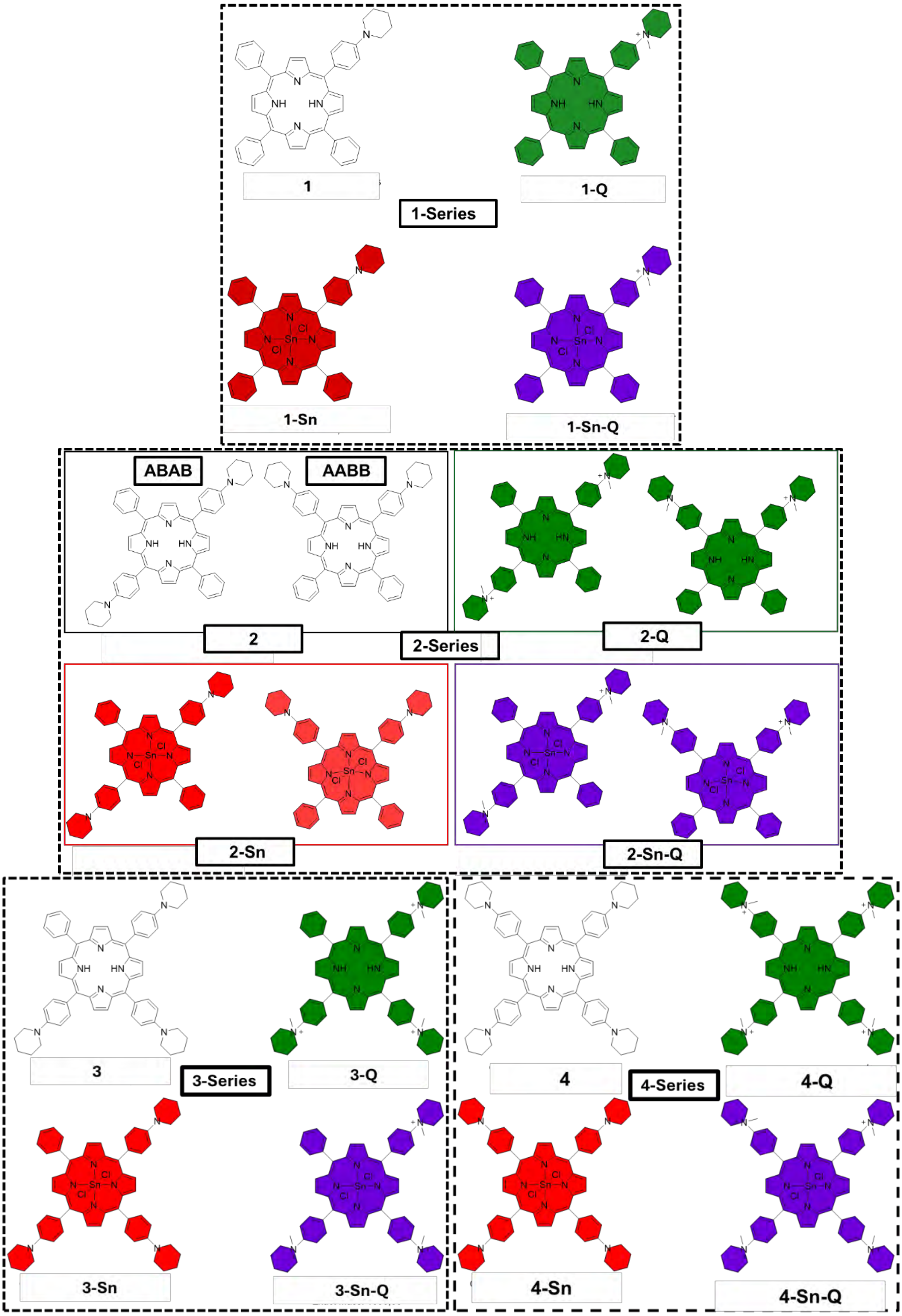

Scheme 1. Porphyrin analogues synthesised.

1.18 The aims and objectives of this work are summarised below:

1. To synthesise and characterise asymmetrical and symmetrical porphyrins, mono-, di-, tri- and tetra-*meso* substituted porphyrins.
2. Metalate and quaternise the porphyrinoids and characterise them by mass spectrometry, and UV-visible absorption and ^{1}H NMR spectroscopy.
3. Determine and compare their photophysiochemical properties, such as singlet quantum yield, fluorescence quantum yield, fluorescence and triplet lifetimes, photostability and lipophilicity, to determine their suitability for PDT and PACT.
4. Study the cytotoxicity and antibacterial activity of the selected porphyrinoids during PDT (MCF-7 cancer cell line) and PACT (*S. aureus* bacteria) activity studies.
5. Carry out time-dependent density functional theory (TD-DFT) calculations to understand the electron transition and spectroscopic properties of the porphyrinoids.
6. Carry out *in silico* docking using human serum albumin human mitochondria ABC transporter.

Chapter 2: Experimental

2.1 Reagents Used for the synthesis of porphyrins

4-(-1-Piperidinyl)benzaldehyde, benzaldehyde, distilled pyrrole, propanoic acid, iodomethane, tin(II) Chloride, zinc tetraphenylporphyrin (ZnTPP), 9,10-dimethylanthracence (DMA) were reagents used during porphyrin synthesis and characterisation. Chloroform, dichloromethane, N,N-dimethylformamide (DMF), dimethylsulfoxide (DMSO), and deuterated chloroform ($CDCl_3$) were solvents used in purification and spectroscopic analysis of the porphyrins. All reagents and solvents were purchased from Sigma-Aldrich.

2.2 Reagents used in PDT

Cultures of MDA cancer cells were obtained from Cellonex®, and 100 unit/mL penicillin−100 μg/mL streptomycin-amphotericin B (PSA) and 10% (v/v) heat-inactivated foetal bovine serum were obtained from Biowest®. Dulbecco's modified Eagle's medium (DMEM) and Dulbecco's phosphate-buffered saline (DPBS) were purchased from Lonza®.

2.3 Equipment

- ➢ Ground state UV-visible absorption spectra in the UV-visible region were recorded on a Shimadzu UV-2550 spectrophotometer.
- ➢ Fluorescence emission spectra were recorded on a Varian Eclipse spectrofluorometer.
- ➢ Mass spectral data were obtained with a Bruker AutoFLEX III Smart-beam TOF/TOF mass spectrometer in positive and negative ion modes by using α-cyano-4-hydroxycinnamic acid as the matrix.
- ➢ An Ekspla NT-342B laser system with an Nd:YAG laser pumping an optical parametric oscillator at 420−2300 nm and a Thermo Scientific Evolution 350 spectrophotometer were used to determine singlet oxygen quantum yields.
- ➢ The triplet state lifetime values were obtained in DMSO at 500 nm on an Edinburgh Instruments LP980 spectrometer. An Ekspla NT-342B laser equipped with an OPO

provided excitation wavelengths (2.0 mJ excitation energy, 7 ns pulse duration and a 20 Hz repetition rate).

- The bioillumination kit of a Modulight® 7710-680 medical laser system was used during PDT and PACT studies by mounting a 595 nm LED (Thorlabs M595L3). Irradiance values were determined with a Coherent FieldMax II Top laser power/energy meter.
- ^{1}H NMR spectra were measured using Bruker 85 and 400 MHz instruments.
- A Clariostar microplate reader was used to analyse output data for the PDT and PACT assays.
- Colony Forming units (CFU)/ml values for PACT studies were evaluated using the Scan 500 automatic colour colony counter.

2.4 Porphyrin Synthesis

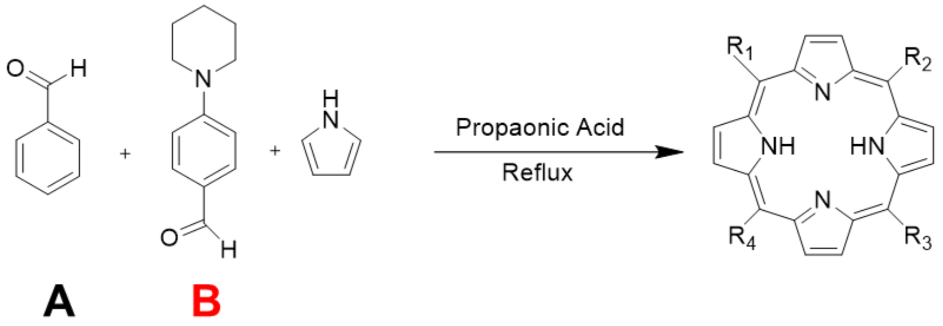

Porphyrin	R1	R2	R3	R4
1 (AAAB)	A	A	A	B
2 (AABB)	A	A	B	B
2 (ABAB)	A	B	A	B
3 (ABBB)	A	B	B	B
4 (BBBB)	B	B	B	B

Scheme 2. Porphyrin analogues synthetic pathway.

The free base porphyrin analogues were synthesised using the Adler-Longo procedure, with few alterations, 1:1:3 molar ratio, 4-(-1-piperidinyl)-benzaldehyde: benzaldehyde: distilled pyrrole respectively [44]. A solution of 4-(-1-piperidinyl)-benzaldehyde (0.5 g), benzaldehyde (1.3 mg), distilled pyrrole and propanoic acid (80 ml) was refluxed for 24 h and then cooled to room temperature (Scheme 1). A NaOH solution was added to the porphyrin solution, and the colour changed from black to dark purple. The product was filtered and dried. The product was then purified through column chromatography (silica gel) using chloroform ($CHCl_3$) as eluent. The porphyrin with the lowest molecular weight (mono-substituted porphyrin **1**) gets eluted first, and the product with the highest molecular weight (tetra-substituted porphyrin **4**) is eluted at the end. Porphyrin **2** was eluted as a mixture of isomers (*cis* and *trans*, i.e. AABB and ABAB, respectively)

1. [$C_{49}H_{39}N_5$] 1H NMR (400 MHz, CDCl3) δ 8.82 (d, J = 7.0 Hz, 8H), 8.21 – 7.98 (m, 8H), 7.77 (d, J = 3.5 Hz, 7H), 6.54 (d, J = 11.1 Hz, 4H), 3.53 (d, J = 14.4 Hz, 4H), 1.33 (s, 4H), 0.76 (s, 2H), -2.79 (s, 2H). MALDI-TOF. m/z: 697.88; obtained: 699.90 $[M+2H]^+$. Yield: 40 mg (22%). Purple Crystals.

2. [$C_{54}H_{48}N_6$] ^{1}H NMR (400 MHz, $CDCl_3$) δ 8.87 (d, J = 7.5 Hz, 8H), 8.52 – 7.27 (m, 14H), 7.27 (s, 4H), 3.47 (t, J = 16.1 Hz, 8H), 1.58 (s, 8H), 0.86 (d, J = 5.4 Hz, 4H), -2.69 (s, 2H). MALDI-TOF. m/z: 781.02; obtained: 781.71 $[M+H]^+$. Yield: 73 mg (40%).Purple crystals.

3. [$C_{59}H_{57}N_7$] ^{1}H NMR (80 MHz, $CDCl_3$) δ 8.91 – 8.23 (m, 8H), 8.16 – 7.61 (m, 6H), 7.47 – 7.20 (m, 5H), 7.07 – 6.50 (m, 6H), 4.56 – 1.87 (m, 12H), 1.53 (d, J = 10.1 Hz, 12H), 0.76 (d, J = 4.7 Hz, 6H), -2.76 (s, 2H). MALDI-TOF. m/z 864.15; obtained: 863.04 $[M-H]^-$. Yield: 23 mg (12%). Brown-Red powder.

4. [$C_{64}H_{66}N_8$] ^{1}H NMR (400 MHz, $CDCl_3$) δ 8.94 (m, 8H), 8.51 – 7.95 (m, 8H), 7.18 – 6.43 (m, 8H), 3.51 (d, J = 4.6 Hz, 16H), 1.46 (d, J = 4.4 Hz, 16H), 0.90 (d, J = 6.2 Hz, 8H), -2.63 (s, 2H). MALDI-TOF. m/z 947.28; obtained: 948.07 $[M+H]^+$. Yield: 27 mg (15%). Black crystals.

2.5 Sn-Porphyrin Synthesis

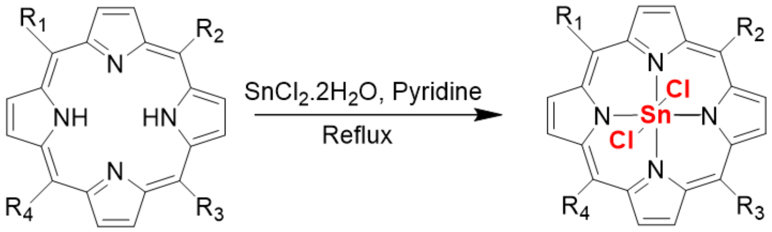

Porphyrin	R1	R2	R3	R4
1-Sn (AAAB)	A	A	A	B
2-Sn (AABB)	A	A	B	B
2-Sn (ABAB)	A	B	A	B
3-Sn (ABBB)	A	B	B	B
4-Sn (BBBB)	B	B	B	B

Scheme 3. Sn (IV) porphyrin synthetic pathway.

1, **2**, **3** and **4** (100 mg) were dissolved in pyridine, and excess tin(IV) (1.5 g) chloride was added [49, 51]. The solution was refluxed for 3 h and then cooled to room temperature. The solution of water and chloroform was used to extract the metalled porphyrin analogues, which dissolved in chloroform (organic layer) and the unreacted tin(IV) chloride salt dissolved in water. The chloroform that contained the product was evaporated under fumehood. The crude product obtained was purified using silica gel chromatography and 2:1 chloroform/methanol as the solvent system to obtain **1-Sn**, **2-Sn**, **3-Sn** and **4-Sn**.

1-Sn. [$C_{49}H_{37}Cl_2N_5Sn$] ^{1}H NMR (400 MHz, $CDCl_3$) δ 10.12 – 8.19 (m, 8H), 7.75 (dt, J = 7.6, 2.2 Hz, 10H), 7.05 (d, J = 8.3 Hz, 2H), 6.74 (d, J = 8.3 Hz, 2H), 4.03 (s, 4H), 1.19 (s, 7H), 0.83 – 0.76 (m, 4H). MS (MALDI-TOF) m/z 885.14, obtained: 850.21 $[M{-}Cl]^+$ [Calcd for $C_{54}H_{46}ClN_6Sn$: 850.04]. Yield: 80 mg (88%) as a green powder.

2-Sn. [$C_{54}H_{46}C_{l2}N_6Sn$] ^{1}H NMR (80 MHz, $CDCl_3$) δ 9.47 – 8.79 (m, 8H), 7.98 (d, *J* = 36.3 Hz, 14H), 7.38 – 7.19 (m, 4H), 3.54 (s, 8H), 2.16 (s, 8H), 0.70 (s, 4H). MS (MALDI-TOF) m/z:

968.64, obtained: 933.66 [M−Cl]$^+$ [Calcd for $C_{54}H_{46}ClN_6Sn$: 933.17]. Yield: 80 mg (92%) as a green powder.

3-Sn. [$C_{59}H_{55}Cl_2N_7Sn$] ^{1}H NMR (400 MHz, $CDCl_3$) δ 8.55 – 8.23 (m, 8H), 7.32 – 7.98 (m, 6H), 7.07 – 6.50 (m, 5H), 4.32 – 1.98 (m, 18H), 1.22 (d, J = 9.1 Hz, 12H), 0.65 (d, J = 4.7 Hz, 6H). Yield: 53 mg (70%) as a green powder.

4-Sn. [$C_{64}H_{64}Cl_2N_8Sn$]] ^{1}H NMR (400 MHz, $CDCl_3$) δ 9.21 – 9.04 (m, 8H), 8.24 (q, *J* = 2.2 Hz, 8H), 7.81 – 7.69 (m, 8H), 4.26 – 3.99 (m, 16H), 2.36 – 1.40 (m, 16H), 0.82 (d, *J* = 6.5 Hz, 8H). MS (MALDI-TOF) m/z: 1134.90; obtained: 1099.76 [M−Cl]$^+$ [Calcd for $C_{64}H_{64}N_6Sn$: 1099.44]. Yield: 50 mg (60%) as a green powder.

2.6 Porphyrin Methylation synthesis

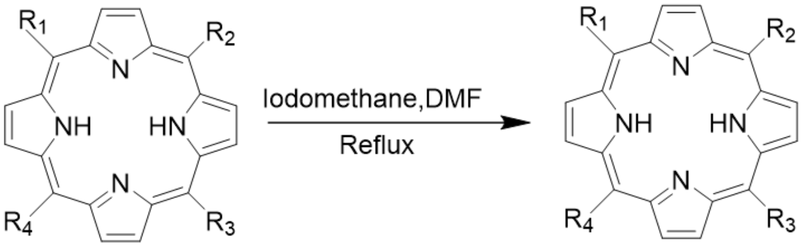

Porphyrin	**R1**	**R2**	**R3**	**R4**
1-Q (AAAB)	**A**	**A**	**A**	**B+**
2-Q (AABB)	**A**	**A**	**B+**	**B+**
2-Q (ABAB)	**A**	**B+**	**A**	**B+**
3-Q (ABBB)	**A**	**B+**	**B+**	**B+**
4-Q (BBBB)	**B+**	**B+**	**B+**	**B+**

Scheme 4. Free base quaternised porphyrin analogues synthetic pathway.

Free base porphyrins **1**, **2**, **3** and **4** (100 mg) were dissolved in dry N,N-dimethylformamide (DMF) and excess iodomethane was added to the solution [71, 72]. The solution was vigorously mixed at room temperature for 24 h and refluxed. Quaternised porphyrin analogues **1-Q**, **2-Q**, **3-Q** and **4-Q** were obtained from the solution by evaporating the DMF organic solvent with a rotary evaporator.

1-Q. $[C_{50}H_{42}N_5]^+$ ^{1}H NMR (400 MHz, CDCl$_3$) 8.71 (m, 8H), δ 7.20 (s, 15H), 7.06 (d, *J* = 8.0 Hz, 2H), 6.75 (d, *J* = 8.2 Hz, 2H), 4.04 (s, 4H), 3.09 (d, *J* = 1.5 Hz, 3H), 1.56 (s, 4H), 0.77 (d, *J* = 4.1 Hz, 2H), -2.85 (s, 2H). MALDI-TOF m/z: 712.34; obtained: 712.54 $[M]^+$ [Calcd for $C_{49}H_{39}N_5$: 1099.44]. Yield: 89 mg (95%) as a purple powder.

2-Q. $[C_{56}H_{54}N_6]^{2+}$ ^{1}H NMR (400 MHz, CDCl$_3$) δ 7.71 (d, *J* = 47.2 Hz, 8H), 7.06 (d, *J* = 8.1 Hz, 18H), 6.76 (s, 8H), 3.94 (d, *J* = 6.1 Hz, 8H), 3.38 (s, 6H), 1.24 (d, J = 6.8 Hz, 4H), -2.36 (s, 2H). MALDI-TOF m/z 811.09; obtained: 795.78 $[M{-}CH_3]^+$ [Calcd for $C_{55}H_{51}N_6$: 796.05]. Yield: 80 mg (82%) as a purple powder.

3-Q. $[C_{62}H_{66}N_7]^{3+}$ ^{1}H NMR (400 MHz, CDCl$_3$) δ 7.84 (s, 8H), 7.46 (s, 5H), 7.20 (s, 6H), 6.75 (d, *J* = 8.2 Hz, 6H), 4.15 – 3.81 (m, 12H), 3.39 (s, *J* = 9.3 Hz, 9H), 2.69 (m, 12H), 1.56 (m, 6H), -2.15 (s, 2H). MALDI-TOF m/z: 908.54, obtained: 879.90 $[M{-}2CH_3]^+$ Yield: 50 mg (59%) as a purple powder.

4-Q. $[C_{68}H_{78}N_8]^{4+}$ ^{1}H NMR (400 MHz, CDCl$_3$) δ 7.05 (d, *J* = 7.9 Hz, 4H), 6.75 (d, *J* = 8.2 Hz, 8H), 4.04 (s, 8H), 2.87 (d, *J* = 9.2 Hz, 6H), 2.74 (s, 8H), 0.91 – 0.79 (m, 4H), -1.59 (s, 2H). MALDI-TOF m/z 1006.63; obtained: 962.97. Yield: 90 mg (98%) as a purple powder.

2.7 Sn-Porphyrin Methylation synthesis

Sn(IV) porphyrins **1-Sn**, **2-Sn**, **3-Sn** and **4-Sn** (100 mg) were dissolved in dry N,N-dimethylformamide (DMF) and excess iodomethane was added to the solution [71, 72]. The solution was vigorously mixed at room temperature for 24 h. The quaternised porphyrin analogues crude product of **1-Sn-Q**, **2-Sn-Q**, **3-Sn-Q** and **4-Sn-Q** were obtained from the solution by evaporating the DMF organic solvent with a rotary evaporator.

1-Sn-Q. $[C_{50}H_{40}Cl_2N_5Sn]^+$ ^1H NMR (400 MHz, $CDCl_3$) δ 9.28 – 9.08 (m, 8H), 7.5 – 7.77 (m, 15H), 7.04 (s, 2H), 6.74 (d, *J* = 8.3 Hz, 2H), 4.03 (s, 4H), 2.89 (s, 3H), 1.18 (s, 4H), 0.81 (s, 2H). MALDI-TOF m/z 900.54; obtained: 831.49 $[M-2Cl+H]^+$ [Calcd for $C_{50}H_{41}N_5Sn$: 830.62]. Yield: 90 mg (96%) as a green paste.

2-Sn-Q. $[C_{56}H_{52}Cl_2N_6Sn]^{2+}$ ^1H NMR (400 MHz, $CDCl_3$) δ 9.17 (s, 8H), 8.24 (s, 14H), 7.77 (s, 12H), 4.13 (d, *J* = 3.7 Hz, 8H), 3.29 (s, 6H), 2.20 (dd, *J* = 60.4, 6.4 Hz, 4H). MALDI-TOF m/z 998.70; obtained: 942.29 $[M-C_4H_8]^+$ [Calcd for $C_{52}H_{44}N_6Cl_2Sn$: 942.60]. Yield: 85 mg (89%) as a green paste.

3-Sn-Q. $[C_{62}H_{64}Cl_2N_7Sn]^{3+}$ ^1H NMR (400 MHz, $CDCl_3$) δ 7.95 (m, 8H), 7.64 (m, 6H), 7.46 (m, *J* = 9.8 Hz, 5H), 6.93 (m, 6H), 5.75 (dd, *J* = 17.2, 10.2 Hz, 12H), 2.89 (m, 9H), 2.36 – 1.83 (m, 12H), 1.18 (m, 6H) . Yield: 78 mg (83%) as a green paste.

4-Sn-Q. $[C_{68}H_{76}Cl_2N_8Sn]^{4+}$ ^1H NMR (400 MHz, $CDCl_3$) δ 7.95 (m, 8H), 7.69 – 7.33 (m, 8H), 7.10 – 6.67 (m, 8H), 4.89 (dd, *J* = 25.9, 13.7 Hz, 16H), 2.55 (d, 16H), 2.28 (t, *J* = 7.6 Hz, 12H), 1.15 (s, 8H). Yield: 89 mg (93%) as a green paste.

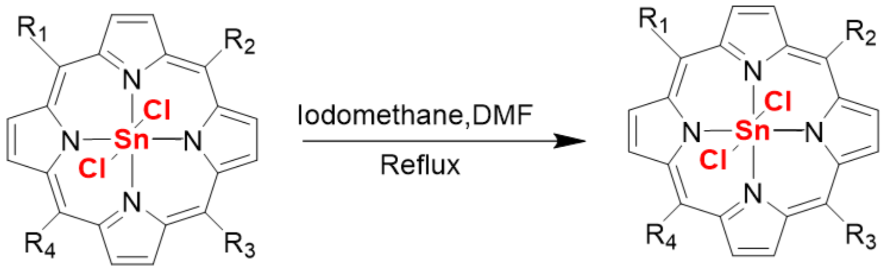

Porphyrin	R1	R2	R3	R4
1-Sn-Q (AAAB)	A	A	A	B+
2-Sn-Q (AABB)	A	A	B+	B+
2-Sn-Q (ABAB)	A	B+	A	B+
3-Sn-Q (ABBB)	A	B+	B+	B+
4-Sn-Q (BBBB)	B+	B+	B+	B+

Scheme 5. Quaternised Sn (IV) porphyrin porphyrin analogue synthetic pathway.

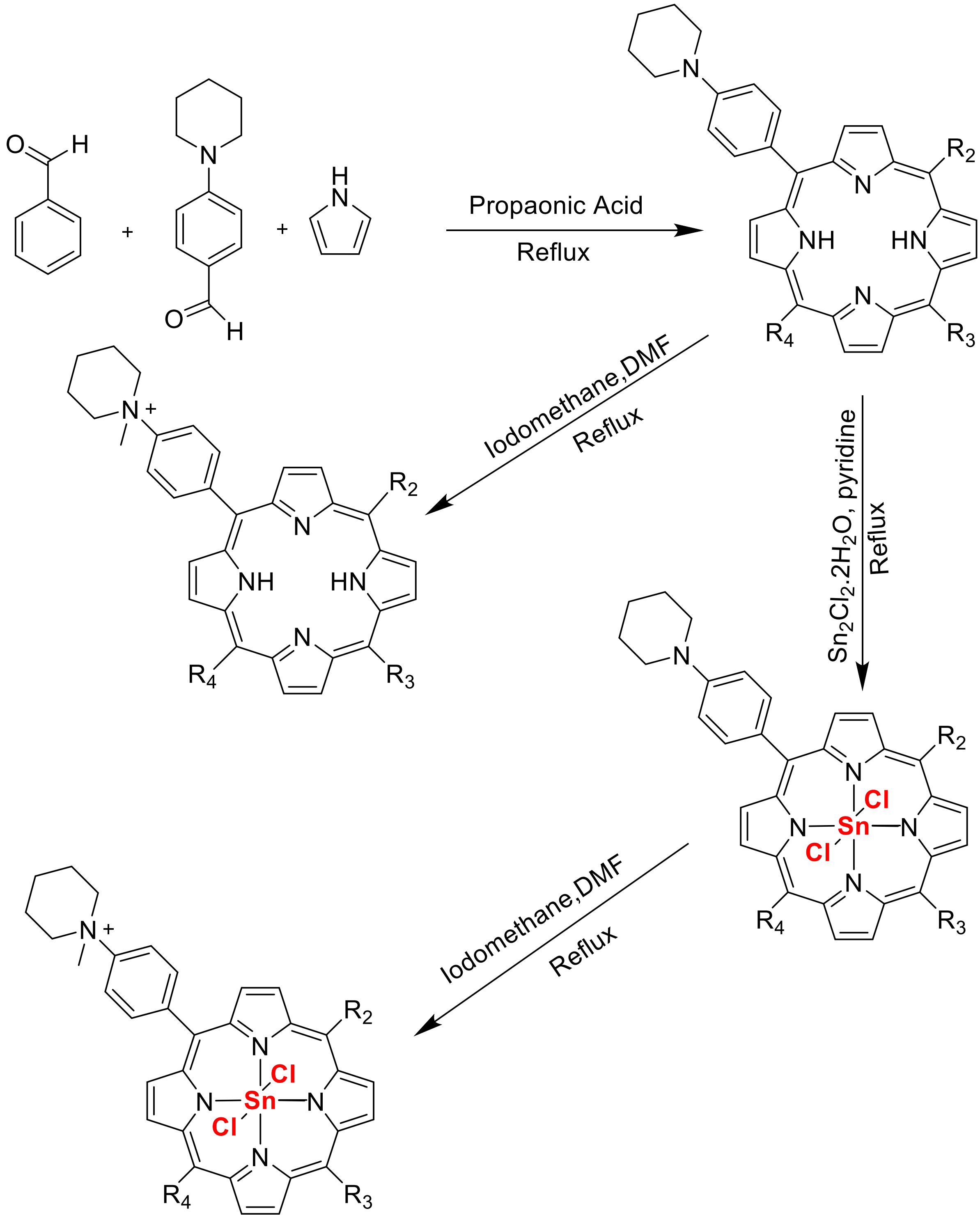

Scheme 6. Synthetic summary of porphyrin analogues.

2.8 Photophysiochemical Properties

- **The singlet oxygen quantum yield** (Φ_Δ) values were determined with a comparative method in DMSO using DMA as a singlet oxygen scavenger and ZnTPP as the standard ($\Phi_\Delta = 0.53$).
- **Fluorescence quantum yield** (Φ_F) values were also determined in DMSO with a comparative method using ZnTPP as the standard ($\Phi_F = 0.039$ in DMSO).
- **Decay curves for the triplet state lifetime** values were determined in spectroscopic DMSO. The values were determined by exponential fitting.
- **Lipophilicity values**

The lipophilicity values were determined in octanol/water solution by the shake flask method [73]. The absorbance of the solution that contains porphyrin analogue (1 mg in 10 ml) in octanol was measured and recorded as before. Thereafter, 3 ml of the octanol solutions were mixed with 3 ml of deionised water, and the mixtures were shaken at room temperature for 3 h. The solutions were then set aside to allow the two layers to separate (octanol/water) for 30 min. The octanol solution absorption was measured and reordered as A_{After}. The lipophilicity values (Log $P_{o/w}$) were calculated using the Equations 2 and 3:

$$A_{Water} = A_{Before} - A_{After} \tag{2}$$

$$P = \log (A_{After} / A_{Water}) \tag{3}$$

- **Photostability**

Photostability values were determined in 1% DMSO in PBS. 1 mg of the porphyrin is dissolved in 1% DMSO/PBS solution, and the solution is irradiated for 1 h (UV-visible absorption spectra were recorded after 15, 30, 45 and 60 min time intervals) like the excitation in PACT and PDT studies. The photoirradiation conditions were kept constant to monitor the stability of the porphyrin during *in vitro* PACT and PDT studies.

2.9 PDT cytotoxicity studies

The *in vitro* cytotoxicity studies were performed using the MDA cancer cell lines. The cells were seeded into 96-well plates to ~10 000 cells/ well and incubated for 24 h in culture media (DMEM with 4.5 g/ L glucose with L-glutamine and phenol red, supplemented with 10% FBS and 1% PSA, v/v) in a 37 °C and ~5% CO_2 humidified atmosphere. The cells were thereafter incubated with the porphyrinoids at varied concentrations (0−100 µM in 1% DMSO/water) and incubated for a further 24 h. The cells were then washed with DPBS to remove unabsorbed Free-base/metalated porphyrin, and 100 ul of DMEM clear (without phenol red) was added. The cells were then exposed to light (PDT studies) with a 595 nm LED (Thorlabs 595L3, dose: 9.0 mJ.cm^{-2} at the well-plate) and irradiated for 1 h. The irradiation kit of a Modulight 7710-680 medical laser system can hold a 96-well tissue culture plate with dimensions of 127.76 × 85.48 mm^2. For dark toxicity experiments, the cells were incubated with the free base and metalated porphyrins but were not exposed to LED light.

2.10 PDT cellular uptake

The cells were cultured following the method defined above. The cells were exposed to the porphyrins at the PDT test concentrations and incubated for 24 h. The cells were washed with DPBS, and 100 µL of DMSO was added to each well and left to stand for 1 h to dissolve the porphyrins in the cells. The absorbance of the porphyrins in each well was recorded at 560 nm.

2.11 PACT activity studies

The *in vitro* PACT activity studies were carried out using Gram-(+) *Staphylococcus aureus* (*S. aureus*) bacteria. The *S. aureus* bacteria was prepared in nutrient broth (5 ml) and incubated at 37 °C for 18 h with shaking. Thereafter, the optical density (OD) value of the bacteria was measured. Maturation growth was stopped once the OD value was between 0.6–0.8. The bacteria were collected by centrifugation and washed with PBS. The collected bacteria were then diluted in PBS (100 ml) to prepare a bacterial stock suspension with a dilution factor of 10^{-2}.

The bacteria suspension with a dilution factor of 10^{-4} and between 30–300 CFU/ml was prepared from the stock solution and then used for these studies.

The concentration optimisation studies were then analysed using the porphyrins in 1% DMSO/PBS at 0−100 μM range, and 25 μM was determined to be the optimal concentration used for further studies. The bacteria (*S. aureus*) solution (10^{-4}) and PS dyes (25 μM) were used to prepare bacterial-PS dye solutions (2.5 ml).

The bacterial-PS dye solutions were irradiated for 90 min with a 595 nm LED (Thorlabs595L3, dose: 13.5 mJ.cm^{-2} at the well-plate) or kept in the dark (for dark cytotoxicity studies) with aliquots for analysis taken at 15 min intervals for 90 min. The dark and irradiated bacterial-PS solutions (100 μL) were inoculated into nutrient agar at each time interval. Thereafter, they were incubated at 37 °C for 18 h with shaking. The CFU values for the colonies were measured using a 500 Automatic Colony Counter from Healthcare Technologies.

2.12 Molecular Modelling

A molecular modelling program, ArgusLab, was used to build the molecular structures of the porphyrin analogues and generate input files. The geometries of the structures were optimised by Gaussian 09 software on the lengau cluster at the Centre for High Performance Computing in Cape Town, using the B3LYP exchange-correlation functional and SDD basis sets. The optimised geometries of porphyrins were then used for time-dependent density functional theory (TD-DFT) calculations, which were conducted using the CAM-B3LYP functional [74]. Thereafter, TD-DFT calculations were used to generate calculated spectra and molecular orbital energy diagrams. The molecular orbital energy diagrams were visualised using Chemcraft and Avogadro.

2.13 Molecular docking

Autodock Vina software was used for the docking studies. The Human Serum Albumin (HSA: 1N5U) protein was retrieved from the RCSB protein data bank. The protein was prepped, and the active site xyz-grid coordinates were determined using AutoDock tools. The porphyrin analogue ligands were also prepped using Autodock software, and the best conformational was used for docking. The porphyrin analogues were docked onto the HSA protein with Autodock Vina software, and the data were analysed and visualised using Biovia Discovery Studio Visualizer 2020. ADMETlab 2.0 was used to predict the pharmacokinetic properties of the porphyrin analogues, which is a web-based application for predicting ADMET properties accurately

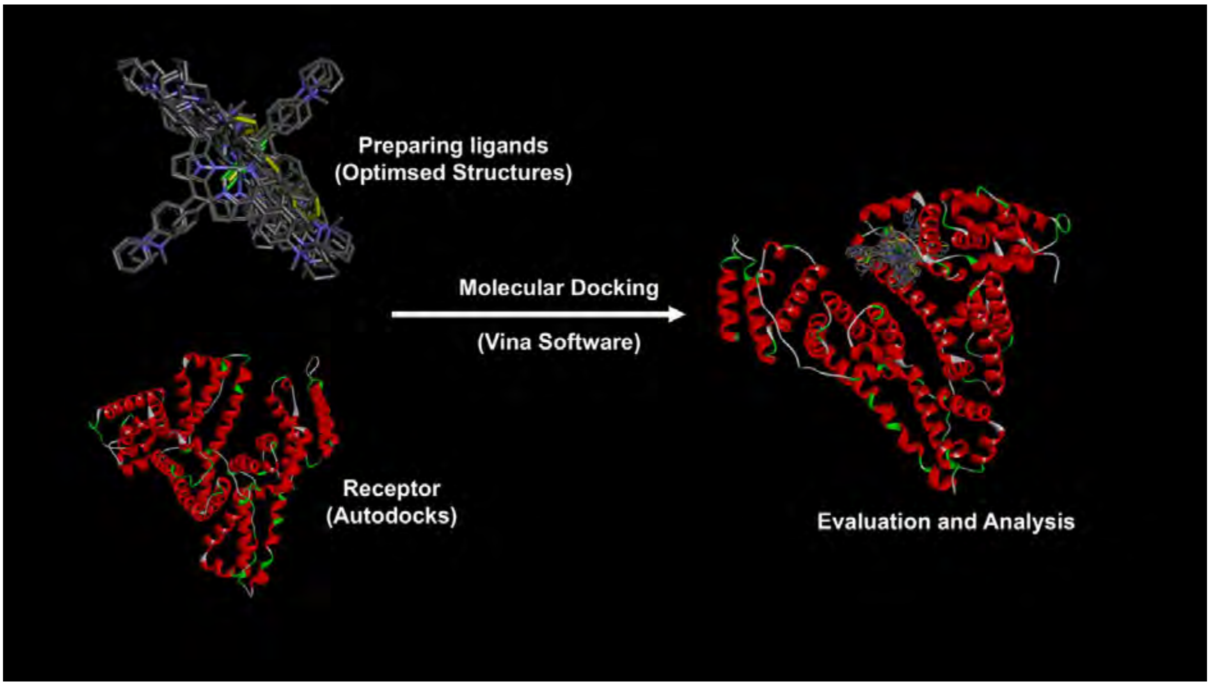

Scheme 7. Molecular Docking.

Concluding Remarks

The novel porphyrin analogues were successfully synthesised, although there was almost certainly a mixture of AABB and ABAB isomers present in the context of Series 2. The porphyrin analogues were characterised by UV-visible spectroscopy, mass spectroscopy and ^1H NMR. Their photophysiochemical properties were determined, and their pharmacological properties were also predicted using software.

Chapter 3: Characterisation

Characterisation

MALDI-TOF MS, UV-visible and ^{1}H NMR spectroscopy were used to confirm the successful syntheses of porphyrin analogues. The dyes were found to aggregate significantly in polar solvents such as DMSO, so no attempt was made to calculate molar extinction coefficients.

3.1. MALDI-TOF Mass Spectrometry

The method of porphyrin analogue synthesis used in this work was a one-pot synthesis where porphyrin analogues were obtained through column chromatography. The fractions were then spotted for MALDI-TOF mass spectrometry to determine the molecular weights of the specific porphyrin analogues. Broad m/z ranges were examined (**Figures 8-20**) to provide evidence that the mono-, di-, tri- and tetrasubstituted target products has been successfully separated. Despite repeated attempts only matrix-related MALDI-TOF MS peaks were observed for **3-Sn**, **3-Sn-Q** and **4-Sn-Q**.

Series 1 MS data

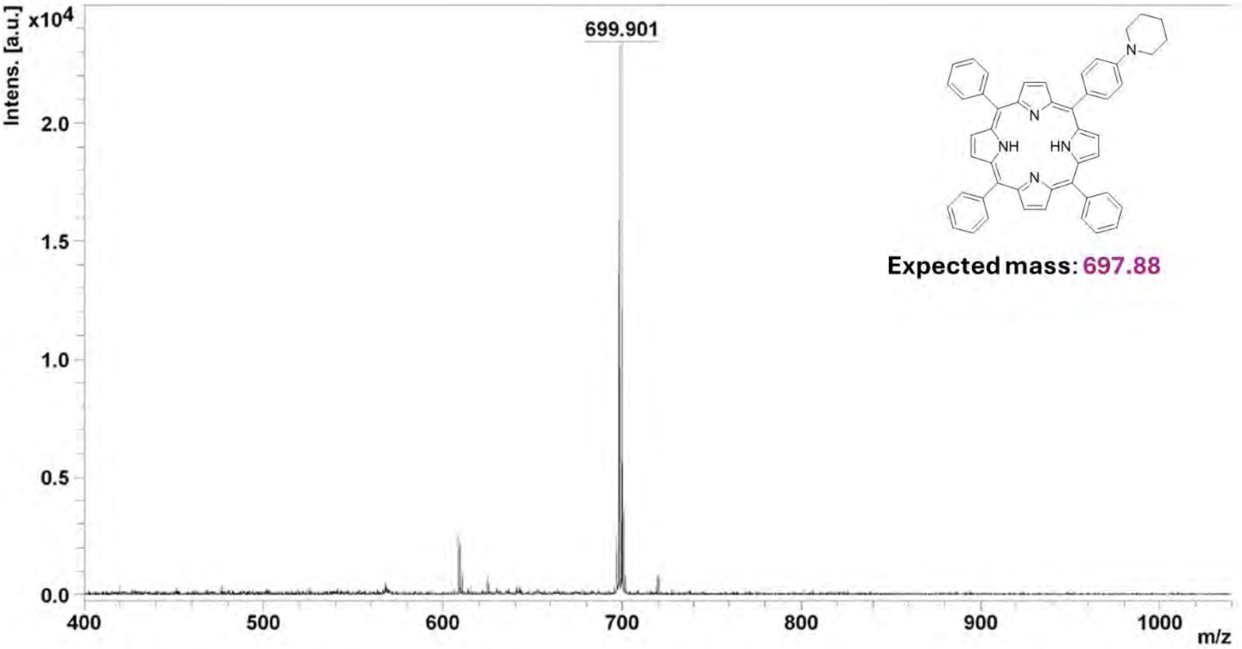

Figure 8. MALDI-TOF MS data for **1**.

The MALDI-TOF MS peak observed for **1** at 699.90 m/z corresponds to an $[M+2H]^+$ peak (**Figure 8**).

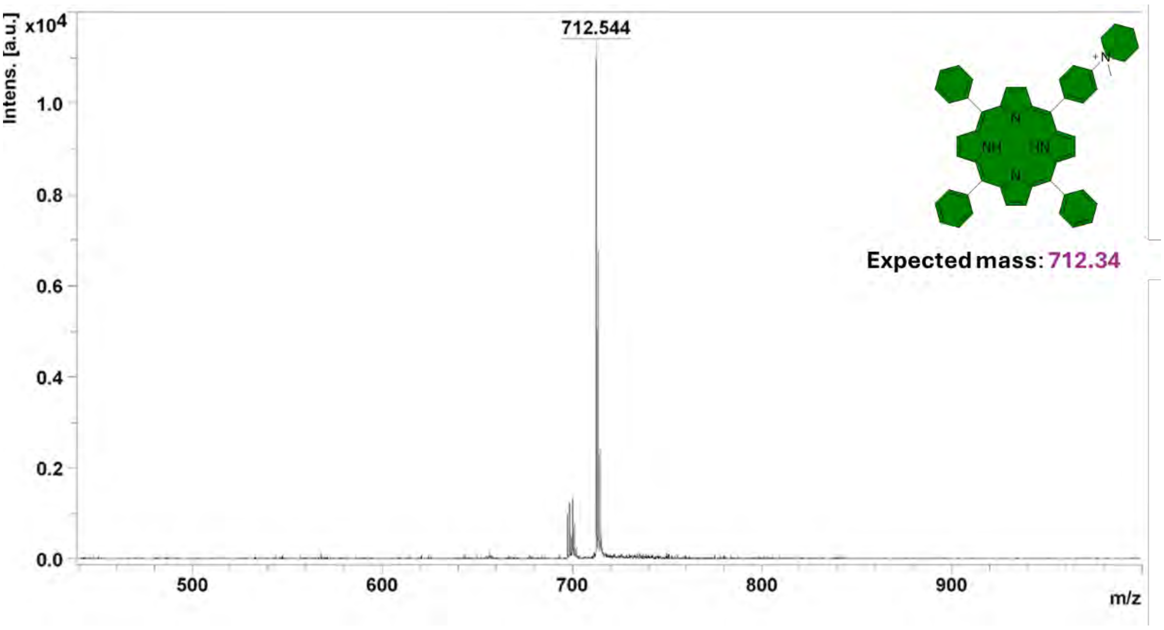

Figure 9. MALDI-TOF MS data for **1-Q**.

The MALDI-TOF MS peak observed for **1-Q** at 712.54 m/z corresponds to an $[M]^+$ peak (**Figure 9**).

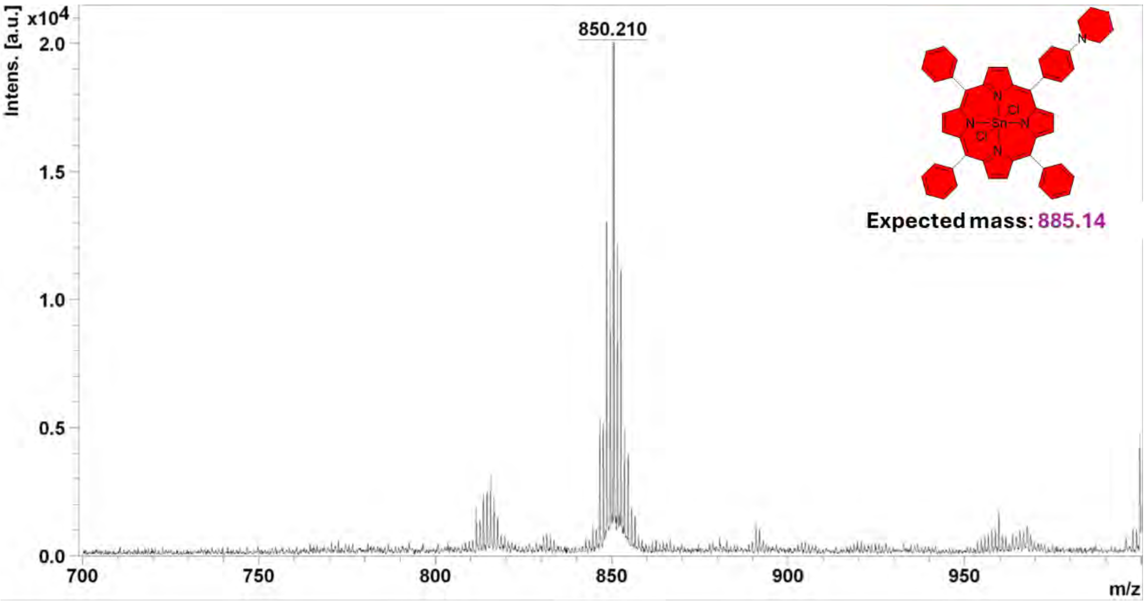

Figure 10. MALDI-TOF MS data for **1-Sn**.

The MALDI-TOF MS peak observed for **1-Sn** at 850.21 m/z corresponds to a $[M-Cl]^+$ peak (**Figure 10**).

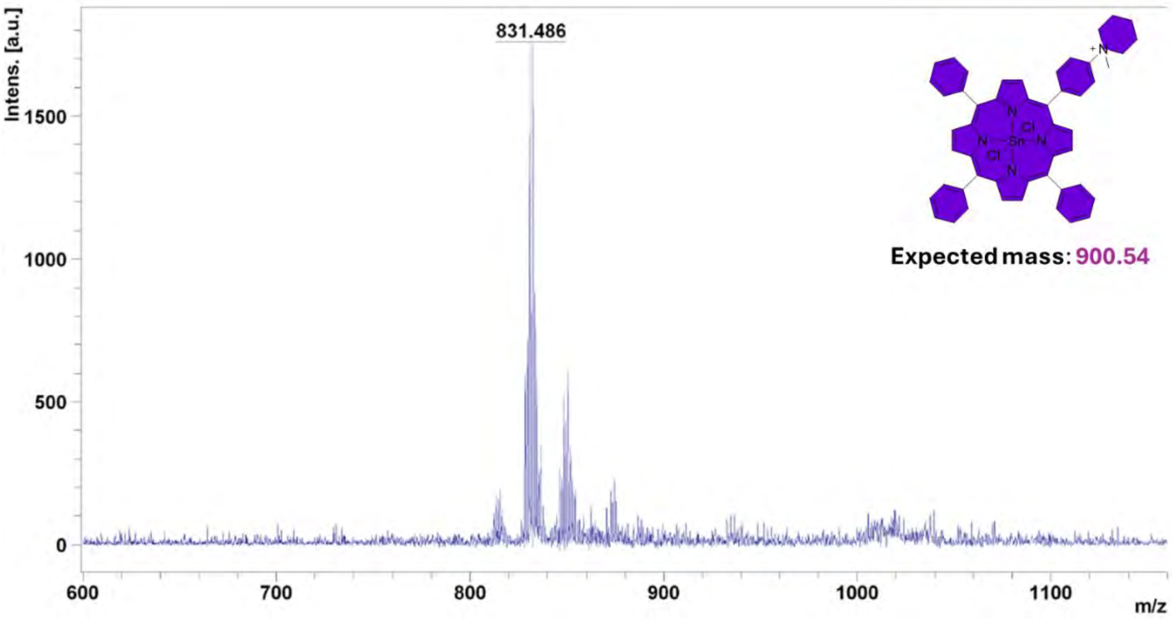

Figure 11. MALDI-TOF MS data for **1-Sn-Q**.

The MALDI-TOF MS peak observed for **1-Sn-Q** at 831.49 m/z corresponds to a [M−2Cl+H]$^+$ peak (**Figure 11**).

Series 2 MS data

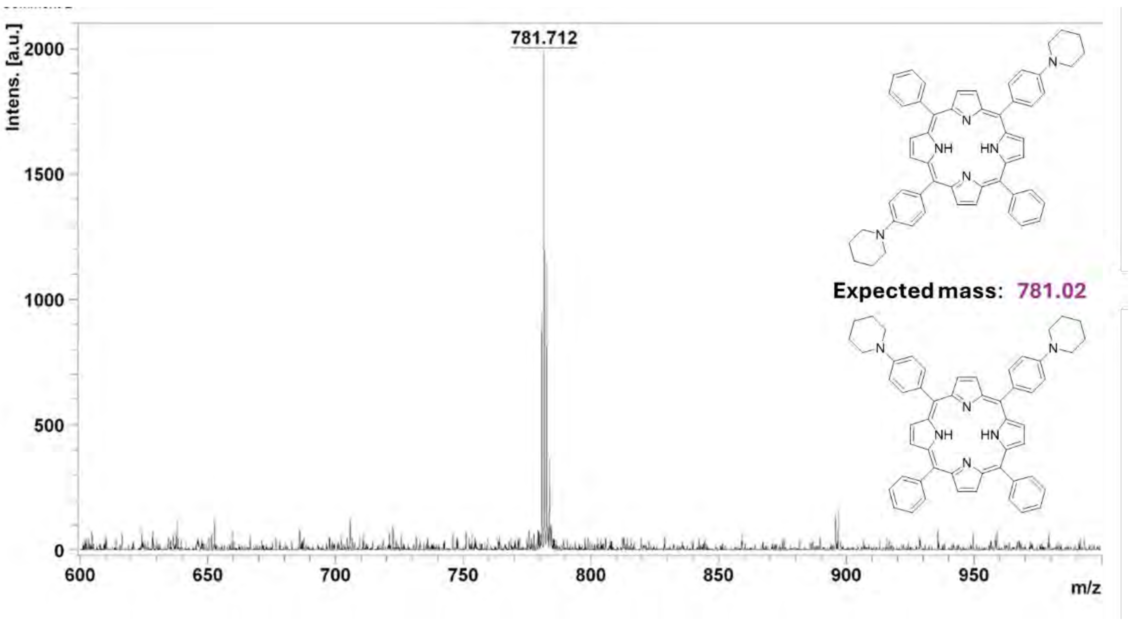

Figure 12. MALDI-TOF MS data for **2**.

The MALDI-TOF MS peak observed for **2** at 781.71 m/z corresponds to a [M+H]$^+$ peak (**Figure 12**).

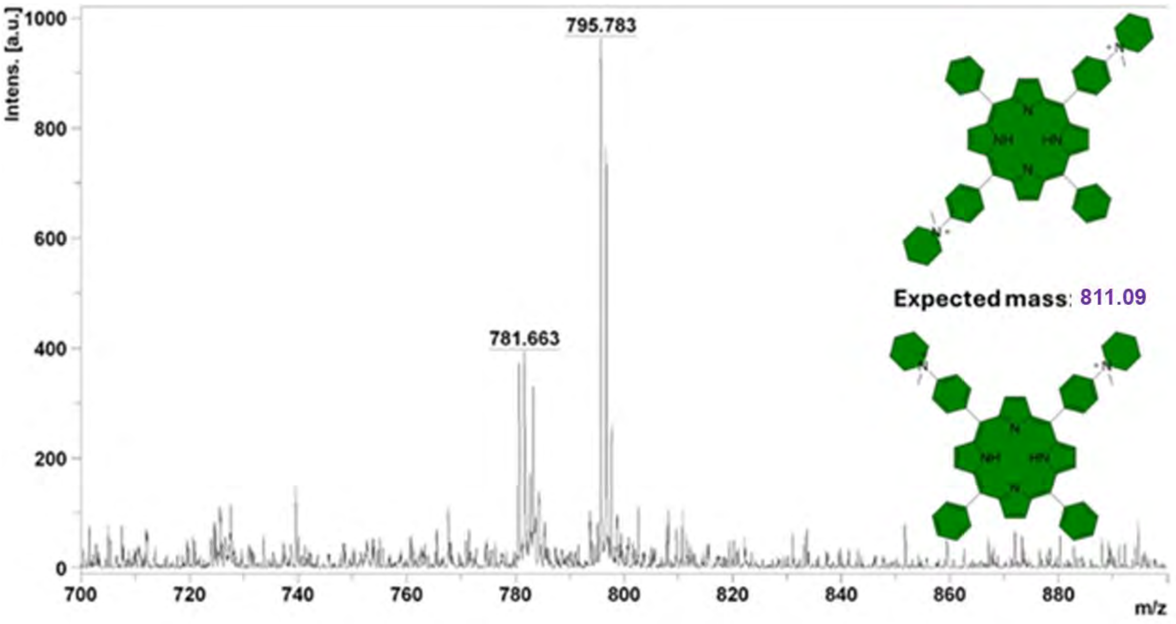

Figure 13. MALDI-TOF MS data for **2-Q**.

The MALDI-TOF MS peak observed for **2-Q** at 795.78 m/z corresponds to an $[M-CH_3]^+$ peak (**Figure 13**).

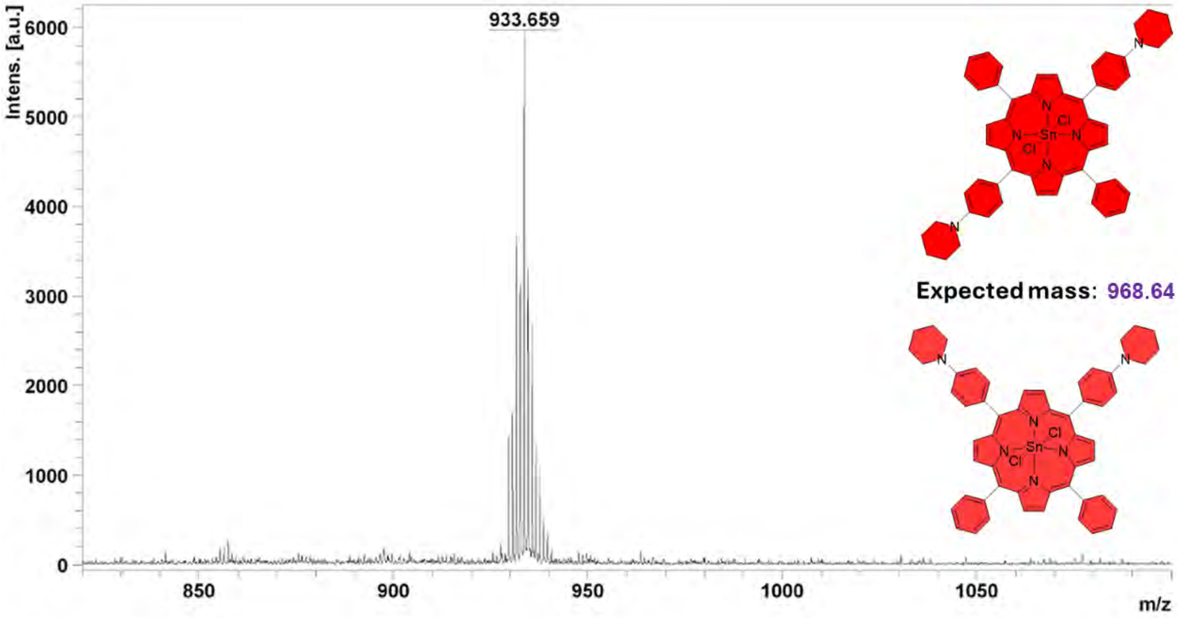

Figure 14. MALDI-TOF MS data for **2-Sn**.

The MALDI-TOF MS peak observed for **2-Sn** at 933.66 m/z corresponds to a $[M-Cl]^+$ peak (**Figure 14**).

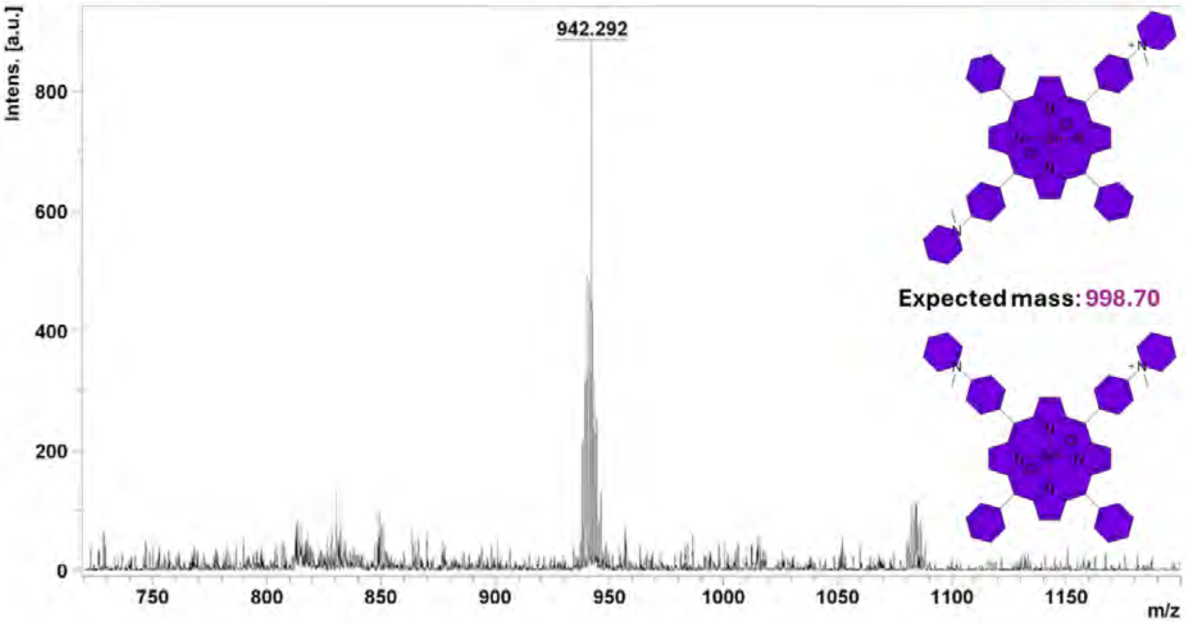

Figure 15. MALDI-TOF MS data for **2-Sn-Q**.

The MALDI-TOF MS peak observed for **2-Sn-Q** at 942.29 m/z is tentatively assigned to a $[M{-}C_4H_8]^+$ peak (**Figure 15**). It is unclear why fragmentation of a piperidinyl group would dominate for this quaternised dye species.

Series 3 MS data

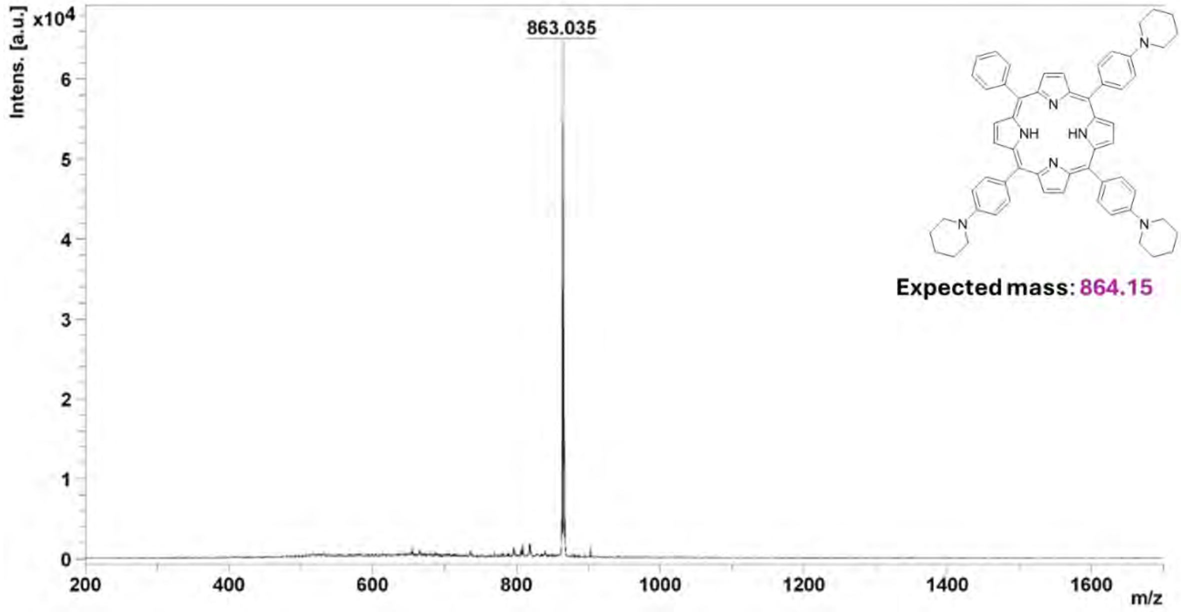

Figure 16. MALDI-TOF MS data for **3**.

The MALDI-TOF MS peak observed for **3** at 863.04 m/z corresponds to an $[M{-}2CH_3]^+$ peak (**Figure 16**).

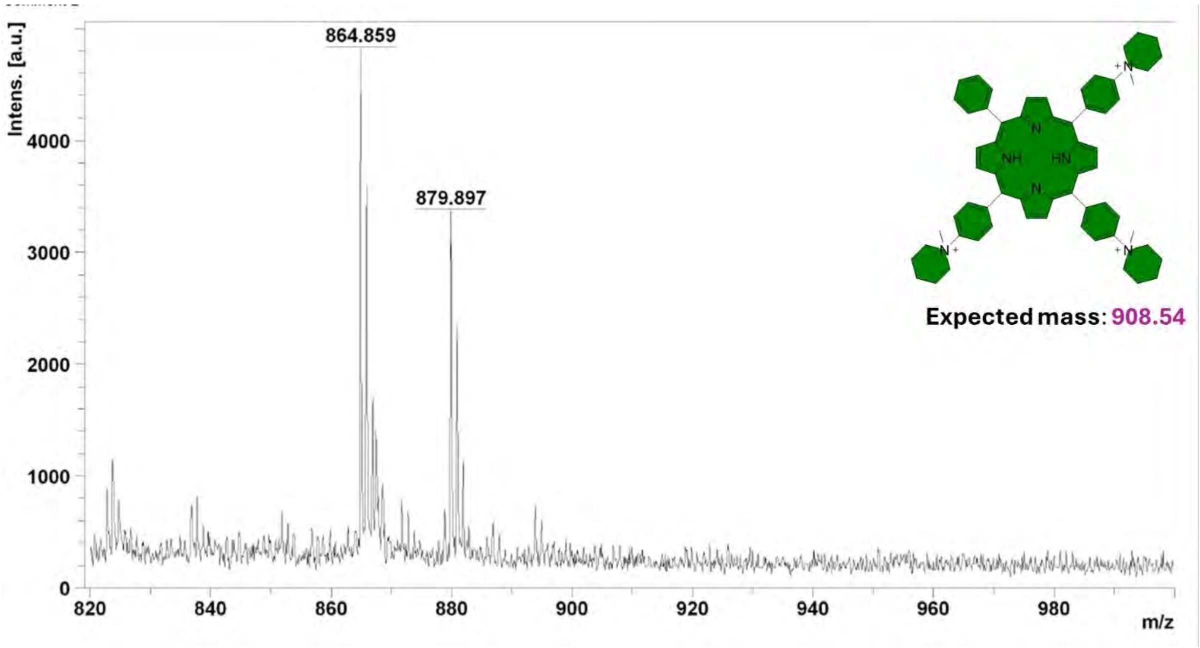

Figure 17. MALDI-TOF MS data for **3-Q**.

The MALDI-TOF MS peak observed for **3-Q** at 879.90 m/z corresponds to an $[M{-}2CH_3]^+$ peak (**Figure 17**).

Series 4 MS data

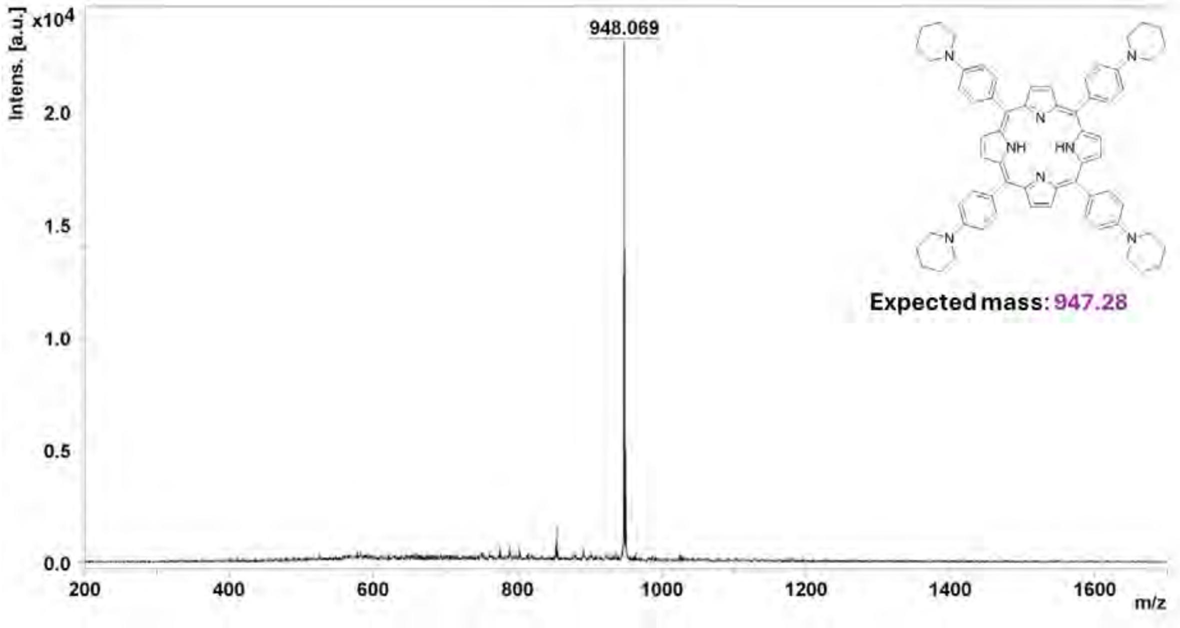

Figure 18. MALDI-TOF MS data for **4**.

The MALDI-TOF MS peak observed for **4** at 948.07 m/z corresponds to an $[M+H]^+$ peak (**Figure 18**).

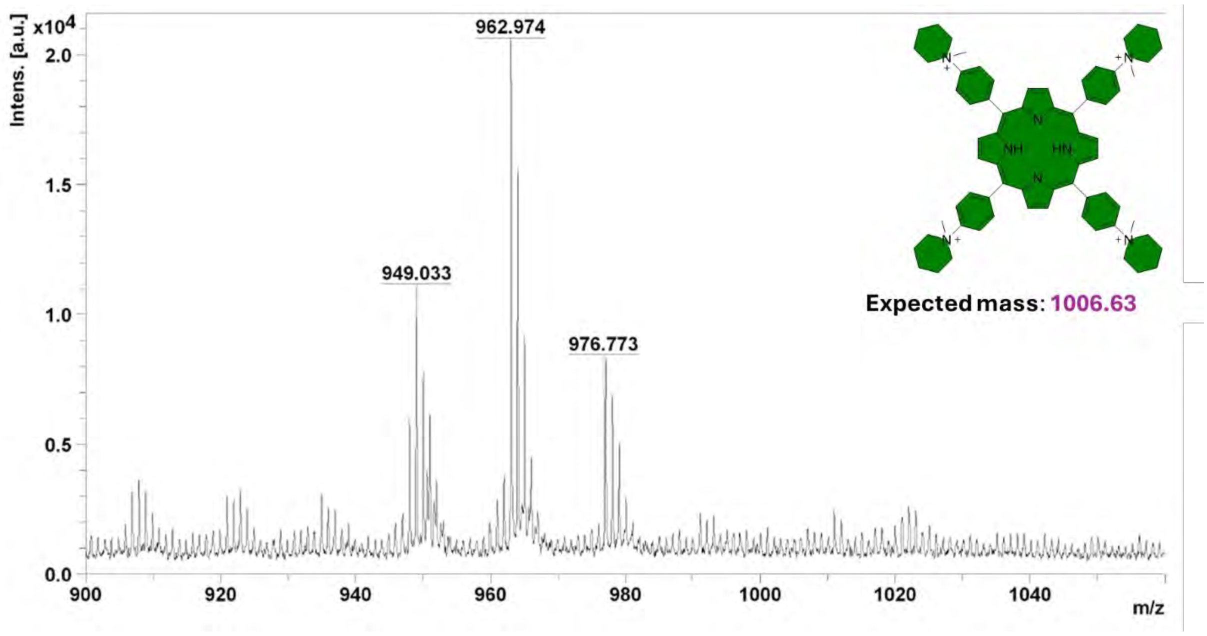

Figure 19. MALDI-TOF MS data for **4-Q**.

The MALDI-TOF MS peak observed for **4-Q** at 962.77 m/z corresponds to an $[M{-}2CH_3]^+$ peak (**Figure 19**).

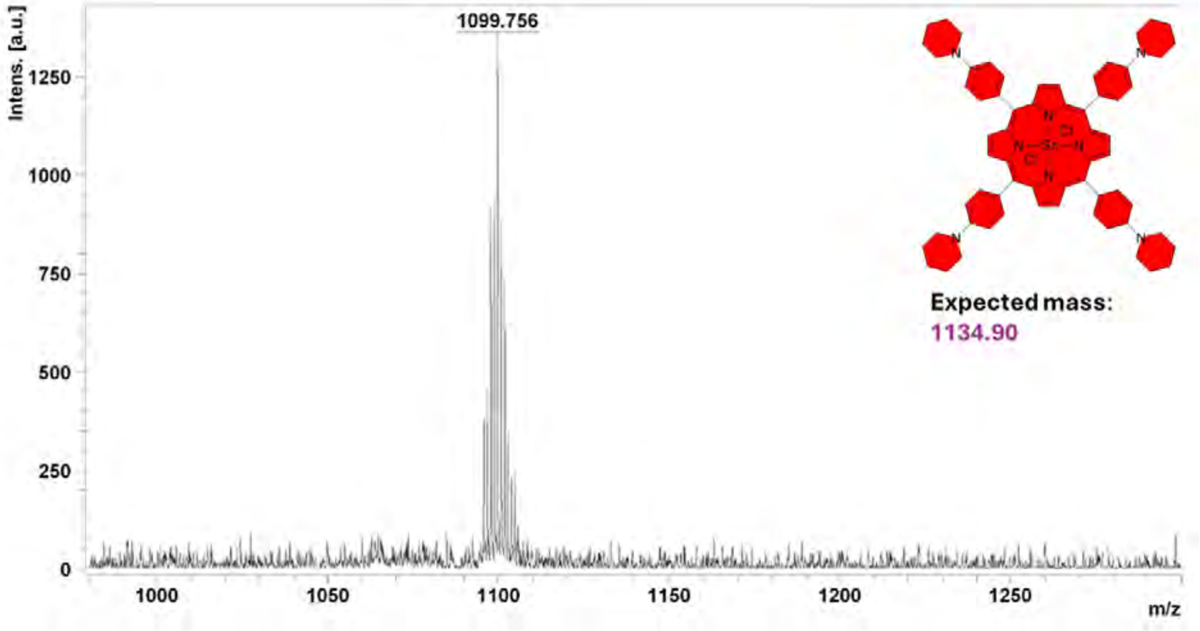

Figure 20. MALDI-TOF MS data for **4-Sn**.

The MALDI-TOF MS peak observed for **4-Sn** at 1099.76 m/z corresponds to an $[M{-}2Cl]^+$ peak (**Figure 20**).

3.2. ^{1}H NMR spectroscopy

^{1}H NMR spectra of all 16 target compounds were recorded in $CDCl_3$ and in each case the number of integrated protons was found to be consistent with the target structure. Spectra of **1**, **1-Sn** and **1-Q** (**Figures 21-23**) are described below as typical examples.

^{1}H NMR spectra of free base porphyrins

A distinctive peak that characterises free base porphyrins in the ^{1}H NMR spectra is the signal at *ca.* 3 ppm (see **Figure 21** for a typical example), which corresponds with the two inner nitrogens of the porphyrin central cavity. All ^{1}H NMR spectra for free base porphyrin (**1**, **2**, **3** and **4**) have broadly similar NMR spectra, but as the number of 4-(-1-piperidinyl) groups increases, the number of protons integrated in the aliphatic region steadily increases.

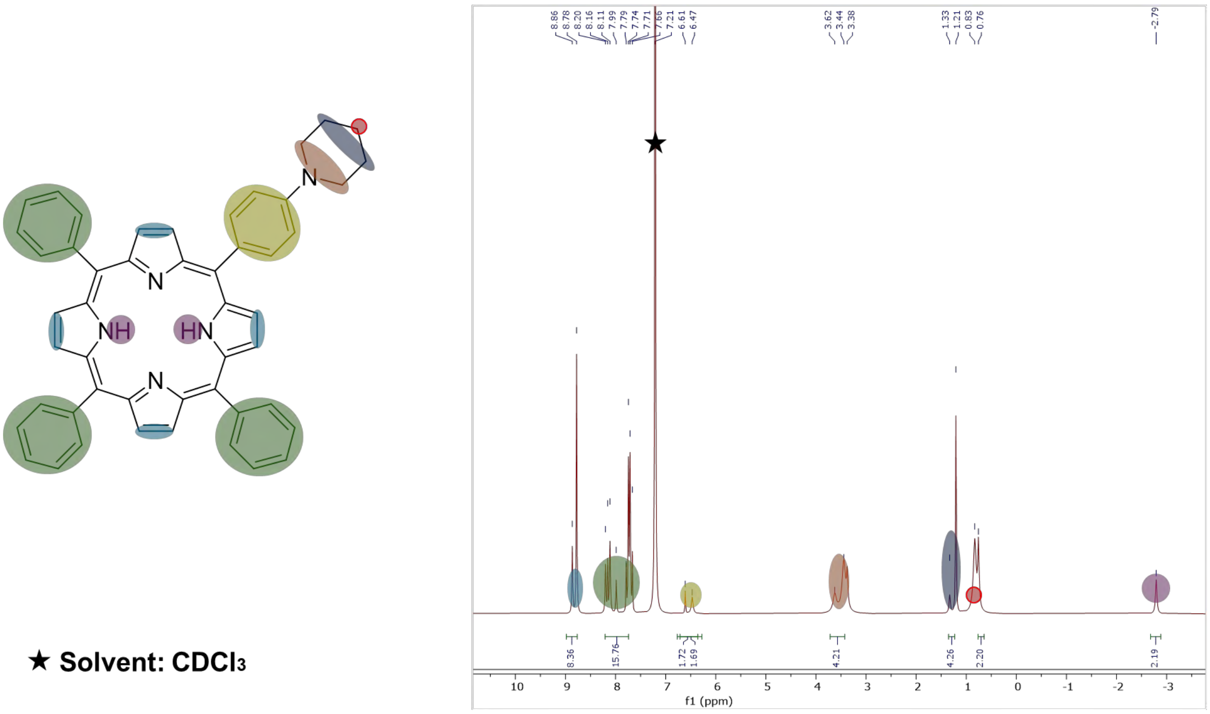

Figure 21. ^{1}H NMR spectrum of **1** in $CDCl_3$.

^{1}H NMR spectra of metalated porphyrins

The distinctive signal that appears at the negative region, mostly in the 2 to 3 ppm region, does not appear for metalated porphyrin complexes (see **Figure 22** for a typical example). This indicates that the Sn(IV) ion has been successfully inserted in the inner cavity of the porphyrin ligand.

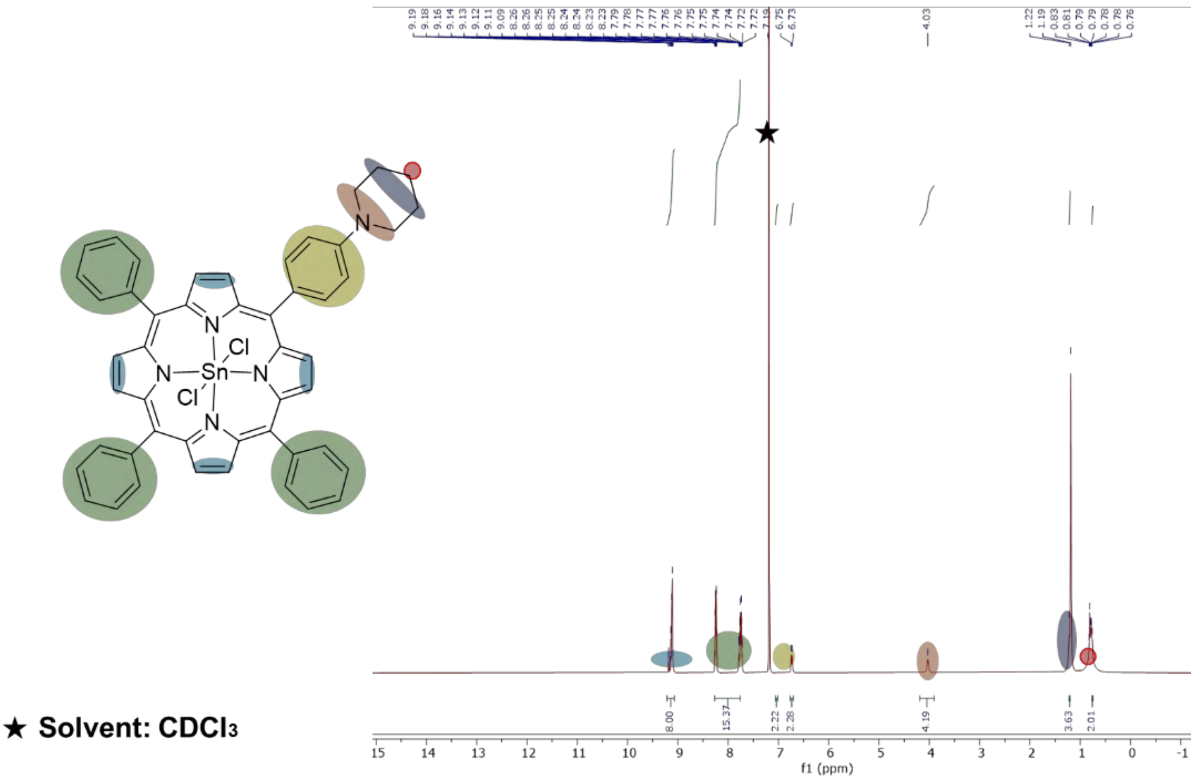

Figure 22. ^{1}H NMR spectrum of **1-Sn** in CDCl$_3$.

^{1}H NMR spectrum of quaternised porphyrin

In the ^{1}H NMR spectra of the quaternised porphyrins (see **Figure 22** for a typical example), a new peak between 2.5 and 3.5 ppm can be assigned to the methyl groups on the quaternized nitrogen atoms, but it was not possible to identify peaks for the inner NH protons of **1-4-Q**, possibly due to exchange with the solvent.

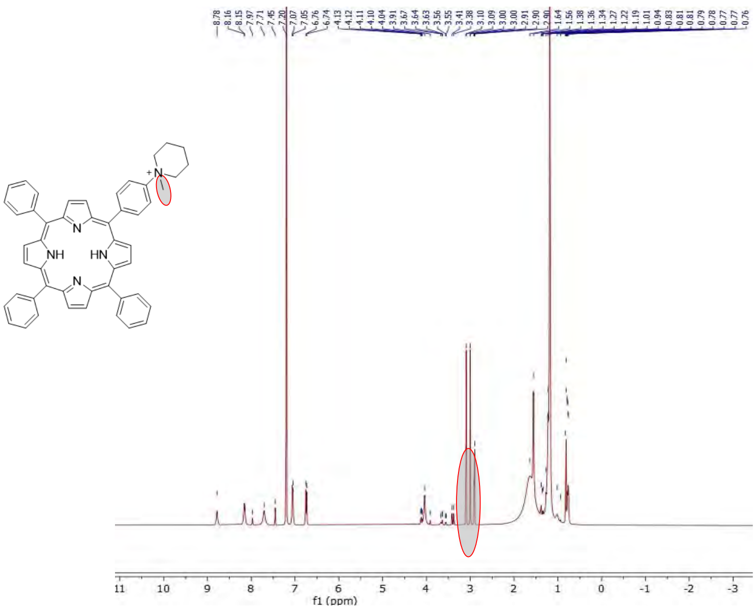

Figure 23. ^{1}H NMR spectrum of **1-Q** in $CDCl_3$.

3.3. Optical Spectroscopy

The first spectroscopic method used was UV-visible spectroscopy (**Figures 25-27**), which allows us to monitor the synthesis of porphyrinoids complexes. According to Gouterman's 4-orbital theory, a free base porphyrin has one B band and four Q bands, the pattern observed for **1-4**. When the free base complexes are metalated, the four Q bands collapse into two bands (**Figures 25-27**). The significant changes confirm the successful insertion of the Sn(IV) ion within the porphyrin core structure. The B and Q bands of the electronic absorption spectra of Series 4 compounds are broader in shape compared to Series 1, 2 and 3 compounds. This is almost certainly due to aggregation effects, since sonication of the solutions of all four series was required before the spectra could be measured in a reproducible manner with a standard 10 mm cuvette. In other regards, the spectra obtained for different series are very similar with the B band maxima of all sixteen dyes studied, only differing by 5 nm (**Table 1**), since the peripheral 4-(-1-piperidinyl) groups are not attached directly to the core of the porphyrin ligands, but to freely rotating phenyl rings.

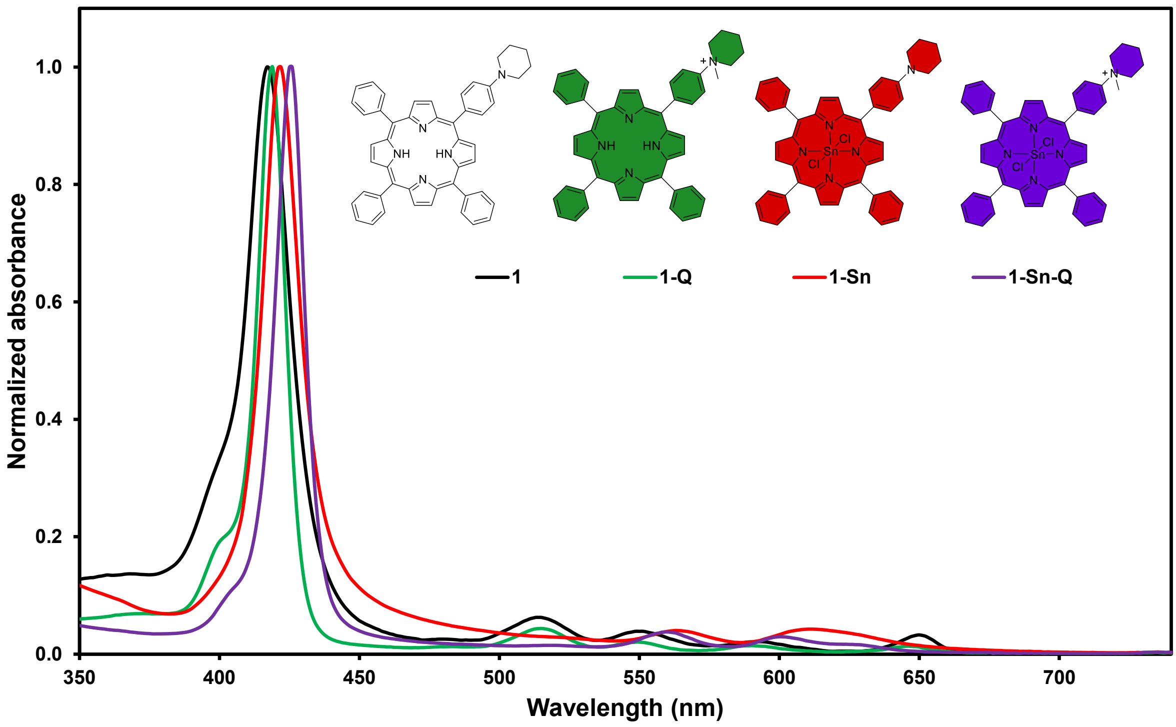

Figure 24. UV-visible absorption spectra of Series 1 porphyrin analogues in DMSO.

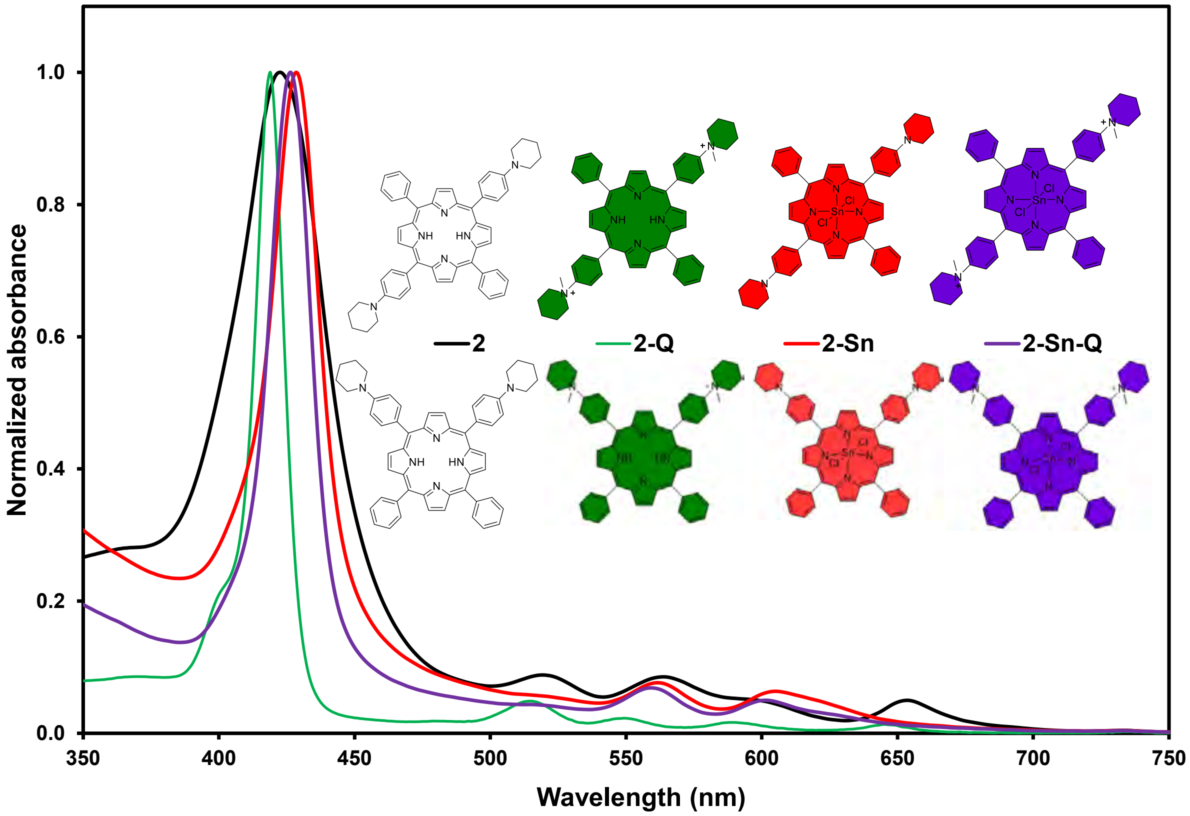

Figure 25. UV-visible absorption spectra of Series 2 porphyrin analogues in DMSO.

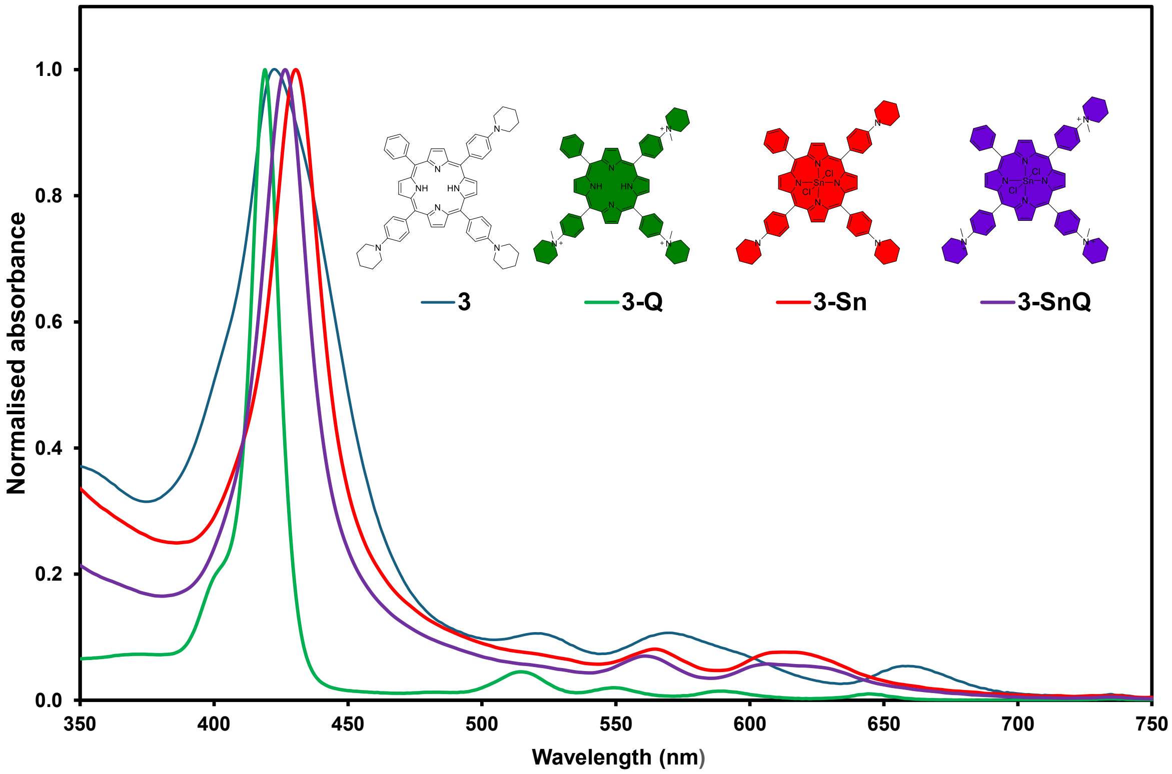

Figure 26. UV-visible absorption spectra of Series 3 porphyrin analogues in DMSO.

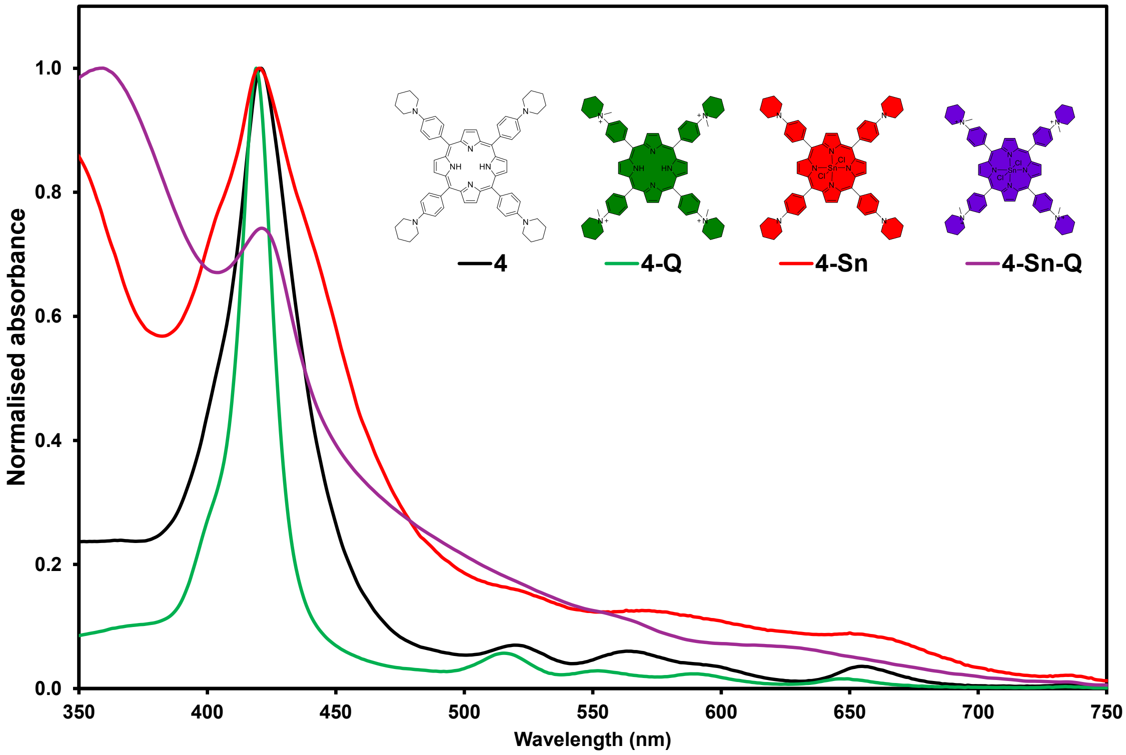

Figure 27. UV-visible absorption spectra of Series 4 porphyrin analogues in DMSO.

3.4. Photophysiochemical properties

The photophysiochemical properties of the porphyrin analogues, such as the singlet oxygen quantum yield (Φ_Δ), fluorescence quantum yield (Φ_F), triplet state lifetime (τ_T) and Stokes shift values were determined (**Table 1**), to predict the efficiency of the PS dye in biological applications, such as PDT and PACT. The addition of the 4-(-1-piperidinyl) group decreases the fluorescence quantum yield relative to the value of 0.0397 [67] reported previously for free base tetraphenylporphyrin due to the presence of nitrogen lone pairs and the scope for intramolecular charge transfer and/or greater conformational flexibility. Only very weak fluorescence signals were observed for **4** and the Sn(IV) complexes solutions, which could not be reliably quantified and verified through excitation spectra as being associated with the monomeric structures of these fluorophores. Relatively small Stokes shift values of *ca.* 120 cm^{-1} were observed for **1-3**. This confirms that the structures of these porphyrins remain relatively rigid upon photoexcitation.

Table 1. The photophysiochemical properties of all porphyrin analogues in Series 1-4.

	B band λ_{Abs} (nm)	**Q band λ_{Abs} (nm)**	**Q band λ_{em} (nm)**	**Stokes Shift (cm^{-1})**	**Φ_F**	**τ_T (µs)**	**Φ_Δ**	**Photo-stability (%)**
1	419	517, 554, 592, 651	655, 709	120	0.02	1.6	0.11	98
1-Q	419	515, 549, 590, 646	654, 717	210	0.04	5.5	0.03	95
1-Sn	422	563, 611	-	-	-	12.6	0.29	82
1-Sn-Q	425	557, 599	-	-	-	9.6	0.15	86
2	421	520, 565, 600, 654	659, 709	120	0.01	1.4	0.05	97
2-Q	419	515, 555, 590, 645	657, 719	280	0.03	3.9	0.05	98
2-Sn	424	562, 606	-	-	-	9.6	0.41	88
2-Sn-Q	422	561, 604	-	-	-	2.4	0.15	91

3	419	520, 561, 597, 654	659, 707	120	> 0.01	2.9	0.09	96
3-Q	419	514, 549, 590, 644	659, 721	350	> 0.01	4.5	0.06	85
3-Sn	422	566, 634	-	-	-	ND	0.35	ND
3-Sn-Q	424	563, 613	-	-	-	ND	0.20	ND
4	421	520, 563, 655	-	-	-	2.7	0.18	99
4-Q	419	526, 552, 588, 646	-	-	-	8.0	0.01	98
4-Sn	~420	~570, ~650	-	-	-	ND	~0.30	ND
4-Sn-Q	~420	~560, ~630	-	-	-	ND	~0.16	ND

ND – Could not be determined, probably due to issues related to aggregation effects.

The singlet quantum yield values of **1-4** and **1-4-Sn** (**Figure 1**) are lower than the values of 0.52 and 0.61 reported previously, respectively, for free base tetraphenylporphyrin (H_2TPP) and Sn(IV) tetraphenylporphyrin (SnTPP) in DMSO [75]. This is probably due to intramolecular charge transfer character introduced to the S_1 excited state by the 4-(-1-piperidinyl) groups and the greater conformational flexibility of the ligand structures of **1-4**. The singlet quantum yield values for all metalated complexes are higher than those of the corresponding free base and quaternised porphyrins. This is due to the heavy atom effect, which increases singlet quantum yield generation by increasing the rate of intersystem crossing to the triplet manifold due to spin-orbit coupling. This demonstrates that the heavy atom effect of the Sn(IV) ion had a significant influence on the photochemical properties. **1-Sn** and **2-Sn** have the longest triplet lifetimes (**Table 1**).

Conclusions

The novel porphyrin analogues were characterized by MALDI-TOF MS, UV-visible and ^{1}H NMR spectroscopy. As anticipated, the singlet oxygen quantum yield values for **1-4-Sn** are significantly higher than those of **1-4** due to the heavy atom effect, which increases the singlet oxygen quantum yield generation, so the metal complexes are anticipated to be more suitable for use in singlet oxygen photosensitizer applications such as PDT and PACT.

Chapter 4: PACT Studies

Antimicrobial Activity

The main purpose of the PACT studies was to evaluate the effect of the number of charges porphyrin analogue has on their PACT activity. The activities of **1**, **2**, **3** and **4** were also compared to those of the **1-Sn-Q**, **2-Sn-Q**, **3-Sn-Q** and **4-Sn-Q** quaternised porphyrin analogues to explore in proof of principle terms whether metalation and quaternisation enhances the PACT activity.

During the initial preparation procedures prior to the *in vitro* PACT studies, the dilution factor for the bacteria solution and optimal porphyrin concentration were determined. A bacterial solution with a dilution factor of 10^{-4} was used for these studies. Porphyrin analogues **1**, **2**, **3** and **4** were used to determine the optimal concentration (2.5−80 µM) irradiated for 90 min using a 595 nm LED (Thorlabs 595L3, dose: 13.0 mJ.cm^{-2} at the well-plate). The optimal concentration selected for the *in vitro* PACT time dependent was 25 µM for all compounds. This is the concentration at which an average amount of bacteria is inactivated (**Figure 28**. a). Minimal PACT activity was observed for the compounds kept in the dark for 90 min (**Figure 28b**). This clearly demonstrates that porphyrin analogues are only active when irradiated with light, which is a favourable characteristic of porphyrin analogues because they should only be active when irradiated with light.

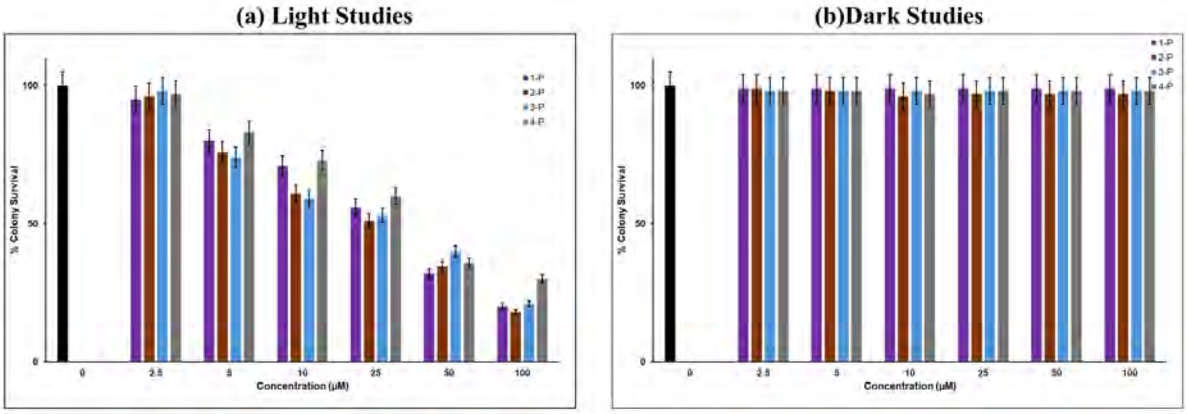

Figure 28. (a) The effect of porphyrin **1**, **2**, **3** and **4** at different concentrations against *S. aureus* irradiated for 90 min. (b) The effect of porphyrin **1**, **2**, **3** and **4** at different concentrations against *S. aureus* when kept in the dark for 90 min. The error bars denote the standard deviation of independent triplicate measurements.

The Resazurin assay method [76] was used to determine the antimicrobial activity of the compounds. When the resazurin dye interacts with bacteria, it turns pink in a manner that quantifies bacteria survival. When there is low bacteria survival, it stays blue (**Figure 29**).

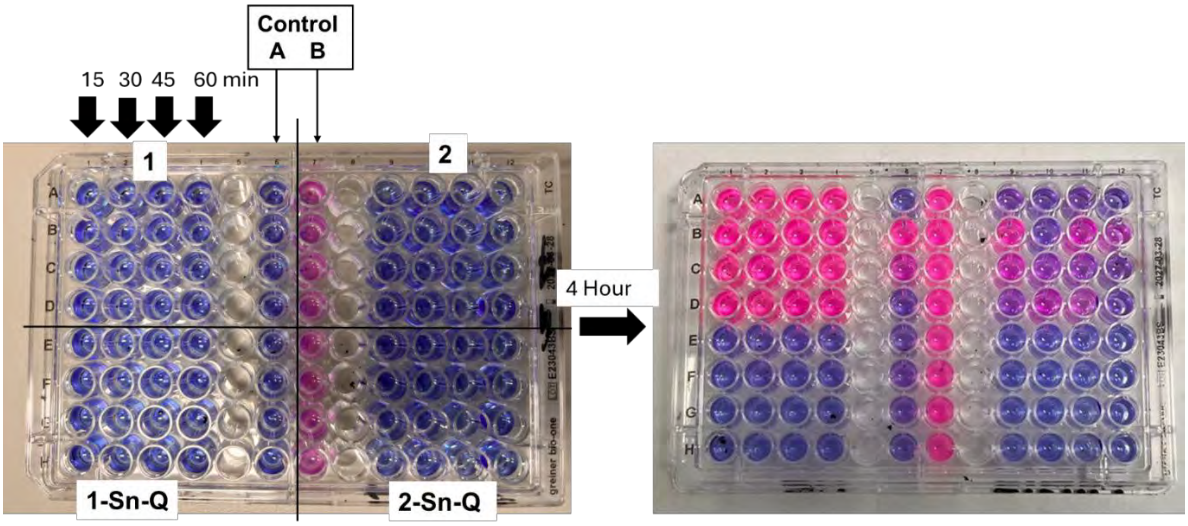

Figure 29. Resazurin assay results against *S. aureus*.

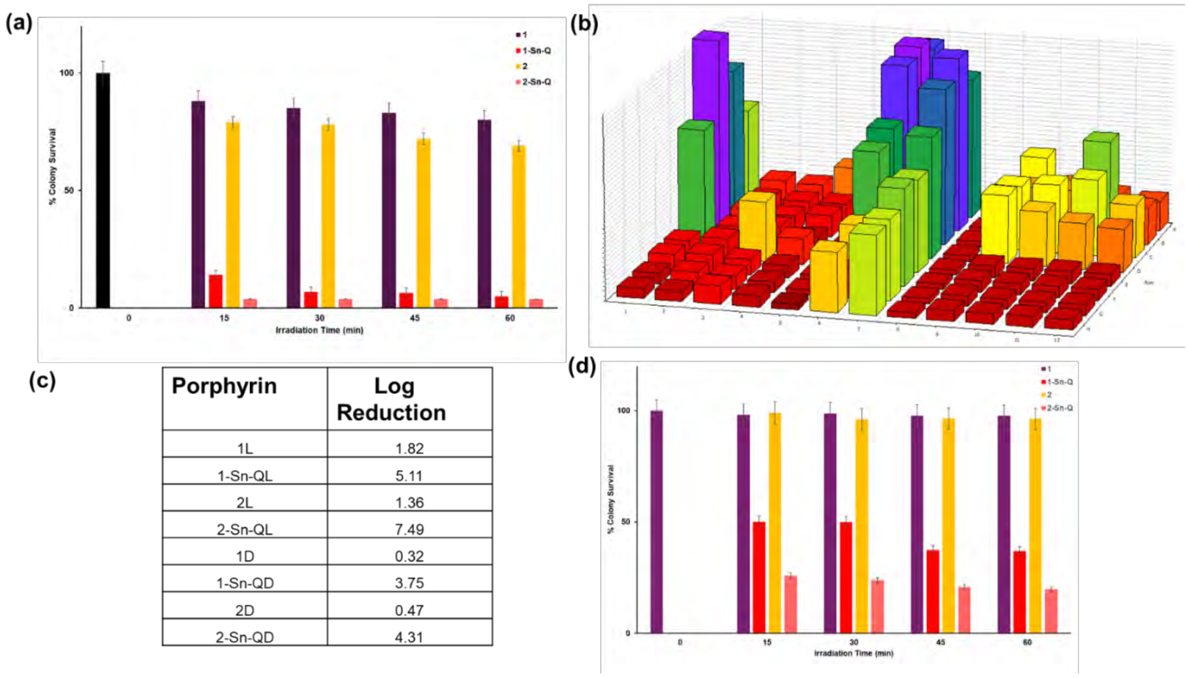

Porphyrin	Log Reduction
1L	1.82
1-Sn-QL	5.11
2L	1.36
2-Sn-QL	7.49
1D	0.32
1-Sn-QD	3.75
2D	0.47
2-Sn-QD	4.31

Figure 30. PACT results for **1**, **2**, **1-Sn-Q** and **2-Sn-Q**. (a) PACT light studies. (b) 96 microplate PACT results. (c) Log_{10} reduction values. (d) PACT dark studies. The error bars denote the standard deviation of independent triplicate measurements.

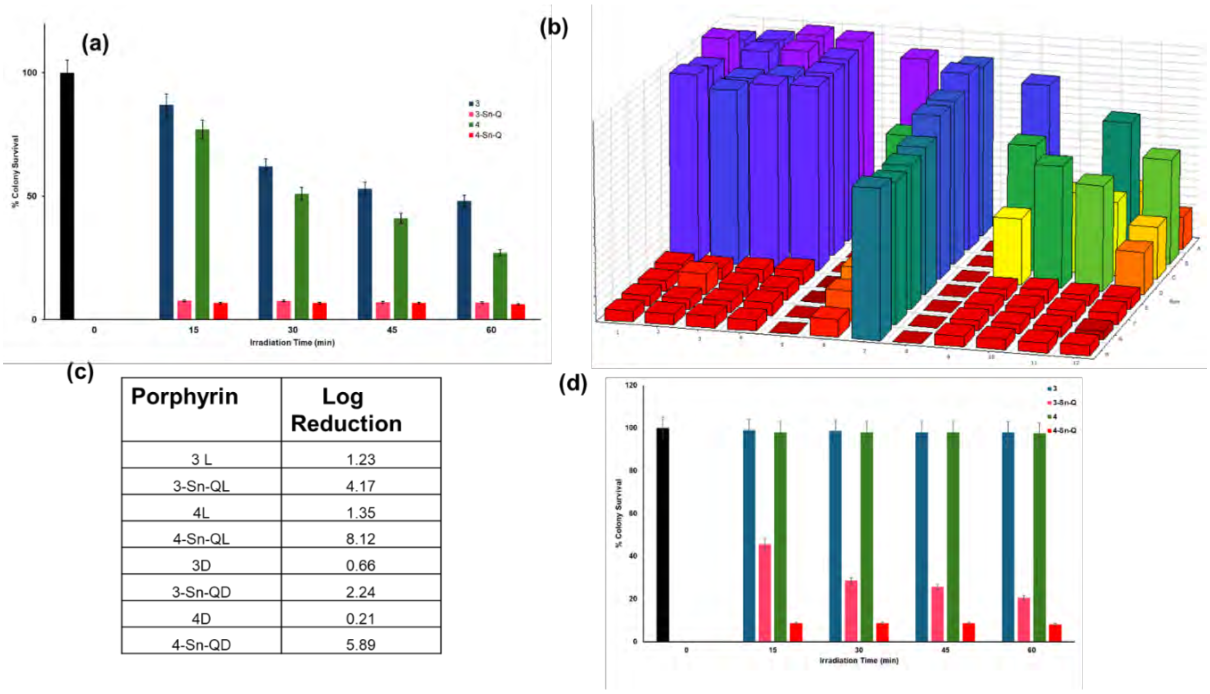

Porphyrin	Log Reduction
3 L	1.23
3-Sn-QL	4.17
4L	1.35
4-Sn-QL	8.12
3D	0.66
3-Sn-QD	2.24
4D	0.21
4-Sn-QD	5.89

Figure 31. PACT results for **3**, **4**, **3-Sn-Q** and **4-Sn-Q**. (a) PACT light studies. (b) 96 microplate PACT results. (c) Log_{10} reduction values. (d) PACT dark studies. The error bars the standard deviation of independent triplicate measurements.

Concluding Remarks

Photosensitisers and other drugs with a Log_{10} reduction > 3 are considered antimicrobial agents by the United States FDA. Uncharged porphyrin analogues exhibited low antimicrobial activity compared to charged porphyrin analogues, which can be observed due to high cell survival percentages and Log_{10} reduction values below 3. In contrast, **1-Sn-Q**, **2-Sn-Q**, **3-Sn-Q** and **4-Sn-Q**all exhibited favourable PACT activity properties. Interestingly, the quaternised Sn(IV) porphyrin analogues exhibited relatively high antimicrobial activity in the dark as well as during the PACT activity studies. The reasons for this clearly merit further in-depth study but were beyond the scope of this MSc study.

Chapter 5: PDT Studies

Photodynamic Activity

The *in vitro* PDT studies were conducted to evaluate the PDT activities of the free base porphyrins (**1**, **2**, **3** and **4**) compared to their quaternised analogues (**1-Q**, **2-Q**, **3-Q** and **4-Q**), their metalated complexes (**1-Sn**, 2-**Sn**, **3-Sn** and **4-Sn**) and metalated quaternised analogues (**1-Sn-Q**, **2-Sn-Q**, **3-Sn-Q** and **4-Sn-Q**). The PDT activity of the porphyrin analogues was tested against MDA breast cancer cells, which are more aggressive and difficult to treat compared to other breast cancer cell lines, such as MCF-7 and Hela cells. The Resazurin assay was used to quantify the cytotoxicity of the porphyrin analogue at different concentrations ranging from 2.5−100 μM, irradiated for 1 h with a 595 nm LED (Thorlabs 595L3, dose: 9.0 mJ.cm^{-2} at the well-plate). GraphPad software was used to calculate IC$_{50}$ values for the dark toxicity and PDT activity studies (**Figures 32-35** and **Table 2**). IC$_{50}$ values provide a measure of the half-maximal inhibitory concentration of the porphyrinoids; the lower the IC$_{50}$ value, the more potent the drug. Phototoxicity Index (PI) values were calculated from the ratio of the dark toxicity and PDT activity IC$_{50}$ values.

All porphyrin analogues exhibited low, minimal dark cytotoxicity. This is a favourable characteristic for porphyrinoids. The photosensitiser should be cytotoxic only when irradiated with light of appropriate wavelengths. As anticipated, there is a clear relationship between concentration and the observed PDT activity of the porphyrin analogues. As the concentration increases, the PDT activity also increases. The higher the PDT activity, the lower the IC$_{50}$ value. The rationale behind modifying the porphyrin structures was to increase the cytotoxicity through higher singlet oxygen quantum yield generation. The trends observed with **3-Sn** and **3-Sn-Q** demonstrate that metalation of the porphyrin analogue increases the observed cytotoxicity (**Figure 34**) due to higher singlet oxygen quantum yields.

Although modifying the structures of compounds can increase their cytotoxicity due to changes in their singlet oxygen quantum yield, the effect on lipophilicity should also be considered, which is the measure (Log P) of how well a compound diffuses between the aqueous and organic layers, which affects the porphyrin uptake into the cancerous cell. Negative Log_{10} P values indicate that the compounds are more hydrophilic, while a Log_{10} P value of 0 indicates that the compound has equally hydrophilic and lipophilic characteristics. According to Lipinski's rules, Log_{10} P values between 1−5 are considered favourable for orally administered drugs. Several of the quaternised porphyrin analogues (**2-Q**, **2-Sn-Q**, **3-Q** and **4-Sn-Q**) have negative Log_{10} P values, since they are more hydrophilic. The aqueous layer was visibly coloured after the shake flask experiment layers had settled in contrast with what happened with the non-quaternised dyes. The PDT activity IC_{50} values of **3-Sn** and **3-Sn-Q** are >1.79 and >1.09, respectively. This indicates that **3-Sn** and **3-Sn-Q** are photodynamically active and more potent than the other porphyrin analogues. In contrast, the porphyrin analogues within Series 4 exhibited low PDT activity with IC_{50} values > 35, likely due to aggregation effects. No clear trend is observed with the number of

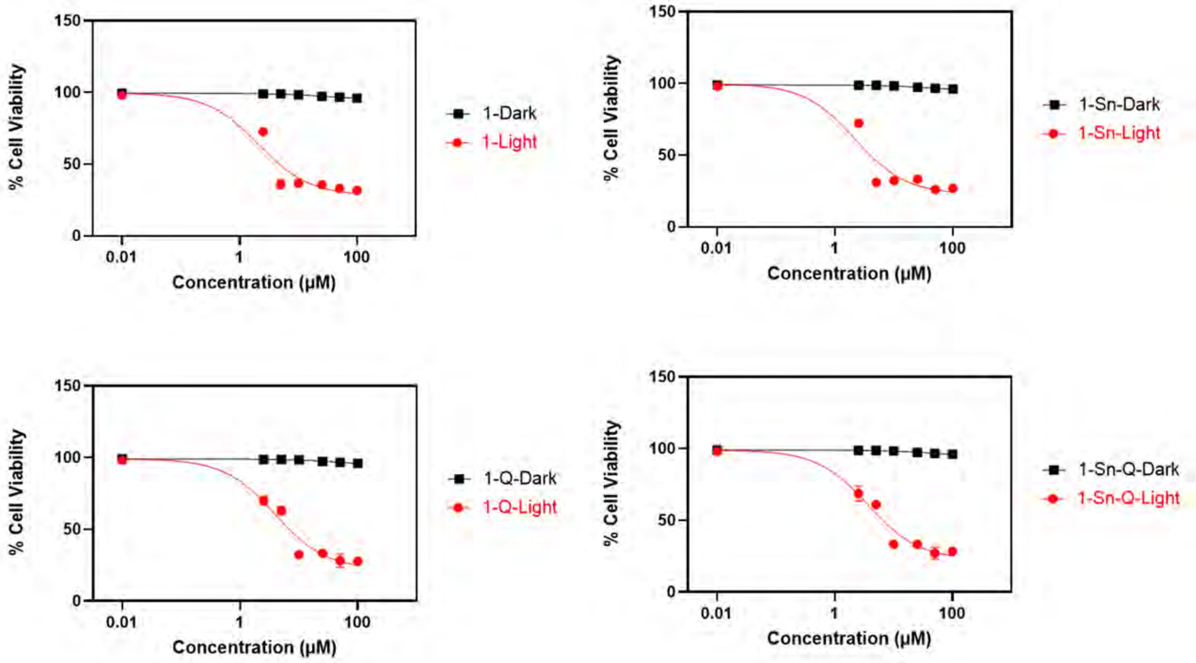

Figure 32. Series 1 IC_{50} determination curves showing the cytotoxicity of porphyrinoids against MDA breast cancer cell line, light and dark studies. The error bars the standard deviation of independent triplicate measurements.

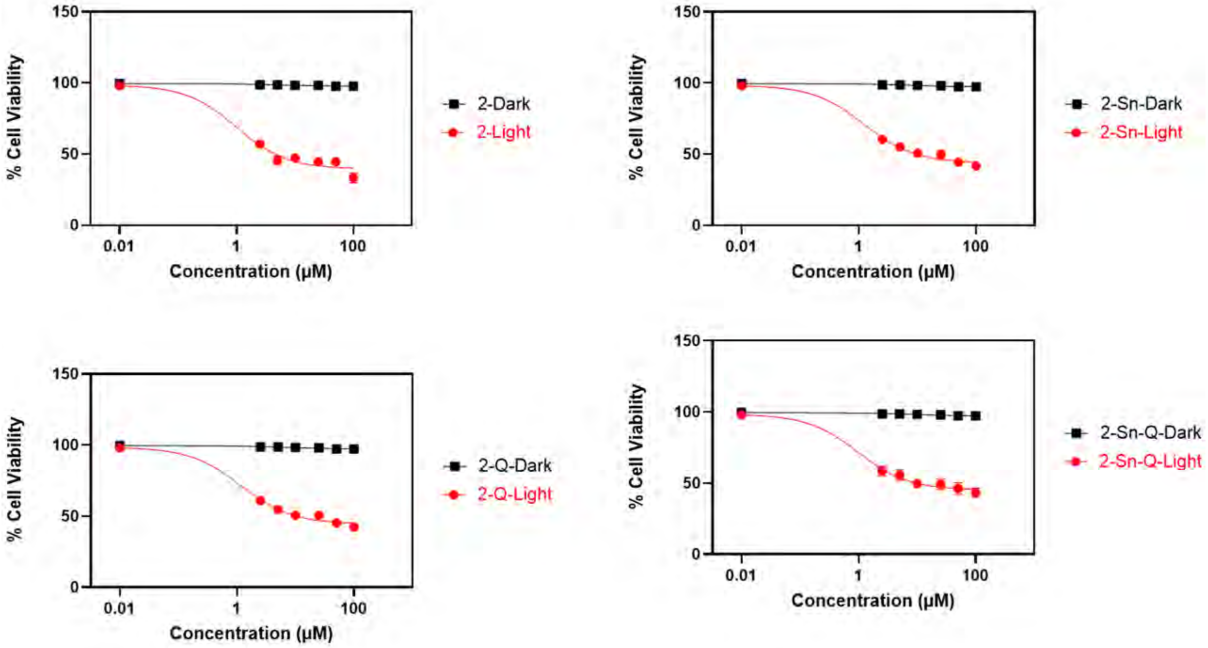

Figure 33. Series 2 IC_{50} value determination curves showing the cytotoxicity of porphyrinoids against MDA breast cancer cell line, light and dark studies. The error bars the standard deviation of independent triplicate measurements.

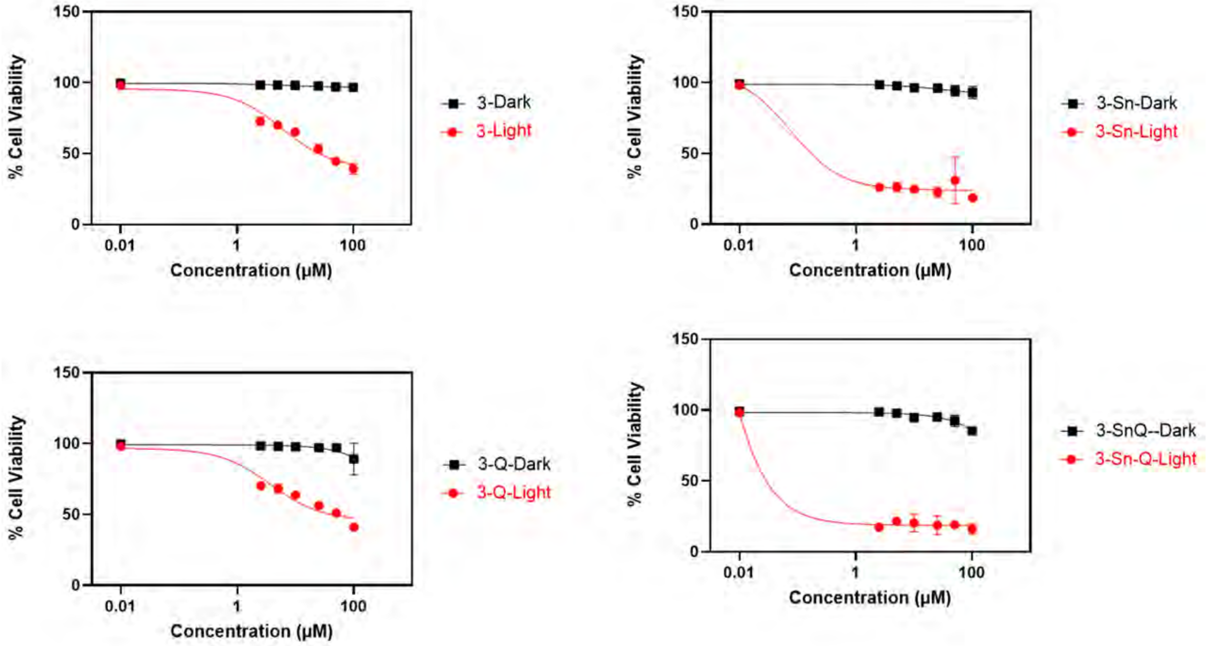

Figure 34. Series 3 IC_{50} value determination curves showing the cytotoxicity of porphyrinoids against MDA breast cancer cell line, light and dark studies. The error bars the standard deviation of independent triplicate measurements.

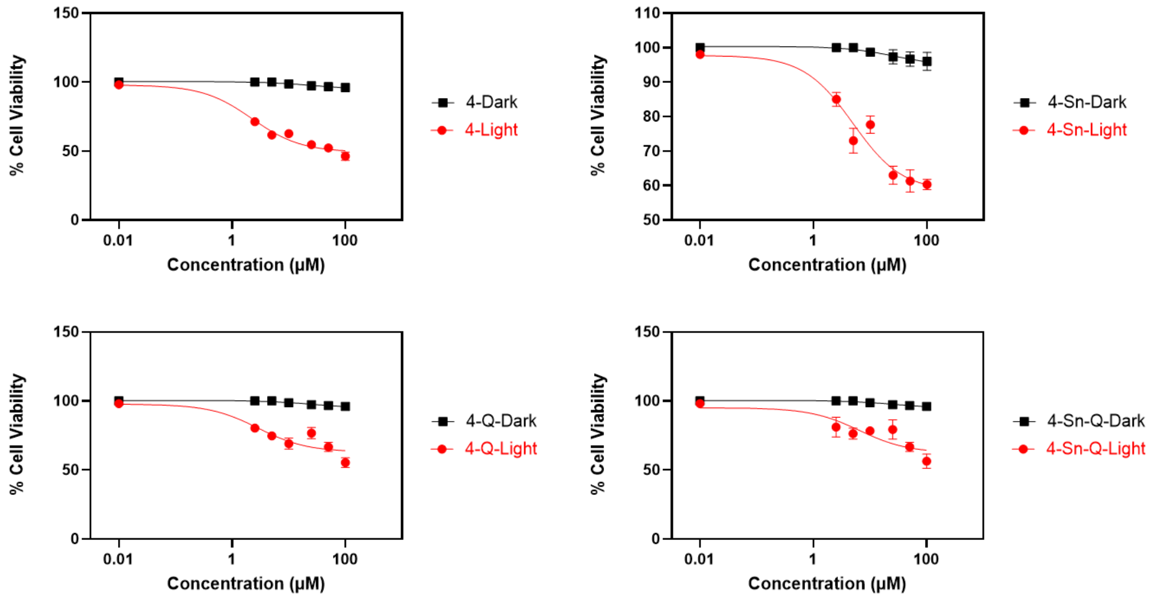

Figure 35. Series 4 IC$_{50}$ value determination curves showing the cytotoxicity of porphyrinoids against MDA breast cancer cell line, light and dark studies. The error bars the standard deviation of independent triplicate measurements.

Table 2. IC$_{50}$, PI and Log P values for the dark toxicity and PDT activity studies.

	IC$_{50}$ (μM)		PI	Log P
	Light	**Dark**		
1	7.15	> 100	> 14.0	0.65
1-Q	8.99	> 100	> 11.1	0.42
1-Sn	5.61	> 100	> 17.8	0.86
1-Sn-Q	8.71	> 100	> 11.5	0.29
2	11.1	> 100	> 8.98	0.34
2-Q	18.7	> 100	> 5.34	-0.90
2-Sn	17.8	> 100	> 5.61	0.79
2-Sn-Q	20.4	> 100	> 4.89	-0.75
3	30.6	> 100	> 3.26	0.76
3-Q	35.0	> 100	> 2.85	-0.52
3-Sn	1.79	> 100	> 55.9	0.75
3-Sn-Q	1.09	> 100	> 91.7	-0.38
4	35.3	> 100	> 2.83	-
4-Q	90.9	> 100	> 1.10	-
4-Sn	79.0	> 100	> 1.27	0.12
4-Sn-Q	83.0	> 100	> 1.20	-0.54

Concluding Remarks

Structural modification of the tetraphenylporphyrin ligand by introducing 4-piperidinylphenyl groups introduced at the *meso*-positions modifies the observed PDT activity with substitution with one and three 4-piperidinylphenyl groups, resulting in more favourable than was observed with two and four 4-piperidinylphenyl groups. Metal insertion in all porphyrin series resulted in lower IC_{50} values for the metal complexes than for the free base porphyrins. All the porphyrin analogues studied exhibited minimal cytotoxicity against MDA cancer cells in the dark toxicity studies with IC_{50} >100 and showed observable PDT activity when irradiated with light. This makes several of the porphyrin analogues favourable photosensitiser dyes for PDT. **3-Q** and **3-Sn-Q** had the lowest IC_{50} values, making them more PDT active than the other porphyrin analogues. Since a different cell line was used, it is not possible to directly compare the IC_{50} values with those obtained in other recent PDT activity studies at Rhodes University against MCF-7 breast cancer cells [49].

Chapter 6: Molecular docking

Molecular Docking

Molecular docking studies were conducted against the HSA plasma protein, a protein available in excess in human plasma. The binding affinity of the porphyrin analogues towards the HSA protein was determined using Autodock Vina software. The pharmacokinetics of the porphyrin analogue properties (i.e. ADMET and Lipinski's rule of five) properties were determined using ADMETlab 2.0 software to evaluate the likeliness of the drugs being approved by the United States Food and Drug Administration as photosensitiser in PDT.

Binding Affinity

Binding affinity energy is the value that determines how strong or weak the interaction between the porphyrin analogues and the protein HSA is (**Table 3**). The more negative the binding affinity value, the more compound will be available to spontaneously bind to the HSA plasma protein (**Table 4**). Series 1 porphyrin analogues (**1**, **1-Q**, **1-Sn** and **1-Sn-Q**) have the lowest binding affinity energy compared to other porphyrin analogues within other series. This indicates that as additional 4-(-1-piperidinyl) groups are added to the tetraphenylporphyrin core structure, the ability of the compound to interact with the HSA plasma protein decreases.

Within Series 1, **1-Q** has the lowest binding affinity energy, indicating a higher probability of the compound interacting with the HSA plasma protein than all of the other porphyrin analogues. Having a higher binding affinity energy not only indicates that there is a lower chance of the porphyrin analogues interacting with plasma protein, it also provides a strong indication that the compound does not interact with any biological molecules or interfere with their biological function. The following order represents the trend in the probability that the porphyrin analogues would interact spontaneously with the plasma protein: Series 1 > Series 2 > Series 3 > Series 4. Within each series, the quaternised compounds have higher chances (**Table 4**). Although metal insertion increases the singlet quantum yield generation, the complexes exhibit unfavourable forbidden interactions with the HSA plasma protein (**Figure 36**); hence, they have high binding affinity values.

Table 3. A clustering histogram showing the binding energy affinity obtained from Autodock Vina after docking the porphyrin analogues and HSA plasma protein.

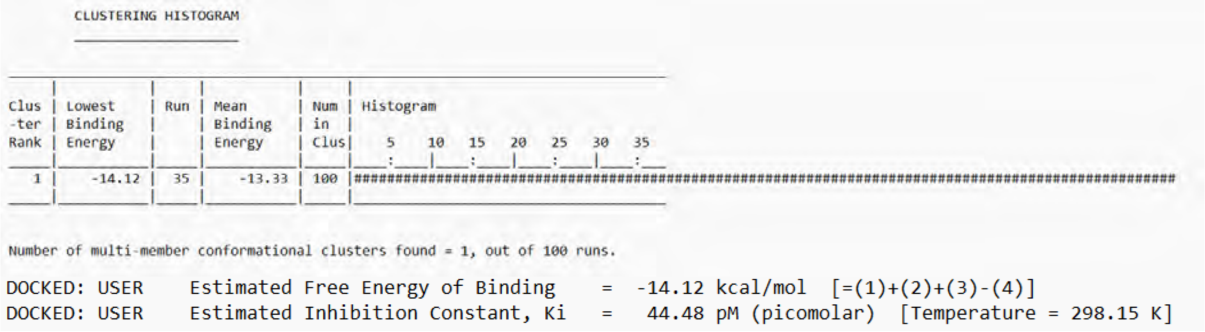

```
        CLUSTERING HISTOGRAM
        ____________________

________________________________________________________________________________
     |           |     |           |     |
Clus | Lowest    | Run | Mean      | Num | Histogram
-ter | Binding   |     | Binding   | in  |
Rank | Energy    |     | Energy    | Clus|    5    10   15   20   25   30   35
_____|___________|_____|___________|_____|____:____|____:____|____:____|____:___
   1 |    -14.12 |  35 |    -13.33 | 100 |####################################################################################################
_____|___________|_____|___________|_____|______________________________________


Number of multi-member conformational clusters found = 1, out of 100 runs.

DOCKED: USER    Estimated Free Energy of Binding    =  -14.12 kcal/mol  [=(1)+(2)+(3)-(4)]
DOCKED: USER    Estimated Inhibition Constant, Ki   =   44.48 pM (picomolar)  [Temperature = 298.15 K]
```

Table 4. The binding affinity between the HSA plasma protein and porphyrin analogues.

No.	Compound	Binding affinity (kcal/mol)
1	1	-14.12
2	1-Q	-13.10
3	1-Sn	+6.25
4	1-Sn-Q	+5.44
5	2	+0.12
6	2-Q	+4.63
7	2-Sn	+50.55
8	2-Sn-Q	+51.20
9	3	+46.51
10	3-Q	+64.03
11	3-Sn	+77.26
12	3-Sn-Q	+118.00
13	4	+13953.12
14	4-Q	+12237.78
15	4-Sn	+1171.55
16	4-Sn-Q	+20480.43

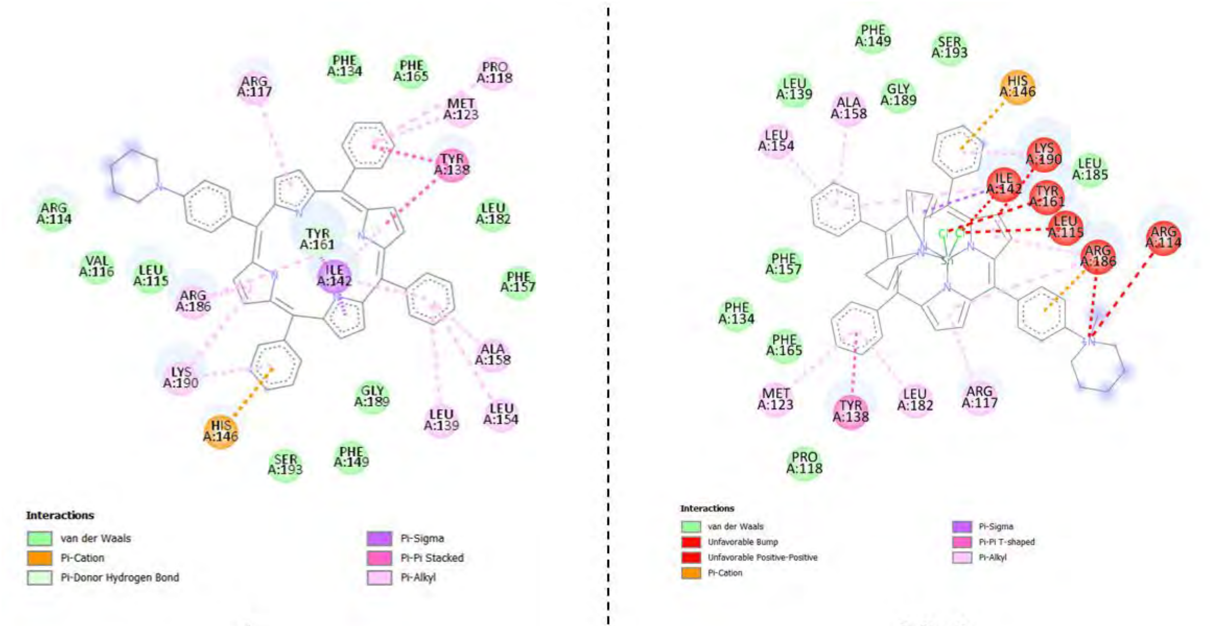

1　　**1-Sn-Q**

Figure 36. The interaction between the HSA plasma protein and porphyrin analogues.

Lipinski Rule of Five

Lipinski's rule [77] states that an orally active drug has no more than one violation of the following criteria:

- No more than 5 hydrogen bond donors (the total number of nitrogen–hydrogen and oxygen–hydrogen bonds).
- No more than 10 hydrogen bond acceptors (all nitrogen or oxygen atoms)
- A molecular mass of less than 500 Daltons.
- A calculated octanol-water partition coefficient (Log P) that does not exceed 5.

Although all porphyrin analogues have violated the Lipinski rule of five (**Table 5**), this does not disqualify them from being used in PDT as the photosensitiser drug. Photofrin® is an FDA-approved porphyrin photosensitiser used in PDT with a mass above 500 daltons, and it is administered as an intranvenous (IV) injection [77]. Therefore, porphyrin analogues cannot be approved as orally active drugs but can potentially be administered through IV injection.

Table 5. Lipinski rule of 5 parameters predicted using Auto-dock Vina.

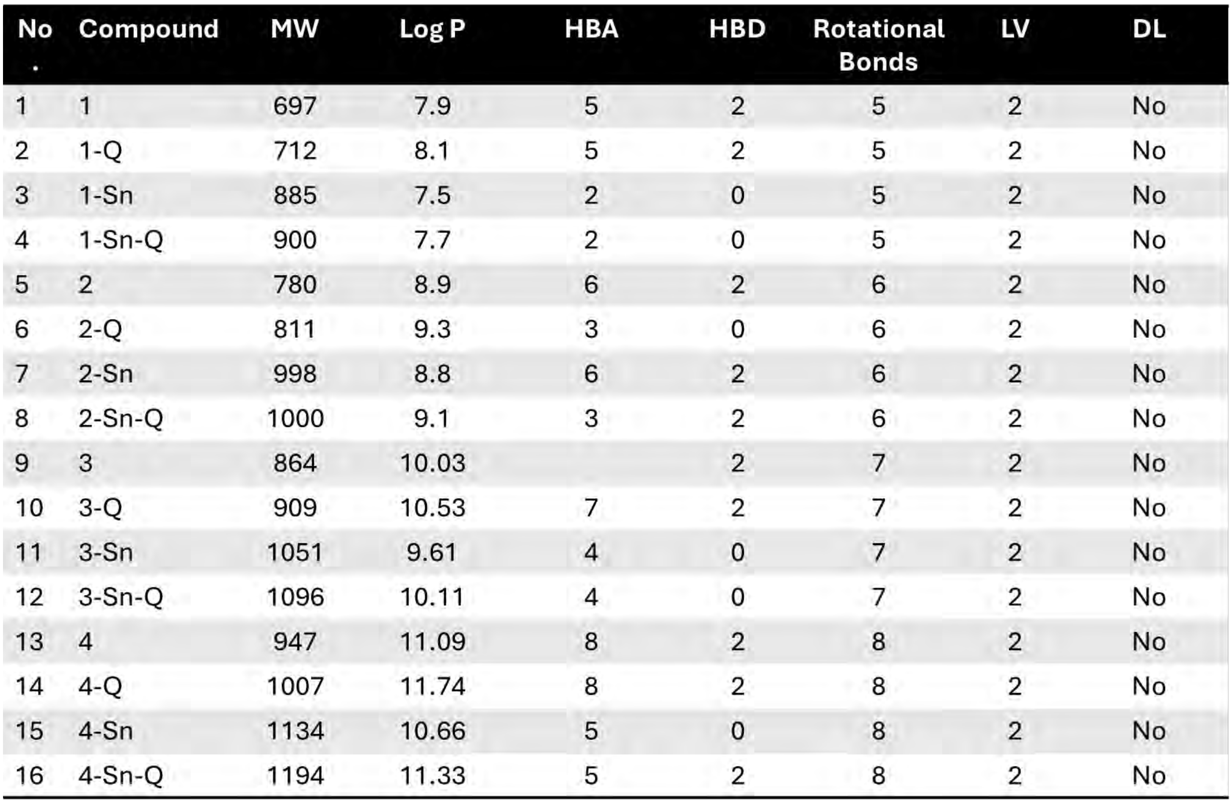

No.	Compound	MW	Log P	HBA	HBD	Rotational Bonds	LV	DL
1	1	697	7.9	5	2	5	2	No
2	1-Q	712	8.1	5	2	5	2	No
3	1-Sn	885	7.5	2	0	5	2	No
4	1-Sn-Q	900	7.7	2	0	5	2	No
5	2	780	8.9	6	2	6	2	No
6	2-Q	811	9.3	3	0	6	2	No
7	2-Sn	998	8.8	6	2	6	2	No
8	2-Sn-Q	1000	9.1	3	2	6	2	No
9	3	864	10.03		2	7	2	No
10	3-Q	909	10.53	7	2	7	2	No
11	3-Sn	1051	9.61	4	0	7	2	No
12	3-Sn-Q	1096	10.11	4	0	7	2	No
13	4	947	11.09	8	2	8	2	No
14	4-Q	1007	11.74	8	2	8	2	No
15	4-Sn	1134	10.66	5	0	8	2	No
16	4-Sn-Q	1194	11.33	5	2	8	2	No

MW: Molecular weight, **Log P**: Lipophilicity, **HBD**: Hydrogen Bond Donor, **HBA:** Hydrogen Bond Acceptor, Rotatable bonds (measure of molecular flexibility of a compound), **LV:** Lipinski Violation, **DL:** Drug-likeliness

ADMET Properties

ADMET properties are crucial in understanding the aftereffects of consuming certain drugs into the human body (**Table 6**). As much as we are using them to treat a certain disease, it is also important that they are not inducing other diseases during the envisaged PDT and/or PACT treatment procedure. The porphyrin analogues synthesized have no or very low blood-brain barrier penetration ability, so they can not affect the brain cells. They have low gastrointestinal absorption and are P-gp substrates, meaning they can be easily excreted out of the body. They do not inhibit CYP2D6, which is involved in drug metabolism. All of the compounds in this study are non-carcinogenic.

Table 6. ADMET properties of the porphyrin analogues predicted by ADMETlab 2.0.

No.	Compound	BBB	GI Absorption	P-gp Substrate	CYP2D6 Inhibitor	Log S	PSA	BA	C
1	1	No	Low	Yes	No	-2.62	59.54	0.55	NC
2	1-Q	No	Low	Yes	No	-14.34	56.30	0.17	NC
3	1-Sn	No	Low	Yes	No	-14.34	22.96	0.17	NC
4	1-Sn-Q	No	Low	Yes	No	-14.30	19.72	0.55	NC
5	2-ABAB	No	Low	Yes	No	-15.35	62.78	0.17	NC
6	2-Q-ABAB	No	Low	Yes	No	-15.26	56.30	0.55	NC
7	2-Sn-ABAB	No	Low	Yes	No	-15.35	26.20	0.17	NC
8	2-Sn-Q-ABAB	No	Low	Yes	No	-15.26	19.72	0.55	NC
9	3	No	Low	Yes	No	-16.36	66.02	0.17	NC
10	3-Q	No	Low	Yes	No	-16.23	56.30	0.55	NC
11	3-Sn	No	Low	Yes	No	-16.36	29.44	0.17	NC
12	3-Sn-Q	No	Low	Yes	No	-16.23	19.72	0.55	NC
13	4	No	Low	Yes	No	-16.23	69.26	0.55	NC
14	4-Q	No	Low	Yes	No	-16.23	56.30	0.55	NC
15	4-Sn	No	Low	Yes	No	-17.39	32.68	0.17	NC
16	4-Sn-Q	No	Low	Yes	No	-17.21	19.72	0.55	NC

BBB (Blood Brain Barrier) penetration ability: very Low, **PPB** (Plasma Protein Binding): > 50% is moderately bound, **GIA** (Gastrointestinal Absorption): 50–100% is for moderately absorbed compounds, **PSA** (Polar Surface Area): ≤90 Å2 is the optimum value, **Log S**: water solubility, **Log Kp**: Skin permeation, **BA** (Bioavailability score): 0.55 passes the rule-of-five, **C** (Carcinogenicity).

Concluding Remarks

The analysis of the computational docking and determination of the pharmacological properties was successfully conducted. Since the porphyrin analogues within Series 1 had negative binding affinity values, they are more likely to bind and interact with protein HSA in human plasma compared to the other porphyrin analogues series. Although all of the porphyrins violated Lipinski's rule of five, they are more likely to be administered through IV injection similar to Photofrin® rather than orally. They all have favourable ADMET properties and are predicted to be non-carcinogenic.

Chapter 7: TD-DFT calculations

Molecular Modelling

Theoretical calculations were carried out for all structures shown in **Scheme 1** to evaluate the effect of structural modification of porphyrinoids on their spectroscopic and optical properties. The effects of the transition from mono- to tetra piperidinyl phenyl substitution, metalation with an Sn(IV) ion and quaternisation of the piperidinyl phenyl nitrogen atom were evaluated. The UV-visible absorption spectra and MO energy plots obtained from the TD-DFT calculations (**Figures 37-53** and **Tables 7-12**) were used to identify trends in the optical spectroscopy and electronic structures of Series 1-4. Calculations were carried out for both the AABB and ABAB isomers in the context of Series 2. Two inner NH tautomers aligned with the *x*- and *y*-axes are possible in the context of the AABB isomers of **2** and **2-Q** (**Figure 44**). The *x*-axis tautomer is predicted to be slightly less stable in each case by 0.002 and 0.308 kcal/mol, respectively.

Calculations

The geometries of all porphyrinoid structures were optimised by using the Gaussian 09 software package [74] with the B3LYP exchange-correlation functional and SDD basis sets. The optimised geometries of porphyrinoids were then used for time-dependent density functional theory (TD-DFT) calculations, which were completed using CAM-B3LYP/SDD level theory at 50 lowest singlet-singlet transitions. The CAM-B3LYP functional was preferred in this context because it has a long-range correction, achieved by introducing increasing fractions of semi-empirical Hartree-Fock (HF) exchange parameters. The SDD basis sets facilitate comparisons with dyes and complexes containing the heavy Sn(IV) ion. The TD-DFT calculated excited states were used to generate absorption spectra and molecular orbital energy diagrams by using Chemcraft and Avogadro. TD-DFT calculations are known to systematically overestimate the energies of the Q and B excited states [46, 78], but trends observed across series of structurally related structures can still be readily compared to experimental data sets so that key structure-property relationships can be rationalised in terms of changes to the relative energies of the four frontier π-MOs (**Figure 3**) that are labelled the **a**, **s**, **-a**, **-s** MOs in the context of Michl's perimeter model [79] The electronic structure of the porphyrin ligand can be rationalized in terms of a $C_{16}H_{16}^{2-}$ cyclic polyene analogous to the inner ligand perimeter. This results in an $M_L = 0, \pm1, \pm2, \pm3, \pm4, \pm5, \pm6, \pm7, 8$ sequence in ascending energy terms. The MOs derived from the HOMO and LUMO of this parent perimeter have $M_L = \pm4$ and ±5 angular nodal patterns, respectively, and are referred to as the **a**/**-a** and **s**/**-s** depending on whether a nodal plane or large MO coefficients are aligned with the symmetry-defined *y*-axis (**Figures 41**, **44**, **47**, **50** and **53**), respectively.

Effect of Piperidinyl substitution

The series of calculations displayed in **Figure 37** were carried out to evaluate the effect of adding the peripheral piperidinyl groups (**Scheme 1**), which changes the ligand structure from the mono-substituted piperidinyl to di-, tri- and tetra-substituted porphyrin structures. Spectroscopically, as shown in **Figure 37**, the addition of the 4-piperidinylphenyl substituents to the porphyrin dyes from Series 1, 3, 3, 4 has a minimal observable effect on the wavelengths of the Q and B bands (**Figure 37**). As the number of 4-piperidinylphenyl substituents increases, the more the Q and B bands of the porphyrin are red shifted, which is an advantage for PDT studies in the context of the lower energy Q band since the band shifts further into the phototherapeutic window (620−850 nm). The red shift is due to the minimal constriction of the HOMO−LUMO gap observed in **Figure 38** due to a relative destabilisation of the **s** MO (i.e. the HOMO) since it has large MO coefficients on the *meso*-carbons where the 4-piperidinylphenyl groups are attached (**Figures 41**, **44**, **47**, **50** and **53**), Similar trends are observed for the metal complexes and quaternized dyes and complexes (**Figures 37-53** and **Tables 7-12**).

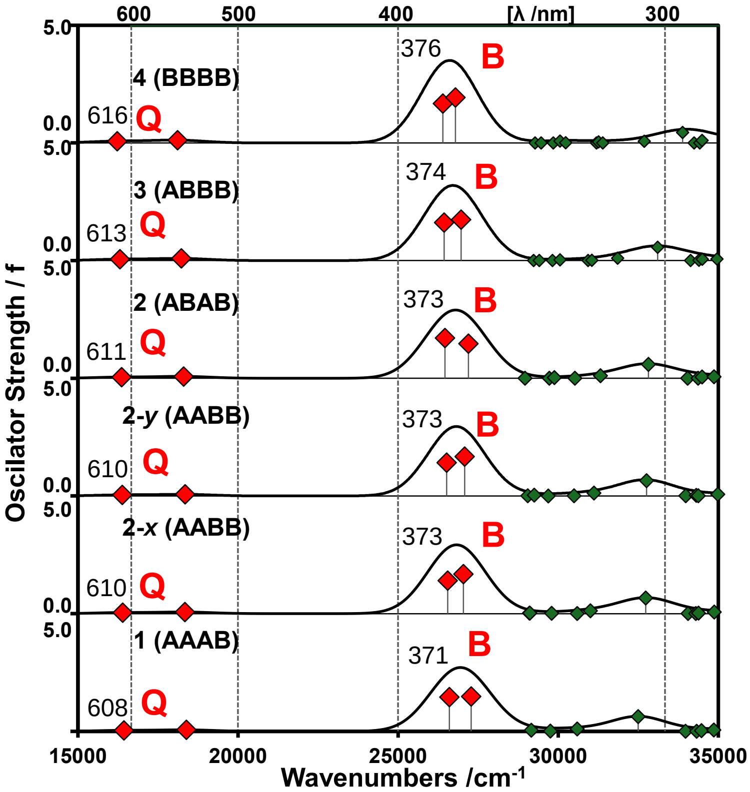

Figure 37. The calculated UV-visible absorption spectra of **1**, **2**, **3** and **4** from TD-DFT calculations at the CAM-B3LYP/SDD level of theory. Chemcraft was used to generate the simulated spectra at a bandwidth of 2000 cm^{-1}. The Q and B band maxima are provided in wavelength.

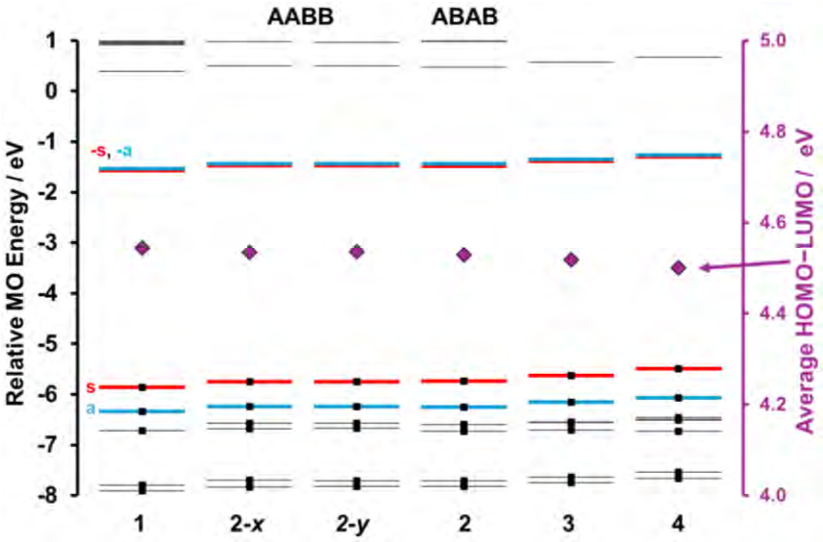

Figure 38. Molecular orbital energy diagram for **1**, **2**, **3** and **4**. Purple diamonds highlight the average HOMO−LUMO gap values taking into account the **a**, **s**, **-a** and **-s** MOs, which are plotted against the secondary *y*-axis. Occupied MOs are highlighted with small back squares.

Effect of Metalation

In the calculated spectra of metalated complexes, the B bands of **1-Sn** (387 nm), **2-Sn** (388 nm), **3-Sn** (391 nm) and **4-Sn** (394 nm) are red shifted compared to the free base ligands **1** (369 nm), **2** (371 nm), **3** (391 nm) and **4** (394 nm). Similar trends are observed for the Q bands (**Figures 37-53** and **Tables 7-12**). The red shift of the metalated compounds is due to the minimal observed constriction of the HOMO−LUMO gap, which is related to a relative destabilisation of the **s** MO (the HOMO), which has large MO coefficients on the pyrrole nitrogen atoms which coordinate the central Sn(IV) ion. Metalation with the Sn(IV) ion is expected to increase the singlet oxygen generation. The more the Q bands of the porphyrinoids are red-shifted, the more they are shifted into the phototherapeutic window (620−850 nm).

Effect of Quaternisation

Quaternisation of sp^3-hybridised nitrogen atoms with methyl iodide is potentially advantageous for photodynamic studies, since it enhances aqueous solubility [71, 72]. This increases porphyrin localisation because cancerous cells and bacterial cells are negatively charged [71, 72], resulting in a high force of attraction between cells and the PS dyes. **1-Q** (375 nm), **2-Q** (368 nm), **3-Q** (368 nm) and **4-Q** (366 nm) have blue shifted spectral bands compared to the free base dyes **1** (369 nm), **2** (371 nm), **3** (391 nm) and **4** (394 nm). Similar trends are observed in the Q bands (**Figures 37-53** and **Tables 7-12**). There is an increase in the HOMO−LUMO gaps, which is related to a relative stabilisation of the **s** MO (the HOMO), which has large MO coefficients on the *meso*-carbons where the 4-piperidinylphenyl substituents are introduced (**Figures 41**, **44**, **47**, **50** and **53**).

Effect of combination of metalation and quaternisation

The combination of metalation and quaternisation on all compounds has the same effect on the porphyrin B-band, where their major spectral bands lie between the wavelengths of the metalated and quaternised compounds alone (**Figures 37-53** and **Tables 7-12**).

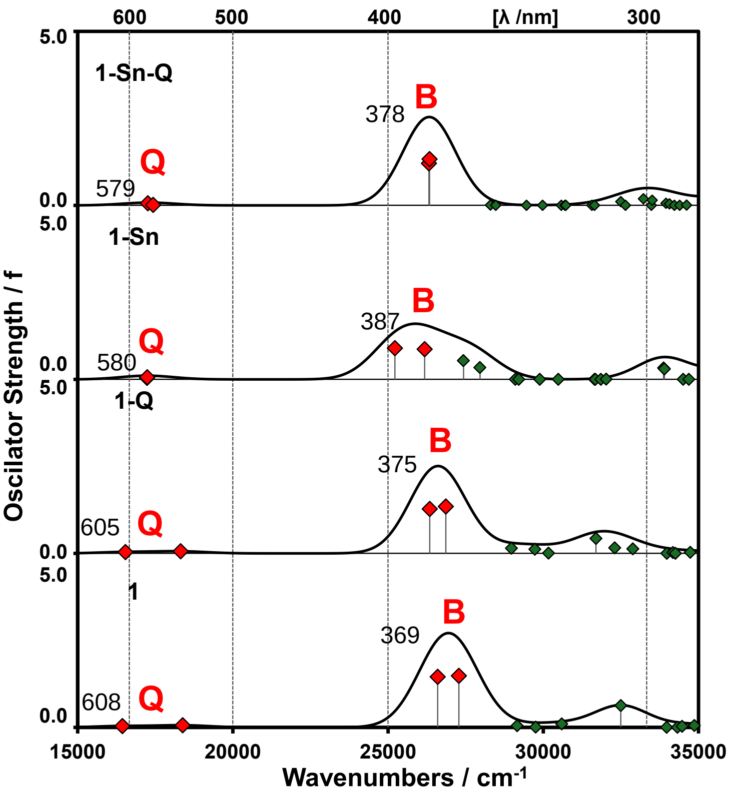

Figure 39. The UV-visible absorption spectra of **1**, **1-Q**, **1-Sn** and **1-Sn-Q** from TD-DFT calculations at the CAM-B3LYP/SDD level of theory. Chemcraft was used to generate the simulated spectra at a fixed bandwidth of 2000 cm^{-1}. The Q and B band maxima are provided in nanometres. The details of the calculations are provided in **Table 7**.

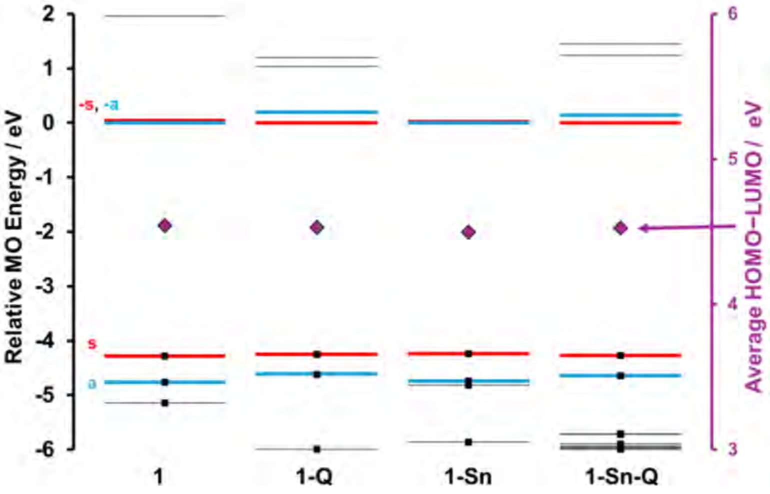

Figure 40. Molecular orbital energy diagram for **1**, **1-Q**, **1-Sn** and **1-Sn-Q**, normalised so that the LUMO energy is set to zero. Purple diamonds highlight the average HOMO−LUMO gap values taking into account the **a**, **s**, **-a** and **-s** MOs, which are plotted against the secondary *y*-axis. Occupied MOs are highlighted with small back squares. The angular nodal patterns and MO energies of the **a**, **s**, **-a** and -s MOs are provided in **Figure 41**.

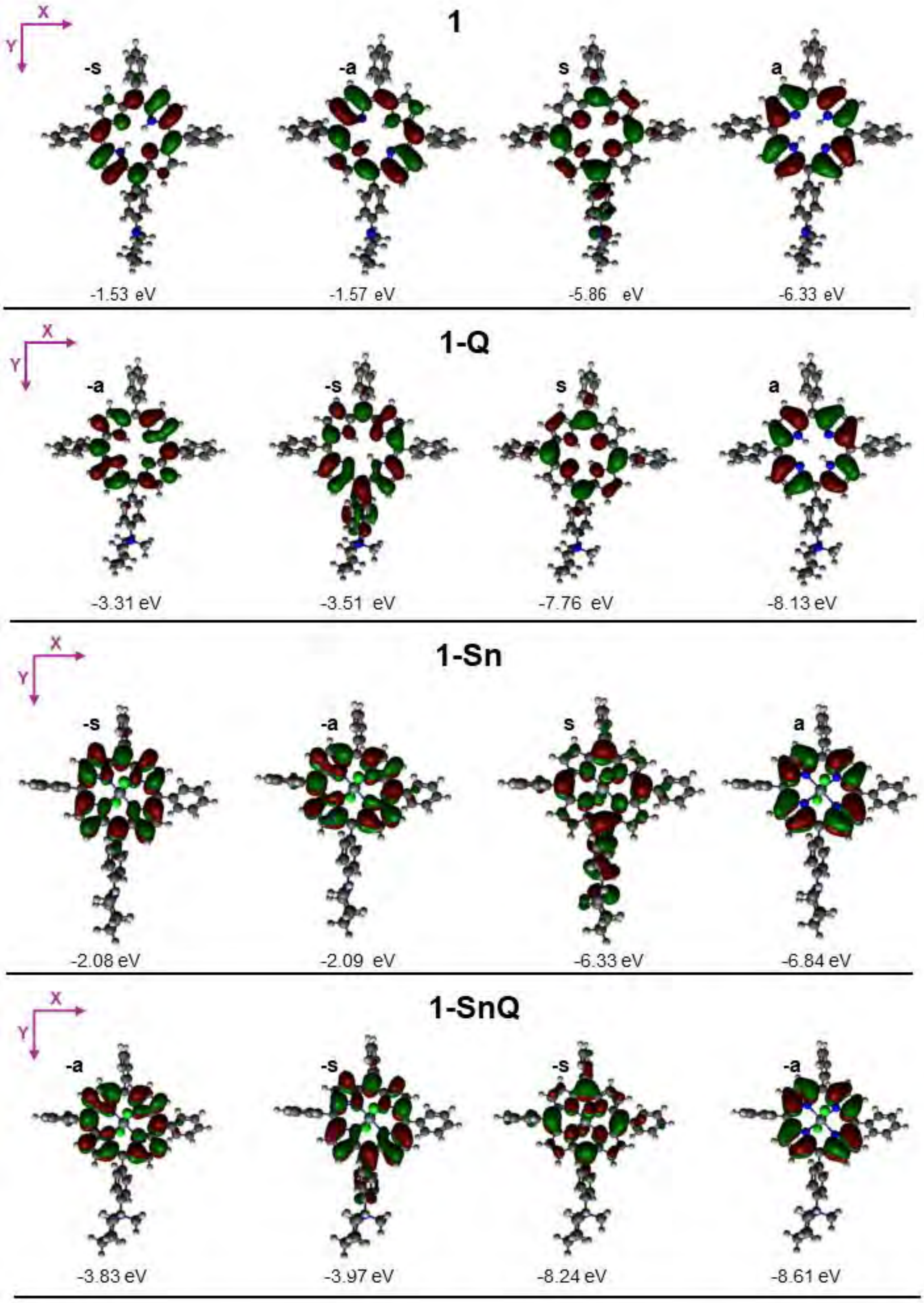

Figure 41. The four frontier π-MOs of **1**, **1-Q**, **1-Sn** and **1-Sn-Q** derived from the HOMO and LUMO of a $C_{16}H_{16}^{2-}$ parent perimeter are referred to as the **a**, **s**, **-a**, and **-s** MOs in the context of Michl's perimeter model [79]. The MO plots are provided at an isosurface of 0.02 a.u.

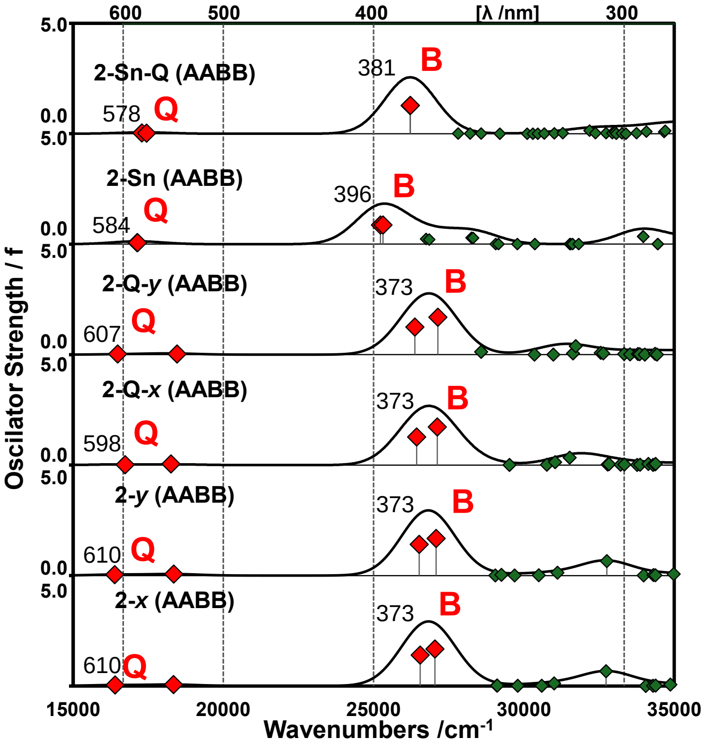

Figure 42. The calculated UV-visible absorption spectra of the AABB isomers of **2**, **2-Q**, **2-Sn** and **2-Sn-Q** from TD-DFT calculations at the CAM-B3LYP/SDD level of theory. Two inner NH tautomers are possible for **2** and **2-Q** (**Figure 44**). Chemcraft was used to generate the simulated spectra at a fixed bandwidth of 2000 cm^{-1}. The details of the calculations are provided in **Table 8**.

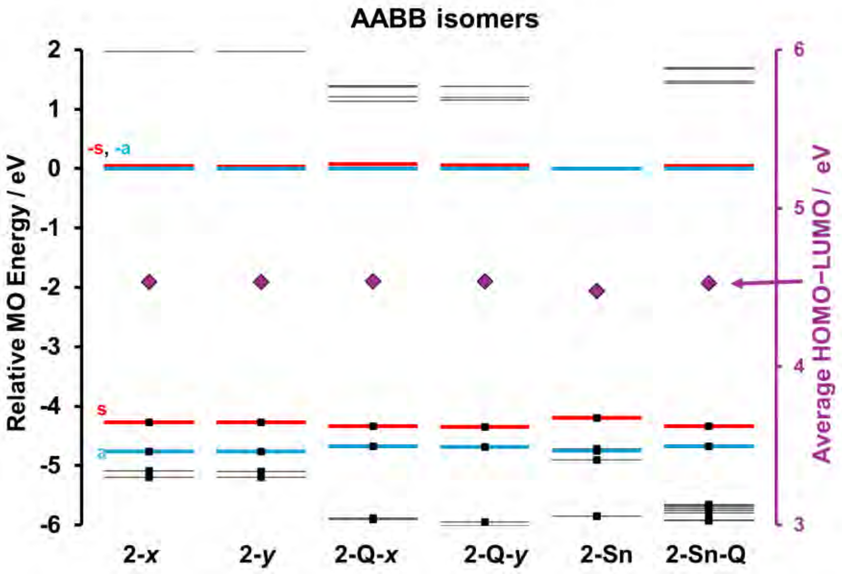

Figure 43. Molecular orbital energy diagram for the AABB isomer structures of **2**, **2-Q**, **2-Sn** and **2-Sn-Q**, normalised so that the LUMO energy is set to zero. Purple diamonds highlight the average HOMO−LUMO gap values taking into account the **a**, **s**, **-a** and **-s** MOs, which are plotted against the secondary *y*-axis. Occupied MOs are highlighted with small back squares. The different inner NH tautomers are possible for **2** and **2-Q**. The angular nodal patterns and MO energies of the **a**, **s**, **-a** and -s MOs are provided in **Figure 44**.

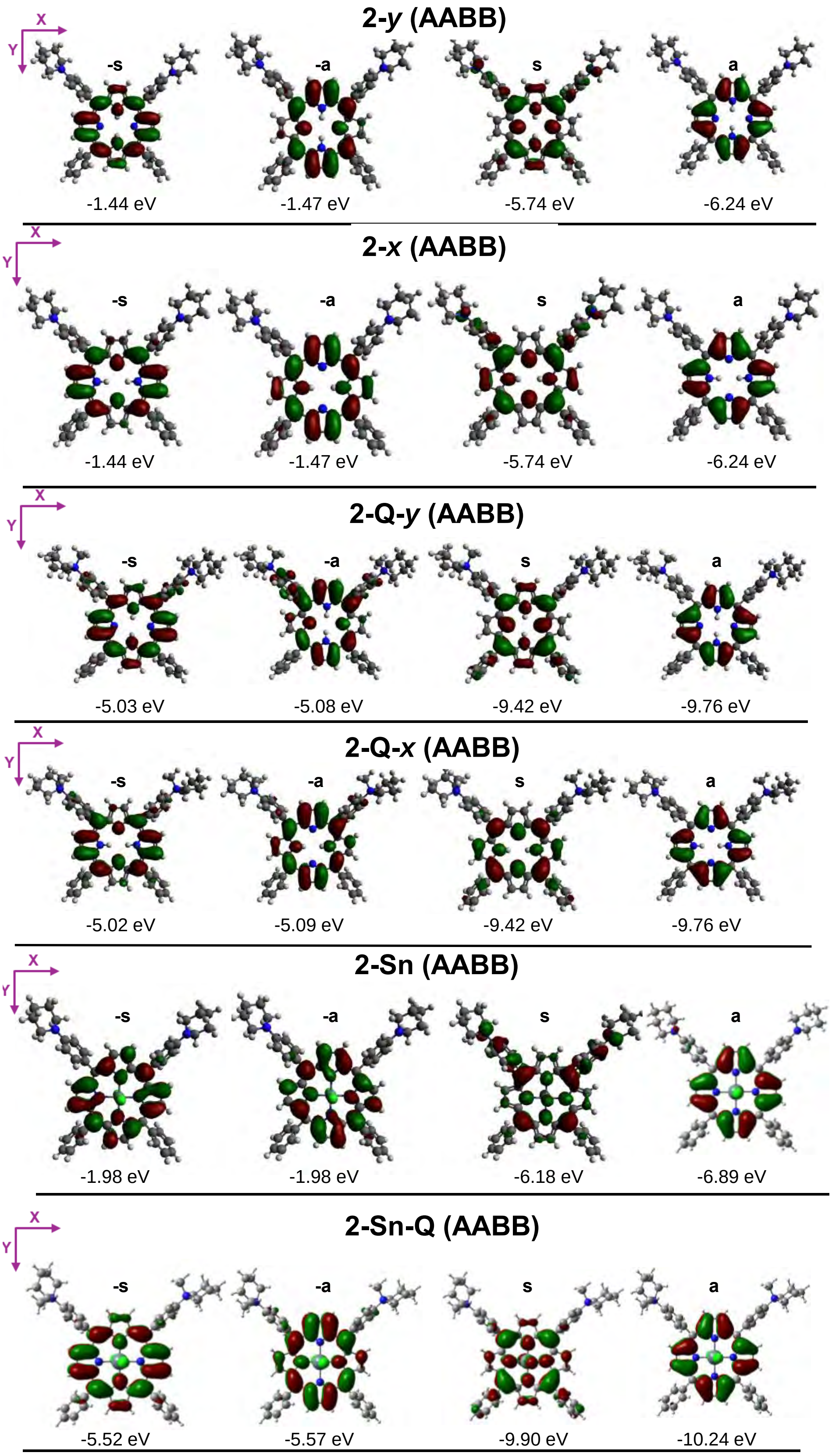

Figure 44. The four frontier π-MOs for the AABB isomer structures of **2**, **2-Q**, **2-Sn** and **2-Sn-Q** derived from the HOMO and LUMO of a $C_{16}H_{16}^{2-}$ parent perimeter are referred to as the **a**, **s**, **-a**, and **-s** MOs in the context of Michl's perimeter model [79]. The MO plots are provided at an isosurface of 0.02 a.u.

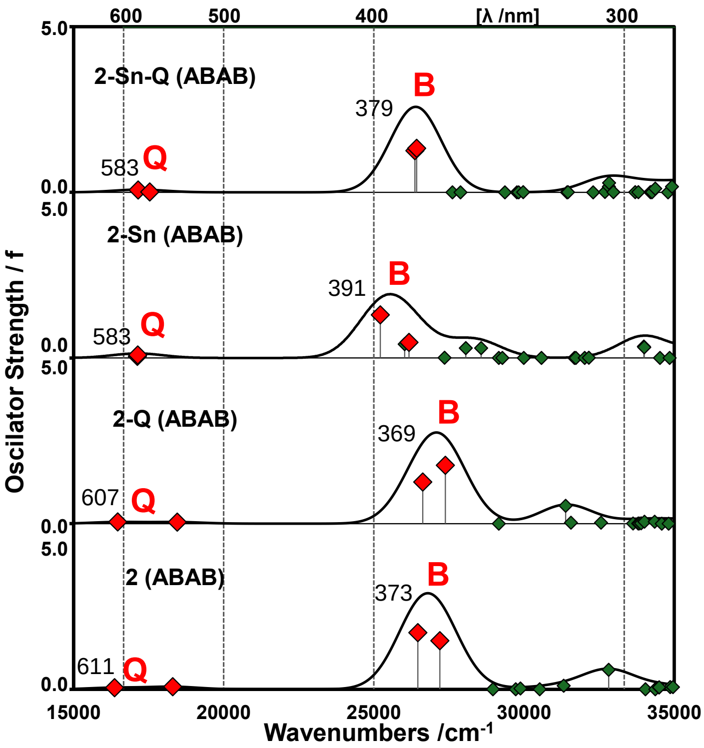

Figure 45. The calculated UV-visible absorption spectra for the ABAB isomers of **2**, **2-Q**, **2-Sn** and **2-Sn-Q** from TD-DFT calculations at the CAM-B3LYP/SDD level of theory. Chemcraft was used to generate the simulated spectra at a bandwidth of 2000 cm^{-1}. The Q and B band maxima are provided in nanometres. The details of the calculations are provided in **Table 9**.

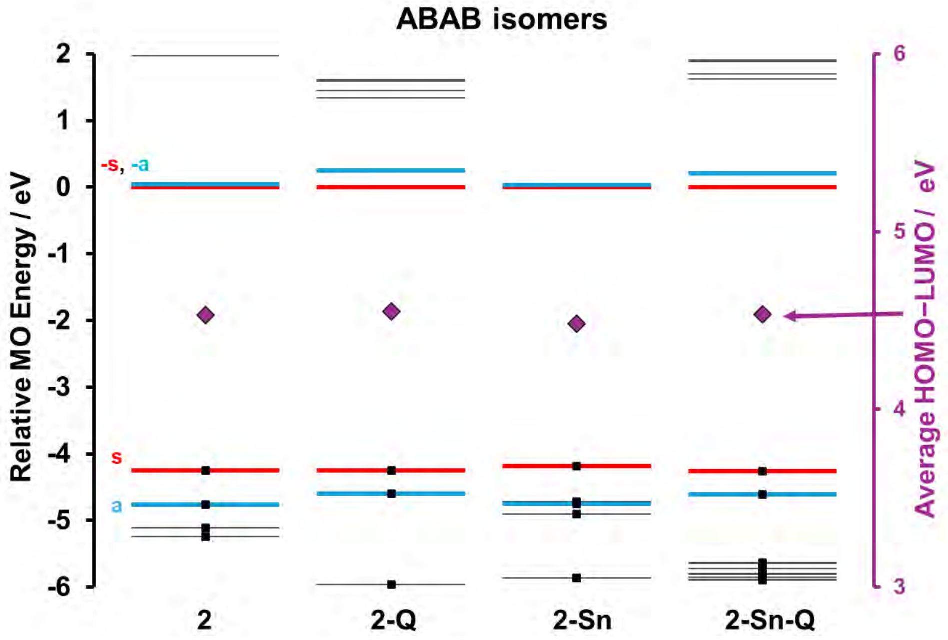

Figure 46. Molecular orbital energy diagram of the ABAB isomers of **2**, **2-Q**, **2-Sn** and **2-Sn-Q**, normalised so that the LUMO energy is set to zero. Purple diamonds highlight the average HOMO−LUMO gap values taking into account the **a**, **s**, **-a** and **-s** MOs, which are plotted against the secondary *y*-axis. Occupied MOs are highlighted with small back squares. The angular nodal patterns and MO energies of the **a**, **s**, **-a** and **-s** MOs are provided in **Figure 47**.

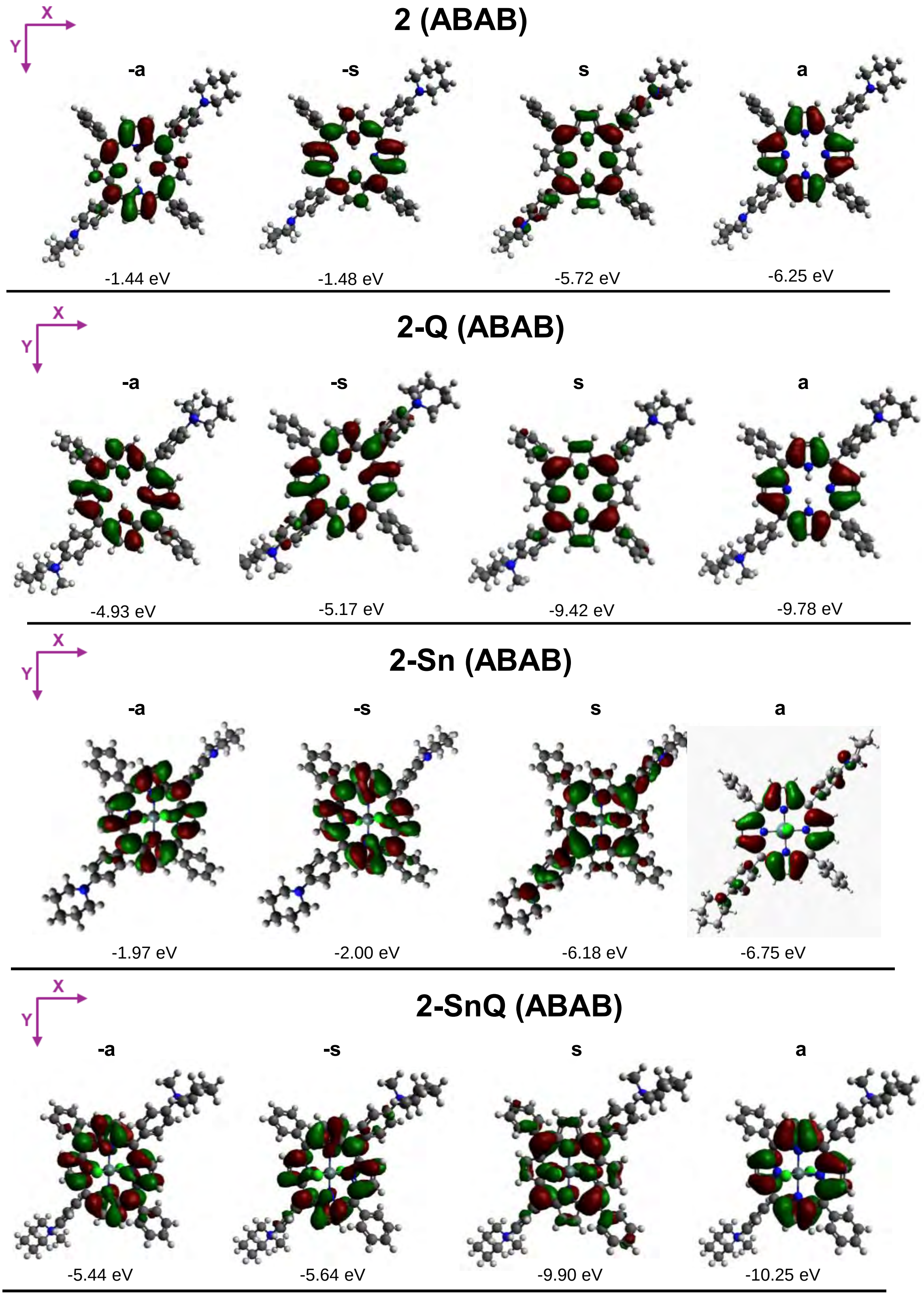

Figure 47. The four frontier π-MOs for the ABAB isomers of **2**, **2-Q**, **2-Sn** and **2-Sn-Q** derived from the HOMO and LUMO of a $C_{16}H_{16}^{2-}$ parent perimeter are referred to as the **a**, **s**, **-a**, and **-s** MOs in the context of Michl's perimeter model [79]. The MO plots are provided at an isosurface of 0.02 a.u.

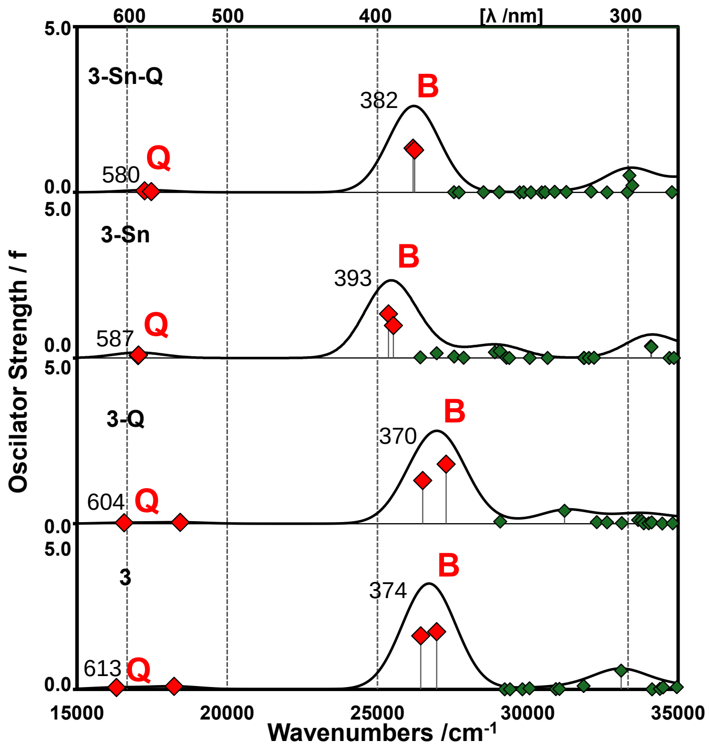

Figure 48. The calculated UV-visible absorption spectra of **3**, **3-Q**, **3-Sn** and **3-Sn-Q** from TD-DFT calculations at the CAM-B3LYP/SDD level of theory. Chemcraft was used to generate the simulated spectra at a bandwidth of 2000 cm^{-1}. The Q and B band maxima are provided in nanometres. The details of the calculations are provided in **Table 10**.

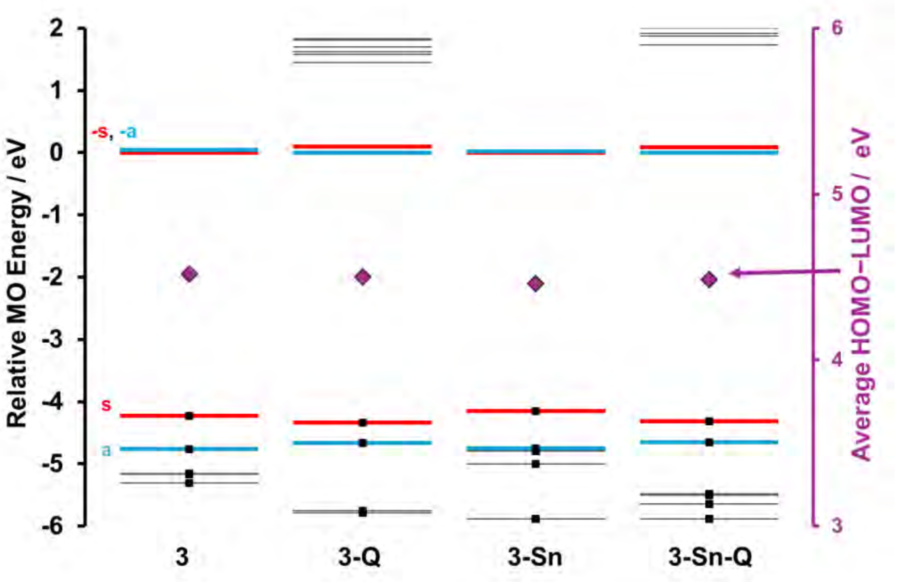

Figure 49. Molecular orbital energy diagram for **3**, **3-Q**, **3-Sn** and **3-Sn-Q**, normalised so that the LUMO energy is set to zero. Purple diamonds highlight the average HOMO−LUMO gap values taking into account the **a**, **s**, **-a** and **-s** MOs, which are plotted against the secondary *y*-axis. Occupied MOs are highlighted with small back squares. The angular nodal patterns and MO energies of the **a**, **s**, **-a** and -s MOs are provided in **Figure 50**.

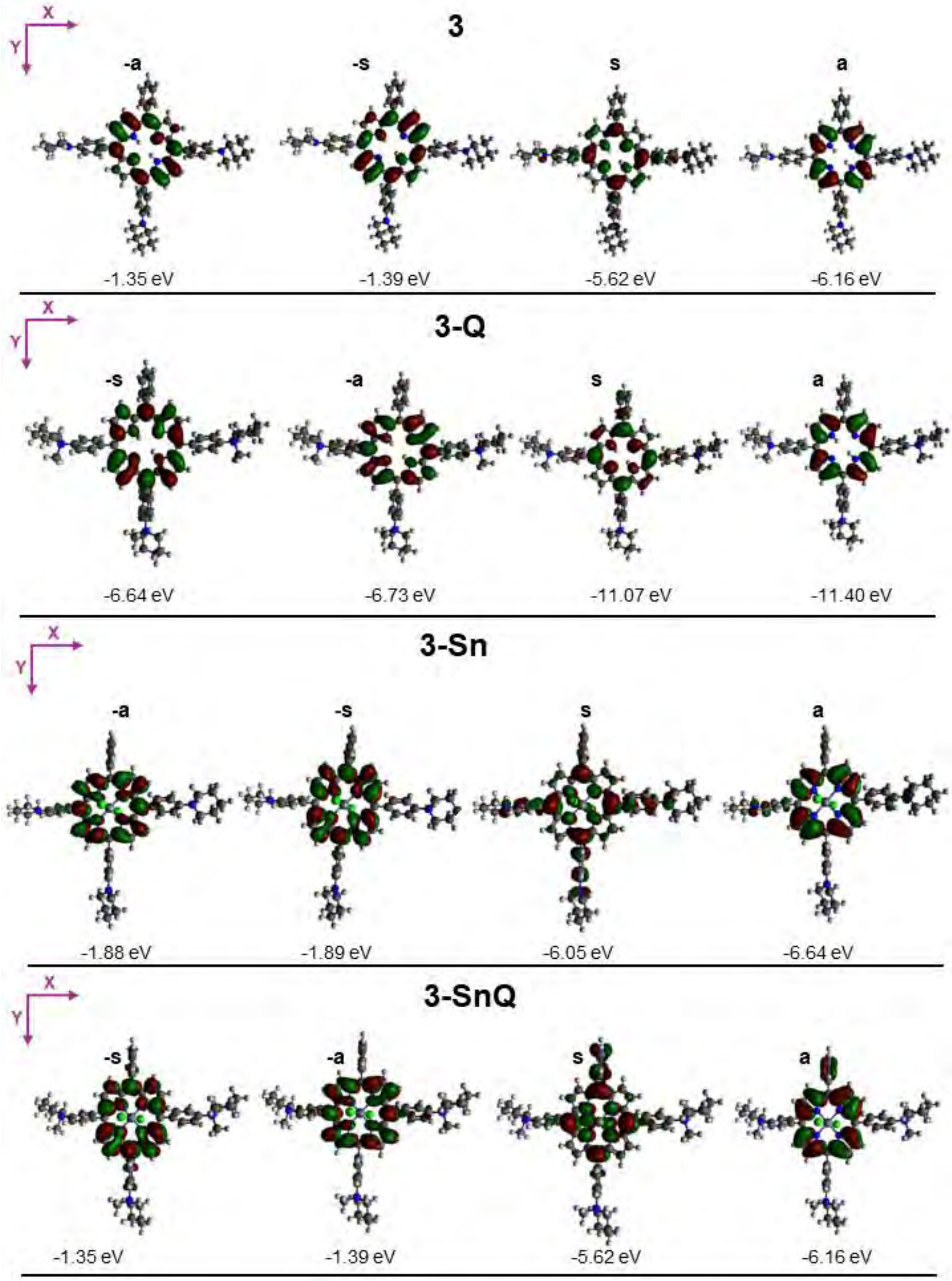

Figure 50. The four frontier π-MOs of **3**, **3-Q**, **3-Sn** and **3-Sn-Q** derived from the HOMO and LUMO of a $C_{16}H_{16}^{2-}$ parent perimeter are referred to as the **a**, **s**, **-a**, and **-s** MOs in the context of Michl's perimeter model [79]. The MO plots are provided at an isosurface of 0.02 a.u.

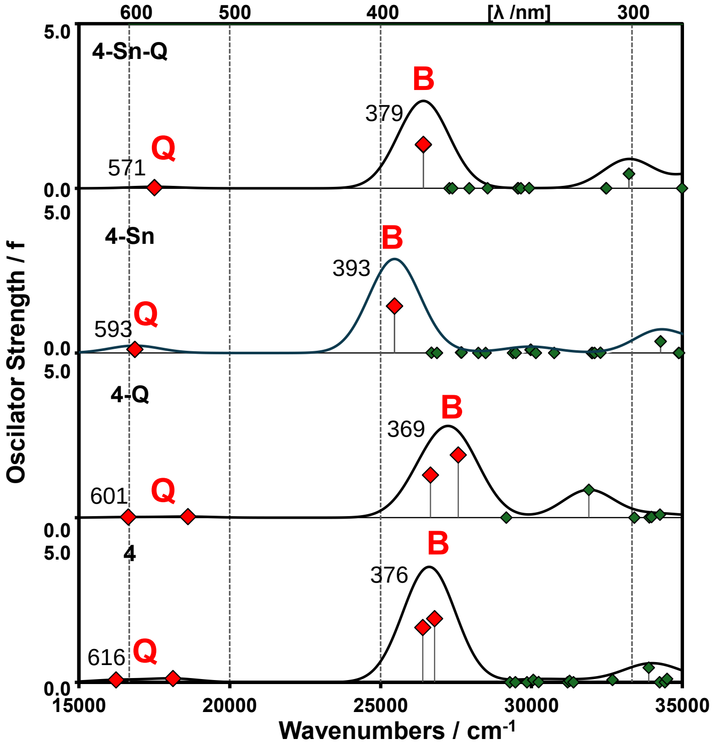

Figure 51. The calculated UV-visible absorption spectra of **4**, **4-Q**, **4-Sn** and **4-Sn-Q** from TD-DFT calculations at the CAM-B3LYP/SDD level of theory. Chemcraft was used to generate the simulated spectra at a bandwidth of 2000 cm^{-1}. The Q and B band maxima are provided in nanometres. The details of the calculations are provided in **Table 11**.

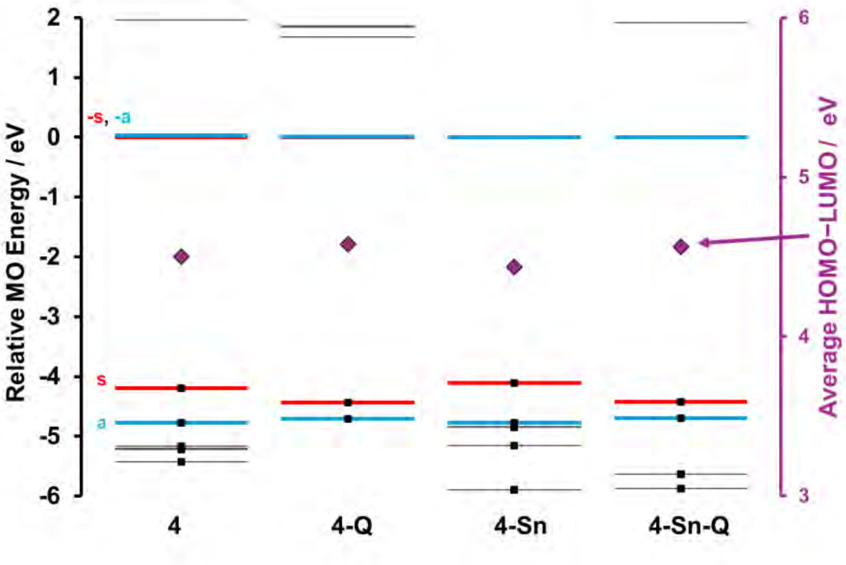

Figure 52. Molecular orbital energy diagram for **4**, **4-Q**, **4-Sn** and **4-Sn-Q**, normalised so that the LUMO energy is set to zero. Purple diamonds highlight the average HOMO−LUMO gap values taking into account the **a**, **s**, **-a** and **-s** MOs, which are plotted against the secondary *y*-axis. Occupied MOs are highlighted with small back squares. The angular nodal patterns and MO energies of the **a**, **s**, **-a** and -s MOs are provided in **Figure 53**.

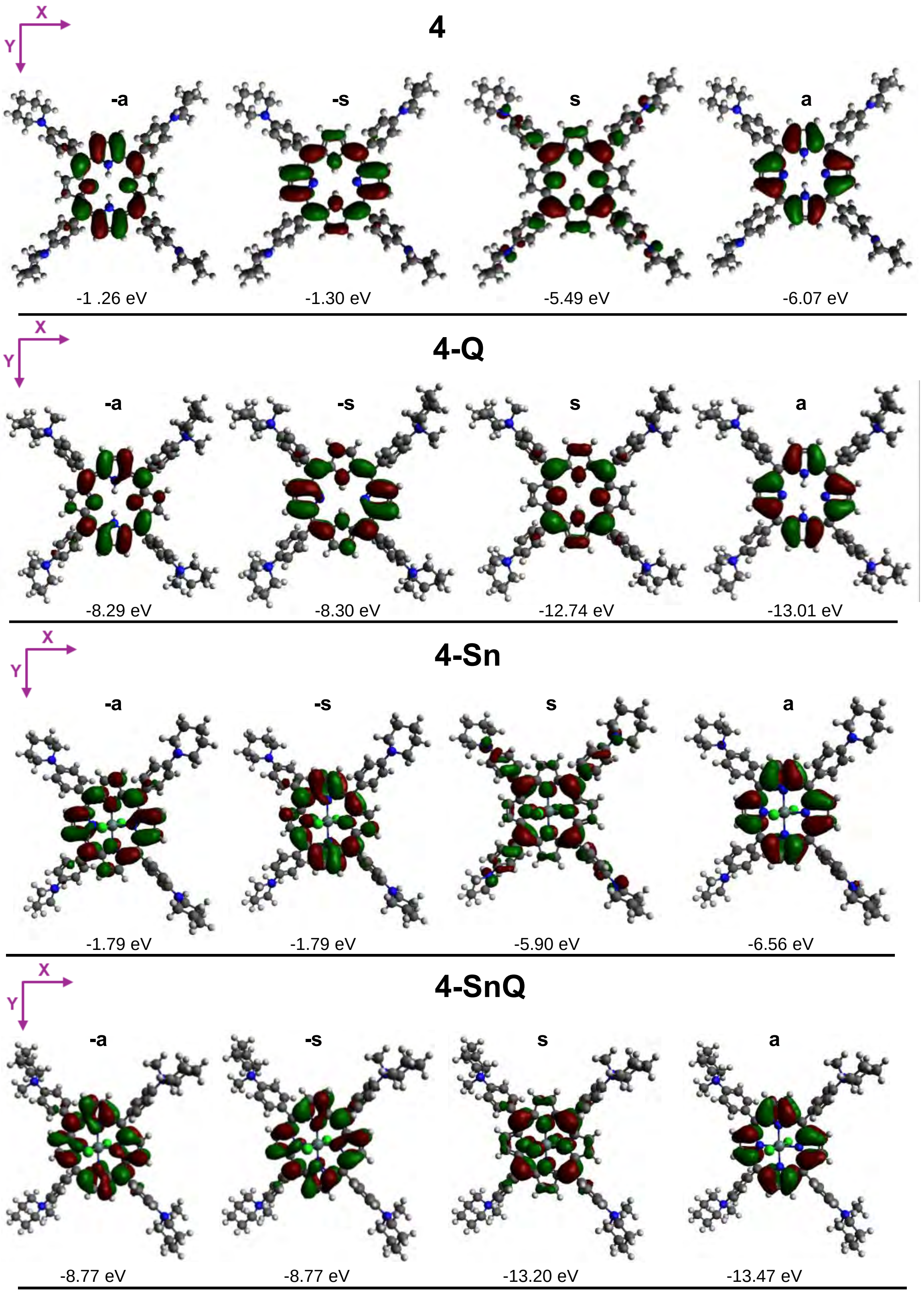

Figure 53. The four frontier π-MOs of **4**, **4-Q**, **4-Sn** and **4-Sn-Q** derived from the HOMO and LUMO of a $C_{16}H_{16}^{2-}$ parent perimeter are referred to as the **a**, **s**, **-a**, and **-s** MOs in the context of Michl's perimeter model [79]. The MO plots are provided at an isosurface of 0.02 a.u.

Table 7. Calculated TD-DFT UV-visible spectra of the B3LYP optimized geometries of Series 1 analogues at the CAM-B3LYP/SDD level of theory.

Band[a]	**#**[b]	**Calc**[c]		**Exp**[d]	**Wave Function**[e] **=**
		λ (nm)	F	λ (nm)	
1					
----	1	---	---	---	Ground State
Q	2	608	0.04	651	**61% s → -s; 32% a → -a;** …
	3	544	0.06	554	**59% s → -a; 35% a → -s;** …
B	4	376	1.46	419	**41% a → -a; 21% s → -s; 16% a → -s; 11% s → -a;** …
	5	367	1.48		**38% -a → s; 26% s → -a; 20% a → -a; 10% s → -s;** …
1-Q					
----	1	---	---	---	Ground State
Q	2	605	0.04	646	**38% s → -s; 26% s → -a; 18% a → -a; 17% a → -s;** …
	3	546	0.06	549	**31% s → -a; 29% s → -s; 25% a → -s; 14% a → -a;** …
	4	380	1.28		**41% a → -a; 19% s → -s; 15% a → -s; 9% s → -a;** …
B	5	372	1.35	419	**40% a → -s; 29% s → -a; 11% a → -a;** 10% s → LUMO+2; **9% s → -s;** …
1-Sn					
----	1	---	---	---	Ground State
Q	2	580	0.04	611	**60% s → -s; 33% a → -a;** …
	3	580	0.06		**61% s → -a; 33% a → -s;** …
B	4	396	0.90	422	**32%** HOMO−2 → a; **31% -s → s; 31% -a → a;** …
	5	382	0.87		**53% a → -a; 38% s → -s;** …
1-Sn-Q					
----	1	---	---	---	Ground State
Q	2	579	0.06	599	**67% -s → s; 32% -a → a;** …
	3	574	0.02	557	**59% -s → a; 40% -a → s;** …
B	4	380	1.21	425	**56% -a → s; 36% -s → a;** …
	5	380	1.33		**62% -a → a; 28% -s → s;** …

[a] Band assignment described in the main text. [b] States assigned in terms of ascending energy in the TD-DFT calculation. [c] Calculated wavelengths (nm) with oscillator strengths in parentheses (f). [d] Observed wavelengths (nm) in DMSO, [e] The wave functions calculated from the eigenvectors predicted by TD-DFT. One-electron transitions associated with the **a**, **s**, **-a**, and **-s** MOs of Michl's perimeter model [79] are highlighted in bold. Only one-electron transition contributions > 10% are shown.

Table 8. Calculated TD-DFT UV-visible spectra of the B3LYP optimized geometries of Series 2 (AABB) analogues at the CAM-B3LYP/SDD level of theory.

Band[a]	**#**[b]	**Calc**[c]		**Exp**[d]	**Wave Function**[e] **=**
		λ (nm)	F	λ (nm)	
2-*x* (AABB)					
----	1	---	---	---	Ground State
Q	2	610	0.04	654	**64% s → -a; 33% a → -s;** …
	3	545	0.07	565	**62% s → -s; 36% a → -a;** …
B	4	377	1.40	421	**59% a → -s; 30% -s → -a;** …
	5	370	1.67		**53% a → -a; 34% s → -s;** …
2-*y* (AABB)					
----	1	---	---	---	Ground State
Q	2	610	0.04	654	**64% s → -s; 33% a → -a; …**
	3	545	0.07	565	**62% s → -a; 36% a → -s; …**
B	4	377	1.41	421	**60% a → -s; 30% s → -s; …**
	5	369	1.68		**54% a → -s; 34% s → -a; …**
2-Q-*x* (AABB)					
----	1	---	---	---	Ground State
Q	2	598	0.02	645	**61% s → -a; 37% a → -s;** …
	3	548	0.05	555	**61% s → -s; 37% a → -a;** …
B	4	378	1.27	419	**57% a → -a; 30% s → -s;** …
	5	369	1.73		**58% a → -s; 35% s → -a;** …
2-Q-*y* (AABB)					
----	1	---	---	---	Ground State
Q	2	607	0.03	645	**63% s → -a; 35% a → -s;** …
	3	542	0.03	555	**58% s → -s; 40% a → -a;** …
B	4	379	1.25	419	**57% a → -s; 27% s → -a;** …
	5	368	1.69		**56% a → -a; 38% s → -s;** …
2-Sn (AABB)					
----	1	---	---	---	
Q	2	584	0.06	606	**45% s → -a; 24% a → -s; 17% s → -s;** …
	3	583	0.06		**45% s → -s; 24% a → -a; 17% s → -a;** …
B	4	396	0.87	424	20% HOMO−2 → -s; **14% a → -s; 14% a → -a; 14% s → -s; 12% s → -a;** …
	5	395	0.87		**22% a → -a; 18% a → -s; 14% s → -a; 12% s → -s;** 11% HOMO−2 → -a; …
2-Sn-Q (AABB)					
----	1	---	---	---	Ground State
Q	2	578	0.04	604	**63% s → -a; 36% a → -s;** …
	3	573	0.03		**61% s → -s; 37% a → -a;** …
B	4	381	1.28	422	**55% a → -s; 31% s → -a;** …
	5	381	1.28		**54% a → -a; 31% s → -s;** …

[a] Band assignment described in the main text. [b] States assigned in terms of ascending energy in the TD-DFT calculation. [c] Calculated wavelengths (nm) with oscillator strengths in parentheses (f). [d] Observed wavelengths (nm) in DMSO, [e] The wave functions calculated from the eigenvectors predicted by TD-DFT. One-electron transitions associated with the **a**, **s**, **-a**, and **-s** MOs of Michl's

perimeter model [79] are highlighted in bold. Only one-electron transition contributions > 10% are shown.

Table 9. Calculated TD-DFT UV-visible spectra of the B3LYP optimized geometries of Series 2 (ABAB) analogues at the CAM-B3LYP/SDD level of theory.

Band[a]	**#**[b]	**Calc**[c]		**Exp**[d]	**Wave Function**[e] **=**
		λ (nm)	F	λ (nm)	
					2 (ABAB)
----	1	---	---	---	Ground State
Q	2	611	0.05	654	**59% s → -s; 30% a → -a;** …
	3	546	0.08	565	**57% s → -a; 32% a → -s;** …
B	4	378	1.71	421	**31% a → -a; 28% a → -s; 17% s → -a; 15% s → -s;** …
	5	368	1.47		**32% a → -a; 30% a → -s; 19% s → -a; 16% s → -s;** …
					2-Q (ABAB)
----	1	---	---	---	Ground State
Q	2	607	0.05	645	**47% s → -s; 22% a → -a; 18% s → -a; 13% a → -s;** …
	3	542	0.05	555	**37% s → -a; 32% a → -s; 21% s → -s; 10% a → -a;** …
B	4	376	1.26	419	**30% a → -a; 27% a → -s; 21% s → -a; 11% s → -s;** …
	5	365	1.76		**34% a → -a; 26% a → -s; 21% s → -a; 18% s → -s;** …
					2-Sn (ABAB)
----	1	---	---	---	Ground State
Q	2	584	0.05	606	**62% s → -s; 27% a → -a;** …
	3	583	0.09		**63% s → -a; 28% a → -s;** …
B	4	397	1.30	424	**37% a → -s; 34% s → -a;** 19% HOMO−3 → -a; …
	6	382	0.47		**57% a → -a; 20% s → -s;** …
					2-Sn-Q (ABAB)
----	1	---	---	---	Ground State
Q	2	583	0.07	604	**69% s → -s; 31% a → -a;** …
	3	570	0.01		**57% s → -a; 42% a → -s;** …
B	4	379	1.26	422	**55% a → -s; 39% s → -a;** …
	5	378	1.32		**66% a → -a; 26% s → -s;** …

[a] Band assignment described in the main text. [b] States assigned in terms of ascending energy in the TD-DFT calculation. [c] Calculated wavelengths (nm) with oscillator strengths in parentheses (f). [d] Observed wavelengths (nm) in DMSO, [e] The wave functions calculated from the eigenvectors predicted by TD-DFT. One-electron transitions associated with the **a**, **s**, **-a**, and **-s** MOs of Michl's perimeter model [79] are highlighted in bold. Only one-electron transition contributions > 10% are shown.

Table 10. Calculated TD-DFT UV-visible spectra of the B3LYP optimized geometries of Series 3 analogues at the CAM-B3LYP/SDD level of theory.

Band[a]	**#**[b]	**Calc**[c]		**Exp**[d]	**Wave Function**[e] =
		λ (nm)	F	λ (nm)	
				3	
----	1	---	---	---	Ground State
Q	2	613	0.06	654	**63% s → -s; 31% a → -a;** …
	3	548	0.09	561	**62% s → -s; 33% a → -s;** …
B	4	378	1.62	419	**52% a → -a; 25% s → -s; 10% a → -s;** …
	5	371	1.74		**49% a → -s; 30% s → -a; 10% a → -a;** …
				3-Q	
----	1	---	---	---	Ground State
Q	2	604	0.03	644	**42% s → -s; 21% s → -a; 23% a → -a; 13% a → -s;** …
	3	543	0.04	549	**37% s → -a; 27% a → -s; 22% s → -s; 13% a → -a;** …
B	4	377	1.31	419	**29% a → -s; 28% a → -a; 18% s → -a; 13% s → -s;** …
	5	367	1.80		**33% a → -a; 27% a → -s; 20% s → -s; 20% s → -a;**
				3-Sn	
----	1		---	---	Ground State
Q	2	587	0.07	~635	**64% s → -s; 27% a → -a;** …
	3	587	0.09		**64% s → -a; 27% a → -s;** …
B	4	394	1.33	~422	**45% a → -s; 31% s → -a;** 11% HOMO−4 → -a; …
	5	392	0.98		**42% -a → a; 27% -s → s;** …
				3-Sn-Q	
----	1	---	---	---	Ground State
Q	2	580	0.04	~615	**65% s → -s; 34% a → -a;** …
	3	572	0.02		**60% s → -a; 39% a → -s;** …
B	4	382	1.33	~424	**57% a → -s; 36% s → -a;** …
	5	381	1.27		**62% a → -a; 31% s → -s;** …

[a] Band assignment described in the main text. [b] States assigned in terms of ascending energy in the TD-DFT calculation. [c] Calculated wavelengths (nm) with oscillator strengths in parentheses (f). [d] Observed wavelengths (nm) in DMSO, [e] The wave functions calculated from the eigenvectors predicted by TD-DFT. One-electron transitions associated with the **a**, **s**, **-a**, and **-s** MOs of Michl's perimeter model [79] are highlighted in bold. Only one-electron transition contributions > 10% are shown.

Table 11. Calculated TD-DFT UV-visible spectra of the B3LYP optimized geometries of Series 4 analogues at the CAM-B3LYP/SDD level of theory.

Band[a]	**#**[b]	**Calc**[c]		**Exp**[d]	**Wave Function**[e] **=**
		λ (nm)	F	λ (nm)	
				4	
----	1	--	---	---	Ground State
Q	2	616	0.07	655	**66% s → -s; 31% a → -a;** …
	3	552	0.11	563	**65% s → -a; 32% a → -s;** …
B	4	379	1.67	421	**64% a → -a; 27% s → -s;** …
	5	373	1.93		**61% a → -s; 31% s → -a;** …
				4-Q	
----	1	---	---	---	Ground State
Q	2	601	0.01	646	**56% s → -s; 35% a → -a;** …
	3	537	0.03	552	**53% s → -a; 38% a → -s;** …
B	4	375	1.29	419	**52% a → -a; 28% s → -s;** 11% HOMO−3 → **-s;** …
	5	363	1.90		**53% a → -s; 39% s → -a;** …
				4-Sn	
----	1	---	---	---	Ground State
Q	2	593	0.11	~650	**60% s → -s; 25% a → -a;** …
	3		0.11		**60% s → -a; 25% a → -s;** …
B	4	393	1.43	~420	**51% a → -a; 27% s → -s;** …
	5		1.42		**52% a → -s; 27% s → -a;** …
				4-Sn-Q	
----	1	---	---		Ground State
Q	2	571	0.02	~630	**60% s → -s; 38% s → -a;** …
	3		0.02		**60% s → -a; 38% s → -s;** …
B	4	379	1.32	~420	**57% a → -s; 36% s → -a;** …
	5		1.34		**57% a → -a; 36% s → -s;** …

[a] Band assignment described in the main text. [b] States assigned in terms of ascending energy in the TD-DFT calculation. [c] Calculated wavelengths (nm) with oscillator strengths in parentheses (f). [d] Observed wavelengths (nm) in DMSO, [e] The wave functions calculated from the eigenvectors predicted by TD-DFT. One-electron transitions associated with the **a**, **s**, **-a**, and **-s** MOs of Michl's perimeter model [79] are highlighted in bold. Only one-electron transition contributions > 10% are shown.

Table 12. Calculated TD-DFT UV-visible spectra of the B3LYP optimized geometries of free base tetraphenyl porphyrin ($\mathrm{H_2TPP}$) and its dichloro Sn(IV) complex (SnTPP) at the CAM-B3LYP/SDD level of theory.

Band[a]	**#**[b]	**Calc**[c]		**Exp**[d]	**Wave Function**[e] =
		λ (nm)	F	λ (nm)	
					$\mathrm{H_2TPP}$
----	1	---	---	---	Ground State
Q	2	604	0.03	651	**64% s → -s; 35% a → -a**; …
	3	538	0.03	554	**60% s → -a; 39% a → -s**; …
B	4	371	1.19	419	**60% a → -a; 26% s → -s**; 10% HOMO−3 → -s; …
	5	360	1.67		**59% -a → s; 38% s → -a**; …
					SnTPP
----	1	---	---	---	Ground State
Q	2	573	0.03	602	**63% s → -s; 36% a → -a**; …
	3				**63% s → -a; 36% a → -s**; …
B	4	375	1.23	427	**57% a → -a; 33% s → -s**; …
	5				**57% a → -s; 33% s → -a**; …

[a] Band assignment described in the main text. [b] States assigned in terms of ascending energy in the TD-DFT calculation. [c] Calculated wavelengths (nm) with oscillator strengths in parentheses (f). [d] Observed wavelengths (nm) in DMSO [75, 80], [e] The wave functions calculated from the eigenvectors predicted by TD-DFT. One-electron transitions associated with the **a**, **s**, **-a**, and **-s** MOs of Michl's perimeter model [79] are highlighted in bold. Only one-electron transition contributions > 10% are shown.

Comparison of the predicted trends to the experimental data

In a similar manner to what is observed experimentally (**Table 1**), the band maxima of the Q and B bands of **1-4** are broadly similar (**Figure 37**). When different types of dye are compared across Series 1-4 (**Figures 39**, **42**, **45**, **48** and **51** **Tables 7-11**), significantly

larger differences in the B band maxima are predicted than are observed experimentally (**Figures 24-27**). In the context of the Sn(IV) complexes, this is due in part to configurational interaction that is predicted with other low-lying ππ* states (**Tables 7-11**).

When the porphyrin analogue is metalated, the B band is predicted to shift to the red (**Figures 39**, **42**, **45**, **48** and **51**, **Tables 7-11**). This trend can be rationalised through a consideration of the effects of metalation on the energy of the **s** MO (the HOMO in each case) relative to the **a**, **-a** and **-s** MOs (**Figures 40**, **43**, **46**, **49** and **52**), since it has large MO coefficients on the pyrrole nitrogens (**Figures 41**, **44**, **47**, **50** and **53**). The lower energy Q band is red shifted relative to that of Sn(IV) tetraphenylporphyrin (SnTPP) (**Tables 7-12**), making these complexes potentially more suitable for application in PDT, since this band is more likely to extend significantly into the phototherapeutic window (620−850 nm). The calculations for **3-Sn** and **4-Sn** (**Figures 48** and **51**, **Tables 10** and **11**) provide further evidence that the marked red shifts observed for the Q bands in DMSO (**Figures 26** and **27** and **Table 1**) are due to aggregation effects.

When the porphyrin analogues are quaternised, the Q and B bands are predicted to undergo a significant blue shift (**Tables 7-11**). This trend can be rationalised through a consideration of the effect of quaternisation on the energy of the **s** MO (the HOMO in each case) relative to the **a**, **-a** and **-s** MOs, since it has large MO coefficients on the *meso*-carbons. Significantly smaller shifts are observed in the band maxima in the experimental spectra, since the gas phase TD-DFT calculations do not adequately account for the effect that the solvation sphere has on the positive charge on the quaternized nitrogen atoms. The absence of an intense band immediately to the blue of the B band of the parent porphyrin ligand in the context of the calculated spectra of the quaternised dyes and complexes (**Figures 39**, **42**, **45**, **48** and **51**) provides evidence that bands observed experimentally in this context (**Figures 24-27**), especially in the context of Series 3 and 4, are almost certainly due to primarily to aggregation effects.

Conclusions

TD-DFT calculations can be used to identify key trends in the optical spectroscopy and electronic structures of porphyrin analogues in a manner that can guide the rational design of porphyrinoids for practical applications such as PDT and PACT. The minor changes observed in the HOMO−LUMO gaps for Series 1-4 (**Figures 39**, **41**, **44**, **49** and **52**) are consistent with the minor changes observed in the wavelengths of the main spectral bands in Chapter 3.

Chapter 8: Conclusion

The main purpose of this work was to synthesise and compare PDT and PACT activities of series of water-soluble *meso*-substituted Sn(IV) tetraarylporphyrins with AAAB, ABAB/AABB, ABBB and BBBB type substitution patterns (A = phenyl, B = 4-piperidinylphenyl). The dyes studied are referred to as Series 1−4 based on the number of 4-piperidinylphenyl groups introduced at the *meso*-positions. The free base porphyrin analogue within Series 1, 2, 3 and 4 were successfully synthesised and characterised by ^{1}H NMR and MALDI-TOF mass spectrometry. Although the free base porphyrin within Series 2 was synthesised, it cannot be fully characterised because the synthetic method gives a mixture of *cis* and *trans* 4-piperidinylphenyl disubstituted AABB and ABAB porphyrins. Since the molar masses are identical, these structures are likely to be eluted at almost the same rate during the separation of the Series 1−4 dyes by column chromatography.

Modification of the porphyrinoids was successfully achieved, as demonstrated by changes observed in the UV-visible absorption spectra, which correlate with the trends predicted in the calculated TD-DFT spectra and through characterisation by ^{1}H NMR and MALDI-TOF mass spectrometry measurements. The metal porphyrin Q-band maxima were red shifted compared to the free base dyes due to the effect of the tetravalent Sn(IV) central metal ion on the relative energies of the four frontier π-MOs from Gouterman's 4-orbital model. This enhances the utility of the dyes for use in PDT, since absorption in the phototherapeutic window (620−850 nm) is required.

The porphyrin analogues within Series 2 and 3 exhibited favourable photophysiochemical properties suitable for photosensitiser applications with regards to the singlet oxygen quantum yield (Φ_Δ), fluorescence quantum yield (Φ_F) and triplet state lifetime (τ_T) and Stokes shift values.

The PACT activity data demonstrate that the number of charges introduced by the quaternisation of 4-piperidinylphenyl nitrogen atoms does not correlate with the observed photodynamic activity. Series 4 provides scope for four positively charged nitrogen atoms, but this did not increase their antimicrobial activity. **1-Sn-Q** and **2-Sn-Q** with one and two positively charged nitrogen exhibited exceptional antimicrobial activity with Log_{10} reduction values of 5.11 and 7.49, respectively. This demonstrates that for a compound to be photodynamically active, there should be a balance between its hydrophilicity and lipophilicity properties.

Further structural modification of the free base dyes increased the photodynamic activity observed during *in vitro* cell studies. Due to the heavy atom effect, the insertion of the central Sn(IV) ion increased the singlet oxygen generation and photodynamic activity with low cancerous cell survival below 30%. The combination of metalation and quaternisation further enhanced the photodynamic activity of the compounds, with cancer cell survival 20% lower than the free base porphyrins. IC_{50} values > 1.79 and 1.09 μM were obtained, respectively, for **3-Sn** and **3-Sn-Q** after irradiation with a 595 nm LED (Thorlabs 595L3, dose: 9.0 mJ.cm^{-2} at the well-plate) for 60 min, making them potent compared to the other porphyrin analogues in the study.

Molecular docking of the compounds demonstrated that the porphyrin analogues within Series 1 will favourably interact and bind with HSA plasma protein due to the negative affinity values obtained. The predicted ADMET properties and pharmacological properties of all porphyrin analogues indicate that the porphyrin analogues can be safely administered through IV injection and do not have to be orally administered. The porphyrin analogues are not predicted to be carcinogenic in this context.

Future Recommendation

There is still more work to be done to evaluate the photodynamic activities of the different low-symmetry porphyrin structures. The following future work is recommended to address aspects of the study that could not be completed due to time constraints and logistical issues:

- Selectively synthesise the ABAB and AABB 4-(-1-piperidinyl) di-substituted Series 2 porphyrins and compare their photodynamic activity.
- The aggregation properties of the dyes could be studied in greater depth. This was not pursued since our primary interest was in the PDT and PACT activity studies.
- Use other MS techniques to try to obtain the missing MS data for **3-Sn**, **3-Sn-Q** and **4-Sn-Q**.
- Experimentally determine the binding affinity of the compounds to HSA and compare with the binding affinity obtained through molecular docking. Special permission is required to bring HSA into South Africa.
- Conduct PACT activity studies against other bacteria strains, such as Gram-(−) *E. coli.*
- Carry out Molecular docking studies against other biological molecules involved in the spread of cancer to demonstrate their inhibitory effect.
- In the longer term, the trends identified with the porphyrin series will guide the rational design of low-symmetry porphyrinoid analogues, such as chlorins and bacteriochlorins (**Figures 4** and **7**), that have more red-shifted Q bands that lie deep within the phototherapeutic window [49].

---References---

1. Global Task Force on Expanded Access to Cancer Care and Control in Developing Countries, “Cancer medicine prices in low– and middle–income countries”, Management Sciences for Health: Boston, USA, 2011. Available from: http://www.msh.org/sites/msh.org/files/ccd_msh.pdf. Accessed: [1 April 2024].
2. J. Ferlay, M. Ervik, F. Lam, M. Laversanne, M. Colombet, L. Mery, M. Piñeros, A. Znaor, I. Soerjomataram & F. Bray, Global Cancer Observatory: Cancer Today (version 1.1), International Agency for Research on Cancer: Lyon, France, 2024. Available from: https://gco.iarc.who.int/today. Accessed [1 April 2024].
3. National Cancer Institute. What is cancer? Available from: https://www.cancer.gov/about-cancer/understanding/what-is-cancer. Accesses [1 April 2024].
4. American Association for Cancer Research. What is cancer? Available from: https://www.aacr.org/patients-caregivers/about-cancer/what-is-cancer/. Accessed [1 April 2024].
5. A. Moten, D. Schafer & M. Ferrari, “Redefining global health priorities: Improving cancer care in developing settings”, *Journal of Global Health*, **2014**, *4*, 1010304.
6. G. Mathur, “Cancer: an overview”, *Academic Journal of Cancer Research,* **2015**, *8*, 1–9.
7. B.N. Ames., L.S. Gold & W. C. Willett, “The Causes and Prevention of Cancer”, *Proceedings of the National Academy of Sciences of the United States of America,* **1995**, *92*, 5258–5265.
8. A. Upadhyay, “Cancer: An unknown territory; rethinking before going ahead”, *Genes & Diseases*, **2020**, *8*, 655–661.
9. J.S. Brown, S.R. Amend, R.H. Austin, R.A. Gatenby, E.U. Hammarlund & K.J. Pienta, “Updating the Definition of Cancer”, *Molecular Cancer Research,* **2023**, *21*, 1142–1147.

10. M.G. Vander Heiden & R.J. DeBerardinis, “Understanding the intersections between metabolism and cancer biology”, *Cell*, **2017**, *168*, 657–669.

11. H. Arem & L. Erikka, “Cancer Epidemiology: A Survey of Modifiable Risk Factors for Prevention and Survivorship”, *American Journal of Lifestyle Medicine*, **2017**, *12*, 200–210.

12. S.H. Hassanpour & M. Dehghani, “Review of Cancer from Perspective of Molecular”, *Journal of Cancer Research and Practice*, **2017**, *4*, 127–129.

13. A. Imran, H.Y. Qamar, Q. Ali, H. Naeem, M. Riaz, S. Amin, N. Kanwal, F. Ali, M.F. Sabar & A.I. Nasir, “Role of Molecular Biology in Cancer Treatment: A Review Article”, *Iranian Journal of Public Health*, **2007**, *46*, 1475–1485.

14. L. Benov, “Photodynamic Therapy: Current Status and Future Directions”, *Medical Principles and Practice*, **2014**, *24*, 14–28.

15. R. Ackroyd, C. Kelty, N. Brown & M. Reed, “The history of photodetection and photodynamic therapy”, *Photochemical and Photobiological*, **2001**, *74*, 656.

16. J.H. Correia, J.A. Rodrigues, S. Pimenta, T. Dong & Z. Yang, Z, “Photodynamic Therapy Review: Principles, Photosensitizers, Applications, and Future Directions”, *Pharmaceutics*, **2021**, *13*, 1332.

17. P. Agostinis, K. Berg, K. Cengel, T. Foster, A. Girotti, S. Han, A. Juzeniene, D. Kessel, M. Korbelik, J. Moan, P. Mroz, D. Nowis, J. Piette, B. Willson & J. Golab, “Photodynamic Therapy of Cancer”, *A Cancer Journal for Clinicians*, **2011**, *61*, 250–281.

18. D.E.J.G.J. Dolmans, D. Fukumura & R.K. Jain, “Photodynamic Therapy for Cancer”, *Nature Reviews Cancer*, **2003**, *3*, 380–387.

19. B.C. Wilson & M.S. Patterson, “The physics, biophysics and technology of photodynamic therapy”, *Physics in Medicine and Biology*, **2008**, *53*, R61−R109.

20. H. Khanam, A.M. Dar & B.A. Shamsuzzaman, “Photodynamic Therapy in the Treatment of Cancer: A review”, *Journal of Integrative Medicine*, **2020**, *8*, 780.

21. T.J. Dougherty, C.J. Gomer, B.W. Henderson, G. Jori, D. Kessel, M. Korbelik, J. Moan & Q. Peng, “Photodynamic therapy”, *Journal of the National Cancer Institute*, **1998**, *90*, 889–905.

22. D.E. Dolmans, D. Fukumura & R.K. Jain, “Photodynamic therapy for cancer”, *Nature Reviews Cancer,* **2003**, *3*, 380–387.

23. L.B. Josefsen & R.W. Boyle, “Unique Diagnostic and Therapeutic Roles of Porphyrins and Phthalocyanines in Photodynamic Therapy, Imaging and Theranostics”, *Theranostics*, **2012**, *2*, 916–966.

24. M. Wainwright, “Photodynamic antimicrobial chemotherapy”, *Journal of Antimicrobial Chemotherapy*, **1998**, *42*, 13–28.

25. J. Ghorbani, D. Rahban, S. Aghamiri, T. Teymouri & A. Bahador, “Photosensitizers in antibacterial photodynamic therapy: an overview”, *Laser Therapy*, **2018**, *27*, 293–302.

26. R.C. Soy, B. Babu, D.O. Oluwole, N. Nwaji, J. Oyim, E. Amuhaya, E. Prinsloo, J. Mack & T. Nyokong, “Photophysicochemical properties and photodynamic therapy activity of chloroindium (III) tetraarylporphyrins and their gold nanoparticle conjugates”, *Journal of Porphyrins and Phthalocyanines*, **2019**, *1*, 34−45.

27. P. Agostini, K. Berg, K.A. Cengel, T.H. Foster, A.W. Girotti, S.O. Gollnick, S.M. Hahn, M.R. Hamblin, A. Juzeniene, D. Kessel, M. Korbelik, J. Moan, P. Mroz, D. Nowis, J. Piette & B.C. Wilson, “Photodynamic therapy of cancer: an update”, *A Cancer Journals for Clinicians*, **2011**, *61*, 250−281.

28. H. Grundmann, M. Aires-de-Sousa, J. Boyce & E. Tiemersma, “Emergence and resurgence of meticillin-resistant Staphylococcus aureus as a public-health threat”, *The Lancet*, **2006**, *368*, 874−885.

29. B.N. Green, C.D. Johnson, J.T. Egan, M. Rosenthal & E.A. Griffith, “Methicillin-resistant Staphylococcus aureus: an overview for manual therapists”, *Journal of Chiropractic Medicine*, **2012**, *11*, 64−76.

30. G. Ippolito, S. Leone, F.N. Lauria, E. Nicastri & R.P. Wenzel, “Methicillin-resistant *Staphylococcus aureus*: the superbug”, *International Journal of Infectious Diseases*, **2010**, 14, S7−S11.

31. L. Sobotta, P. Skupin-Mrugalska, J. Piskorz & J. Mielcarek, “Porphyrinoid photosensitizers mediated photodynamic inactivation against bacteria”, *European Journal of Medicinal Chemistry*, 2019, *175*, 72−106.

32. K. O’Riordan, O.E. Akilov & T. Hasan, “The potential for photodynamic therapy in the treatment of localized infections”, *Photodiagnosis and Photodynamic Therapy*, **2005**, *2*, 247−262.

33. M. Managa & T. Nyokong, “Photodynamic antimicrobial chemotherapy activity of gallium tetra-(4-carboxyphenyl) porphyrin when conjugated to differently shaped platinum nanoparticles,” *Journal of Molecular Structure*, **2015**, *1099*, 432−440.

34. B. Babu, A. Sindelo, J. Mack & T. Nyokong, “Thien-2-yl substituted chlorins as photosensitizers for photodynamic therapy and photodynamic antimicrobial chemotherapy,” *Dyes and Pigments*, **2021**, *185*, 108886.

35. Y.I. Openda, P. Sen, M. Managa & T. Nyokong, “Acetophenone substituted phthalocyanines and their graphene quantum dots conjugates as photosensitizers for photodynamic antimicrobial chemotherapy against *Staphylococcus aureus*”, *Photodiagnosis and Photodynamic Therapy*, **2020**, *29*, 101607.

36. X. Li, H. Bai, Y. Yang, J. Yoon, S. Wang & X. Zhang, “Supramolecular antibacterial materials for combatting antibiotic resistance”, *Advanced Materials,* **2019**, *31*, 1805092.

37. B. Babu, R. Soy, J. Mack & T. Nyokong, “Non-aggregated lipophilic water-soluble tin porphyrins as photosensitizers for photodynamic therapy and photodynamic antimicrobial chemotherapy”, *New Journal of Chemistry*, **2020**, *44,* 11006–11012.

38. R.M. Ion, “Revisiting Tetra-*p*-Sulphonated Porphyrin as Antimicrobial Photodynamic Therapy Agent”, *Coatings,* **2021**, *11*, 393.

39. M. Gouterman, G.H. Wagnière & L.C. Snyder, “Spectra of porphyrins: Part II. Four orbital model”, *Journal of Molecular Spectroscopy*, **1963**, *11*, 108–127.

40. E.D. Sternberg, D. Dolphin & C. Brückner, “Porphyrin-based photosensitizers for use in photodynamic therapy”, *Tetrahedron,* **1998**, *54*, 4151–4202.

41. A.P. Castano, T.N. Demidova & M.R. Hamblin, “Mechanisms in photodynamic therapy: part one - photosensitizers, photochemistry and cellular localization”, *Photodiagnosis and Photodynamic Therapy*, **2004**, *1*, 279–293.

42. M. Ethirajan, Y. Chen, P. Joshi & R.K. Pandey, “The role of porphyrin chemistry in tumour imaging and photodynamic therapy”, *Chemical Society Reviews*, **2010**, *40*, 340–362.

43. P. Rothemund & A.R. Menotti, “Porphyrin Studies. IV. The Synthesis of α,β,γ,δ-Tetraphenylporphine”, *Journal of the American Chemical Society*, **1941**, *63*, 267–270.

44. A. D. Adler, T. R. Longo, J. D. Finarelli, J. Goldmacher, J. Assour & L. Korsakoff, “A simplified synthesis for *meso*-tetraphenylporphine”, *Journal of Organic Chemistry*, **1967**, *32*, 476–476.

45. J. S. Lindsey, H. C. Hsu & I. C. Schreiman, “Synthesis of tetraphenylporphyrins under very mild conditions”, *Tetrahedron Letters*, **1986**, *27*, 4969–4970.

46. J. Mack, “Expanded, Contracted, and Isomeric Porphyrins: Theoretical Aspects”, *Chemical Reviews*, **2017**, *117*, 3444–3478.

47. J. Mack, M. J. Stillman & N. Kobayashi, “Application of MCD spectroscopy to porphyrinoids”, *Coordination Chemistry Reviews*, **2007**, *251*, 429–453.
48. R. C. Soy, B. Babu, J. Mack & T. Nyokong, “The photodynamic anticancer and antibacterial activity properties of a series of *meso*-tetraarylchlorin dyes and their Sn(IV) complexes”, *Molecules*, **2023**, *28*, 4030.
49. B. Babu, J. Mack & T. Nyokong, “Sn(iv)-porphyrinoids for photodynamic anticancer and antimicrobial chemotherapy”, *Dalton Transactions*, **2023**, *52*, 5000–5018.
50. W. Zhu, Y.H. Gao, P.Y. Liao, D.Y. Chen, N.N. Sun, P.A. Nguyen Thi, Y.J. Yan, X.F. Wu & Z.L. Chen, “Comparison between porphin, chlorin and bacteriochlorin derivatives for photodynamic therapy: Synthesis, photophysical properties, and biological activity”, *European Journal of Medicinal Chemistry*, **2018**, *160*, 146–156.
51. B. Babu, J. Mack & T. Nyokong, “Photodynamic activity of Sn(IV) tetrathien-2-ylchlorin against MCF-7 breast cancer cells”, *Dalton Transactions*, **2021**, *50*, 2177–2182.
52. Y. Lin, T. Zhou, R. Bai & Y. Xie, “Chemical approaches for the enhancement of porphyrin skeleton-based photodynamic therapy”, *Journal of Enzyme Inhibition and Medicinal Chemistry*, **2020**, *35*, 1080−1099.
53. C.C. Wamser & A. Ghosh, “The Hyperporphyrin Concept: A Contemporary Perspective”, *Journal of American Society*, **2020**, *2*, 1543–1560.
54. R. Cheng, P. Chen, T. Lovell, T. Liu, L. Noodleman & D.A. Case, “Symmetry and Bonding in Metalloporphyrins. A Modern Implementation for the Bonding Analyses of Five- and Six-Coordinate High-Spin Iron(III)−Porphyrin Complexes through Density Functional Calculation and NMR Spectroscopy”, *Journal of the American Chemical Society*, **2003**, *125*, 6774–678.
55. S. Scoditti, F. Chiodo, G. Mazzone, S. Richeter & E. Sicilia, “Porphyrins and Metalloporphyrins Combined with N-Heterocyclic Carbene (NHC) Gold(I) Complexes

for Photodynamic Therapy Application: What Is the Weight of the Heavy Atom Effect?", *Molecules*, **2022**, *27*, 4046.

56. J.M. Dabrowski, B. Pucelik, A. Regiel-Futyra, M. Brindell, O. Mazuryk, A. Kyzioł, G. Stochel, W. Macyk & L.G. Arnaut, "Engineering of Relevant Photodynamic Processes Through Structural Modifications of Metallotetrapyrrolic Photosensitizers", *Coordination Chemistry Reviews*, **2016**, *325*, 67–101.
57. B.C. Wilson & M.S. Patterson, "The physics, biophysics and technology of photodynamic therapy", *Physics in Medicine and Biology*, **2008**, *53*, 61–109.
58. K. Plaetzer, B. Krammer, J. Berlanda, F. Berr & T. Kiesslich, "Photophysics and photochemistry of photodynamic therapy: fundamental aspects", *Lasers in Medicine Science*, **2009**, *24*, 259–268.
59. F. Nifiatis, J.C. Athas, K.D. Gunaratne, Y. Gurung, K.M. Monette & P.J. Shivokevich, "Substituent Effects of Porphyrin on Singlet Oxygen Generation Quantum Yields", *The Open Spectroscopy Journal*, **2011**, *5*, 1–12.
60. W. Redmond & J.N. Gamlin, "A compilation of singlet oxygen yields from biologically relevant molecules", *Photochemistry and Photobiology*, **1999**, *70*, 391−475.
61. A. Magadla, D.O. Oluwole, J. Britton & T. Nyokong, "Effect of nature of nanoparticles on the photophysiochemical properties of asymmetrically substituted Zn phthalocyanines", *Inorganica Chimica Acta*, **2018**, *482*, 432–446.
62. B. Valeur & M.N. Berberan-Santos, "*Molecular Fluorescence: Principles and Applications*", Wiley-VCH: Weinheim, Germany, 2012.
63. R. L. Brookfield, H. Ellul, A. Harriman, G.J. Porter, "Luminescence of porphyrins and metalloporphyrins. Part 11.—Energy transfer in zinc–metal-free porphyrin dimers", *Journal of the Chemical Society, Faraday Transactions 2*, **1986**, *82*, 219−233.

64. C. Feng, S. Li, L. Fu, X. Xiao, Z. Xu, Q. Liao, Y. Wu, J. Yao & H. Fu, “Breaking Kasha’s Rule as a Mechanism for Solution-Phase Room-Temperature Phosphorescence from High-Lying Triplet Excited State”, *Journal of Physical and Chemistry Letters*, **2020**, *11*, 8246−8251.

65. G. Xiong, Z. Wu, J. Yi, L. Fu. Z. Yang, C. Hsieh, M. Yin, X. Zeng, C. Wu, A. Lu, X. Chen, T. Hou & D. Cao, “ADMETlab 2.0: An Integrated Online Platform for Accurate and Comprehensive Predictions of ADMET Properties”, *Nucleic Acids Res*, **2021**, *49*, W5–W14.

66. X. M. He & D. C. Carter, “Atomic structure and chemistry of human serum albumin”, *Nature*, **1992**, *358*, 209–215.

67. T. Strózik, M. Wolszczak, M. Hilczer, M. Pawlak, T. Wasiak, P. Wardęga, M. Ionov & M. Bryszewska, “Multi-Spectroscopic and Molecular Modeling Studies of Interactions Between Anionic Porphyrin and Human Serum Albumin”, *International Journal of Molecular Sciences*, **2024**, *25*, 12473.

68. A.M. Udrea, A. Dinache, A. Staicu & S. Avram, “Target Prediction of 5,10,15,20 *Tetrakis* (4-Sulfonatophenyl)-Porphyrin Using Molecular Docking”, *Pharmaceutics*, **2022**, *14*, 2390.

69. V.J. Bergh & H. Tønnesen, “Interaction between the Photosensitizer Lumichrome and Human Serum Albumin: Effect of Excipients”, *Pharmaceutical Development and Technology*, **2017**, *22*, 992–1000.

70. M. Samperi, S. Vittorio, L. De Luca, A. Romeo & L. Monsù Scolaro, “Interaction of Aggregated Cationic Porphyrins with Human Serum Albumin”, *International Journal of Molecular Sciences*, **2023**, *24*, 2099.

71. A. N. Hurst, B. Scarbrough, R. Saleh, J. Hovey, F. Ari, S. Goyal, R. Chi, J.M. Troutman & J.L. Vivero-Escoto, “Influence of Cationic meso-substituted Porphyrins on the Antimicrobial

Photodynamic Efficacy and Cell Membrane Interaction in *Escherichia coli*", *International Journal of Molecular Science*, **2019**, *20*, 134.

72. M.B. Spesia, D. Lazzeri, L. Pascual, M Rovera & E.N. Durantini, "Photoinactivation of *Escherichia coli* using porphyrin derivatives with different number of cationic charges", *Federation of European Microbiological Societies Immunology and Medical Microbiology*, **2005**, *44*, 289–295.
73. C. Hansch, P.P. Maloney, T. Fujita & Muir, "Correlation of biological activity of phenoxyacetic acids with Hammett substituent constants and partition coefficients", *Nature*, **1962**, *194*, 178–180.
74. Gaussian 09, Revision E.01, M.J. Frisch, G.W. Trucks, H.B. Schlegel, G.E. Scuseria, M.A. Robb, J.R. Cheeseman, G. Scalmani, V. Barone, G.A. Petersson, H. Nakatsuji, X. Li, M. Caricato, A. Marenich, J. Bloino, B.G. Janesko, R. Gomperts, B. Mennucci, H.P. Hratchian, J.V. Ortiz, A.F. Izmaylov, J.L. Sonnenberg, D. Williams-Young, F. Ding, F. Lipparini, F. Egidi, J. Goings, B. Peng, A. Petrone, T. Henderson, D. Ranasinghe, V.G. Zakrzewski, J. Gao, N. Rega, G. Zheng, W. Liang, M. Hada, M. Ehara, K. Toyota, R. Fukuda, J. Hasegawa, M. Ishida, T. Nakajima, Y. Honda, O. Kitao, H. Nakai, T. Vreven, K. Throssell, J.A. Montgomery, Jr., J.E. Peralta, F. Ogliaro, M. Bearpark, J.J. Heyd, E. Brothers, K.N. Kudin, V.N. Staroverov, T. Keith, R. Kobayashi, J. Normand, K. Raghavachari, A. Rendell, J.C. Burant, S.S. Iyengar, J. Tomasi, M. Cossi, J.M. Millam, M. Klene, C. Adamo, R. Cammi, J.W. Ochterski, R.L. Martin, K. Morokuma, O. Farkas, J.B. Foresman & D.J. Fox, Gaussian, Inc., Wallingford CT, 2013.
75. B. Babu, J. Mack & T. Nyokong, "Sn (IV) N-confused porphyrins as photosensitizer dyes for photodynamic therapy in the near IR region", *Dalton Transactions*, **2020**, *49*, 15180–15183.

76. B.P. McNicholl, J.W. McGrath & J.P. Quinn, “Development and application of a resazurin-based biomass activity test for activated sludge plant management”, *Water Research*, **2007**, *41*, 127–133.

77. C. A. Lipinski, F. Lombardo, B.W. Dominy, & P. J. Feeney, “Experimental and computational approaches to estimate solubility and permeability in drug discovery and development settings”, *Advanced Drug Delivery Reviews*, **2001**, *46*, 3–26.

78. J. Mack, M. Wildervanck & T. Nyokong, “TD-DFT Calculations and MCD spectroscopy of porphyrin and phthalocyanine analogues: rational design of photosensitizers for PDT and NIR region sensor applications”, *Turkish Journal of Chemistry*, **2014**, *38*, 1013–1026, 10.3906/kim-1406-32.

79. J. Michl, “Magnetic circular dichroism of aromatic molecules,” Tetrahedron, **1984**, *40*, 3845–3934.

80. J. Mack, Y. Asano, N. Kobayashi & M.J. Stillman, “Application of MCD spectroscopy and TD−DFT to a highly non-planar porphyrinoid ring system. New insights on red−shifted porphyrinoid spectral bands,” *Journal of the American Chemical Society,* **2005**, *127*, 17697–17711.